

**THIN FILM PROCESSING AND THE MORPHOLOGICAL AND
MECHANICAL CHARACTERIZATION OF SULFONATED
POLY(STYRENE-ISOBUTYLENE-STYRENE) (SIBS)
TRIBLOCK COPOLYMERS**

By

Omar A. Movil Cabrera

A dissertation submitted in partial fulfillment of the requirements for the degree of

DOCTOR OF PHILOSOPHY
in
CHEMICAL ENGINEERING

UNIVERSITY OF PUERTO RICO, MAYAGÜEZ CAMPUS

2013

Approved by:

Agnes M. Padovani Blanco, PhD
Graduate Committee Chairperson

Date

Aldo Acevedo Rullan, PhD
Member, Graduate Committee

Date

Oscar M. Suarez, PhD
Member, Graduate Committee

Date

David Suleiman Rosado, PhD
Member, Graduate Committee

Date

Luis Morell Cruz, PhD
Representative of Graduate Studies

Date

Aldo Acevedo Rullan, PhD
Director, Chemical Engineering Department

Date

*“I do not think there is any thrill than can go
through the human heart like that felt by the
scientist as he sees some creation of the brain
unfolding to success...Such emotions make a man forget
food, sleep, pain, friends, love, everything”*

Nikola Tesla

ACKNOWLEDGEMENTS

First of all, I would like to thank Dr. Agnes Padovani, without whose support, patience and commitment, the difficulties during my doctoral studies might have been greater. Also, I extend my thanks to my committee members Dr. David Suleiman, Dr. Aldo Acevedo, and Dr. Marcelo Suárez for their constructive collaboration in this work. I also want to thank CREST-UPRM program for its financial support. Thanks Marcelo for giving me the opportunity to belong to this prestigious program. You are my role model, thank you for showing me the way.

I would like to thank Boris Rentería and Carlos Rivera who were always willing to help and give their best technical suggestions. Many thanks to Sonia Avilés, Gabriel Negrón, Ulises Barajas, Jose Primera, Omar Vega, Roberto Olayo, and Wilman Cabrera. My research would not have been possible without their help.

Thanks to my good friends David Ramirez, Amelida Echavarría, Brendaly Rodríguez, Marcos Garza, and Victor Rios and his family, for teaching me to love “The Island of Enchantment”.

Last, but in no way least, I would like to express sincere thanks to the members of my family (Dad, Mom, Titi, and Juan) for their unconditional love and support.

Table of Contents

ACKNOWLEDGEMENTS	iii
List of Tables	vii
List of Figures	ix
ABSTRACT	xvi
RESUMEN.....	xviii
CHAPTER 1	1
INTRODUCTION	1
1.1. Project Objectives.....	4
CHAPTER 2.....	6
BACKGROUND.....	6
2.1. Polymer Electrolyte Membranes (PEMs).....	6
2.2. Electrochemical Devices	13
2.2.1 Portable Polymer Electrolyte Membrane Fuel Cells (PEMFCs)	13
2.2.2. Micro (μ) Sensors.....	16
2.2.3. Micro (μ) Actuators.....	18
2.3 Polymer Electrolyte Thin Films	20
CHAPTER 3.....	24
PROJECT METHODOLOGY	24
3.1. Sample Preparation.....	24
3.1.1. Materials	24
3.1.2. Thin Film Fabrication Process	25
3.1.3. Hydration Process.....	26
3.1.4. Membrane Electrode Assembly Fabrication Process	28
3.2. Materials Characterization Techniques	30
3.2.1. Optical Microscopy	30
3.2.2. Profilometry	30
3.2.3 Atomic Force Microscopy (AFM)	30
3.2.4. Fourier Transform Infrared Spectroscopy (FTIR).....	31

3.2.5. Differential Scanning Calorimetry (DSC) and Thermogravimetric Analysis (TGA).....	31
3.2.6. X-ray Diffraction (XRD)	31
3.2.7. Nanoindentation	32
3.2.8. Adhesion Testing.....	40
3.2.8.1. Adhesion Background.....	40
3.2.8.2. Scratch Adhesion Testing with Nanoindentation.....	44
3.2.9. Scanning Electron Microscopy (SEM).....	46
CHAPTER 4.....	47
PHYSICAL CHARACTERIZATION OF SIBS THIN FILMS	47
4.1. Thin Film Quality	47
4.2. Thin Film Thickness.....	59
4.3. Summary.....	60
CHAPTER 5.....	62
CHEMICAL AND MORPHOLOGICAL CHARACTERIZATION OF SIBS THIN FILMS.....	62
5.1. Chemical Characterization.....	62
5.2. Morphological Characterization.....	66
5.2.1. Solvent Effects	67
5.2.2. Sulfonation Percent and Thermal Annealing Treatment Effects	69
5.2.3. Polymer Concentration Effects	76
5.3 Summary.....	78
CHAPTER 6.....	79
MECHANICAL CHARACTERIZATION OF SIBS THIN FILMS.....	79
6.1. Substrate-Independent Mechanical Properties.....	79
6.2. Mechanical Characterization.....	94
6.2.1. Sulfonation Percent Effects.....	94
6.2.2. Polymer Concentration Effects	99
6.2.3. Temperature Effects	101
6.2.4. Hydration Treatment Effects.....	105

6.3. Summary	108
CHAPTER 7	110
ADHESION CHARACTERIZATION OF SIBS THIN FILMS	110
7.1. Practical Adhesion Measurement	110
7.3. Summary	122
CHAPTER 8	123
CONCLUSIONS	123
RECOMMENDATIONS	125
REFERENCES	126

List of Tables

Table 2.1. Classification of PEMs and their structure-property relationships.....	9
Table 2.2. Examples of sulfonated block copolymers that have been studied as PEM.....	11
Table 2.3. Summary of studies focused on polymer electrolyte thin films fabricated by spin coating.....	21
Table 3.1. Processing conditions used for the fabrication of SIBS and Nafion [®] thin films.....	26
Table 3.2. Process conditions used for the MEA fabrication.....	29
Table 3.3. Parameters used for the nanoindentation tests.....	39
Table 3.4. Parameters used for the hot stage nanoindentation tests.....	40
Table 3.5. Adhesion test methods based upon the application of stress.....	43
Table 3.6. Parameters used for the scratch adhesion tests.....	46
Table 4.1. Surface roughness measurements for the continuous films.....	56
Table 4.2. Thickness measurements for the thin films fabricated using different process conditions.....	59
Table 5.1. Main IR peaks of unsulfonated SIBS and their corresponding vibrational mode descriptions.....	63

Table 5.2. PS domain size as a function of the sulfonation percent in the SIBS thin films.....	74
Table 6.1. Average results for the measured substrate-independent elastic modulus and hardness of the SIBS thin films.....	88
Table 7.1. Critical loads for the studied samples.....	112

List of Figures

Figure 2.1. Chemical structure of Nafion [®]	7
Figure 2.2. Chemical structure of SIBS membranes.....	12
Figure 2.3. Schematic of a Polymer Electrolyte Membrane Fuel Cell (PEMFC) as depicted by Chu <i>et al.</i>	14
Figure 2.4. Schematic of two chamber design MEMS-based μ -PEMCF proposed by Jankowski and co-workers.....	15
Figure 2.5. Schematic representation of CNFET fabricated by Star <i>et al.</i>	17
Figure 2.6. Process flow used by Zhou <i>et al.</i> for the fabrication of a Nafion [®] Microactuator.....	19
Figure 3.1. Image of nanoindentation samples ready to be hydrated.....	27
Figure 3.2. Experimental setup used to hydrate the thin film samples.....	28
Figure 3.3. Process flow for the MEA fabrication.....	29
Figure 3.4. Schematic representation of the proposed Hay-Crawford Model.....	35
Figure 3.5. (a) Images for the G200 NanoIndenter and (b) the sample tray used for the nanoindentation experiments. Figure 3.5c corresponds to a SEM image of a Berkovich tip, courtesy of Hysitron Inc.....	38
Figure 3.6. Images for (a) the sample mounted on the metallic disk and (b) the sample onto the hot stage ready for testing.....	39

Figure 3.7. Schematic representation of a three-step ramp-load-scratch sequence used for the adhesion testing.....45

Figure 4.1. AFM topography images for SIBS00 thin films fabricated at 2.5 wt% polymer concentration using: (a) a mixture of toluene and hexyl alcohol, and (b) pure toluene. Figures 4.1c and 4.1d: characteristic line profiles for the films in 4.1a and 4.1b, respectively.....48

Figure 4.2. AFM topography images of SIBS thin films fabricated at 2.5 wt% polymer concentration from block copolymers with sulfonation percents of: (a) 20, (b) 45, and (c) 80%. Figures 4.2d – 4.2f: line profiles for the films in 4.2a to 4.2c, respectively.....50

Figure 4.3. (a) AFM topography image for SIBS20 film fabricated at 2.5 wt% polymer concentration and using a mixture of toluene and hexyl alcohol. (b) corresponding line profile.....52

Figure 4.4. AFM topography images for SIBS thin films fabricated at 5 wt% polymer concentration from block copolymers with sulfonation percents of: (a) 0, (b) 20, (c) 45%, and (d) 80%.....54

Figure 4.5. AFM topography images for SIBS thin films fabricated at 10 wt% polymer concentration from block copolymers with sulfonation percents of: (a) 0, (b) 20, and (c) 45%.....55

Figure 4.6. Optical microscopy images for SIBS thin films fabricated from polymers with sulfonation percents of 0, 45, and 80%. Figures 4.6a to 4.6c at 2.5 wt% polymer

concentration. Figures 4.6d to 4.6f at 5 wt% polymer concentration, respectively.....57

Figure 5.1. FTIR spectrum for an unsulfonated SIBS thin films fabricated at 10 wt% polymer concentration.....63

Figure 5.2. FTIR spectra for SIBS thin films fabricated at 2.5 wt% polymer concentration with sulfonation percents of: (a) 0%, (b) 45%, (c) 70%, and (d) 80%.....64

Figure 5.3. FTIR spectra for SIBS thin films fabricated at 5 wt% polymer concentration with sulfonation percent of: (a) 0%, (b) 20%, (c) 45%, (d) 70%, and (e) 80%.....65

Figure 5.4. FTIR spectra for SIBS thin films fabricated at 10 wt% polymer concentration with sulfonation percent of: (a) 0%, (b) 20%, and (c) 45%.....66

Figure 5.5. AFM phase images for thin films fabricated with SIBS00 polymer and using two different solvent systems: (a) 85:15 (v/v) toluene/hexyl alcohol mixture and (b) pure toluene.....68

Figure 5.6. AFM phase images for SIBS thin films at different sulfonation percents. Figures 5.5a to 5.5d: Samples without thermal annealing fabricated from SIBS polymers with sulfonation percents of: (a) 0, (b) 20, (c) 45, and (d) 80%. Figures 5.5e to 5.5h: Corresponding AFM phase images for the thermally annealed (130 °C) samples. Figures 5.5i and 5.5j: Corresponding FFT images for the annealed (130 °C) samples shown in Figures 5.5e and 5.5f. Figures 5.5k and 5.5l: Samples fabricated from SIBS polymers with

sulfonation percents of: (k) 45 and 150 °C thermal annealing, and (l) 80% and 170 °C thermal annealing.....69

Figure 5.7. DSC curves for SIBS polymers with sulfonation percents of: (a) 0%, (b) 20%, (c) 45%, and (d) 80%. Data presented is for the second re-heating step in the cycle.....72

Figure 5.8. X-ray diffraction patterns for: (a) blank silicon wafer substrate and (b) SIBS thin films with different sulfonation percents.....75

Figure 5.9. AFM phase images for films fabricated from SIBS00 and SIBS20 at: 2.5 wt% polymer concentration (Fig. 5.8a and 5.8c, respectively) and at 10 wt% polymer concentration (Fig. 5.8b and 5.8d, respectively).....77

Figure 6.1. Load versus displacement data obtained for an indentation array in SIBS45-C.....80

Figure 6.2. Optical microscopy image for a 5x4 indentation array on sample SIBS45-C.....81

Figure 6.3. Apparent and substrate-independent elastic modulus as a function of normalized displacement for different SIBS films. Figures 6.3a – 6.3c: Corresponding results for films with sulfonation percent of 0% and fabricated at 2.5 wt%, 5 wt%, and 10 wt% polymer concentration, respectively. Figures 6.3d – 6.3f: Corresponding results for films with sulfonation percent of 45% and fabricated at 2.5 wt%, 5 wt%, and 10 wt% polymer concentration, respectively.....83

Figure 6.4. Apparent and substrate-independent elastic modulus as a function of normalized displacement for different SIBS films. Figures 6.4a and 6.4b: Corresponding results for films with sulfonation percent of 20% and fabricated at 5 wt% and 10 wt% polymer concentration, respectively. Figures 6.4c and 6.4d: Corresponding results for films with sulfonation percent of 70% and fabricated at 2.5 wt% and 5 wt% polymer concentration, respectively.....84

Figure 6.5. Elastic moduli maps for SIBS thin films fabricated at 5 wt% and with different sulfonation percents: (a) 0%, (b) 20%, and (c) 45%.....86

Figure 6.6. Elastic moduli maps for SIBS thin films fabricated at 5 wt% and with different sulfonation percents: (a) 70%, and (b) 80%.....87

Figure 6.7. Hardness as a function of normalized displacement for different SIBS films. Figures 6.7a – 6.7c: Corresponding results for films with sulfonation percent of 0% and fabricated at 2.5 wt%, 5 wt% and 10 wt% polymer concentration, respectively. Figures 6.7d – 6.7f: Corresponding results for films with sulfonation percent of 45% and fabricated at 2.5 wt%, 5 wt% and 10 wt% polymer concentration, respectively.....91

Figure 6.8. Hardness as a function of normalized displacement for different SIBS films. Figures 6.8a and 6.8b: Corresponding results for films with sulfonation percent of 20% and fabricated at 5 wt% and 10 wt% polymer concentration, respectively. Figures 6.8c and 6.8d: Corresponding results for films with sulfonation percent of 70% and fabricated at 2.5 wt% and 5 wt% polymer concentration, respectively.....93

Figure 6.9. (a) Substrate-independent elastic modulus and (b) hardness for SIBS thin films as a function of sulfonation percent and polymer concentration.....96

Figure 6.10. DSC curves for SIBS polymers with sulfonation percents of:(a) 0%, (b) 20%, (c) 45%, and (d) 80%. Data presented is for the first-heating step in the cycle.....97

Figure 6.11. TGA curves for SIBS polymers with sulfonation percents of: (a) 0%, (b) 20%, (c) 45%, and (d) 80%.....99

Figure 6.12. (a) Elastic modulus and (b) hardness as a function of temperature for a variety of SIBS and Nafion[®] films.....102

Figure 6.13. Hydration treatment effects on the mechanical properties of SIBS thin films: (a) elastic modulus and (b) hardness for different SIBS.....107

Figure 7.1. Displacement into the surface versus scratch distance data for the scratches performed on SIBS samples with sulfonation percents of (a) 0%, (b) 20%, (c) 45% and (d) 80%. Figure 7.1e correspond to the scratch result on the Nafion[®] film.....111

Figure 7.2. Coefficient of Friction data versus scratch distance for the scratches performed on SIBS samples with sulfonation percents of (a) 0%, (b) 20%, (c) 45% and (d) 80%. Figure 7.1e correspond to the scratch result on the Nafion[®] film.....114

Figure 7.3. SEM images for scratches performed on the SIBS00-C film.....116

Figure 7.4. SEM images for scratches performed on the SIBS20-C film.....	117
Figure 7.5. SEM images for scratches performed on the SIBS45-C film.....	118
Figure 7.6. SEM images for scratches performed on the SIBS80-B film.....	119
Figure 7.7. SEM images for scratches performed on the Nafion® film.....	120
Figure 7.8. Average normalized critical load for the studied samples.....	121

ABSTRACT

This work focuses on the fabrication and characterization of SIBS thin films deposited via spin-coating for potential applications in microelectrochemical devices. The main goals of this project are to determine suitable parameters to fabricate uniform and continuous SIBS thin films and to perform the materials characterization with particular emphasis on the morphology as well as on the mechanical and adhesive properties of the films. The materials properties are evaluated as a function of critical parameters such as the sulfonation percent and polymer concentration in the films. The effect of hydration and temperature on the mechanical properties of the films is also considered. Nafion[®] thin films are assessed for comparative purposes.

A variety of techniques are used for the materials characterization including profilometry, optical microscopy, atomic force microscopy (AFM), Fourier transform infrared spectroscopy (FTIR), X-ray diffraction, differential scanning calorimetry (DSC), nanoindentation, scratch adhesion testing, and scanning electron microscopy (SEM).

The results show that the film continuity and uniformity, as well as the film thickness, increases as a function of both, sulfonation percent and polymer concentration. AFM studies reveal phase-separated morphologies with critical transitions from a short-range ordered cylindrical/lamellar morphology to a more disordered morphology (network-like structure) as the sulfonation percent increases in the films.

Nanoindentation results show that both, the elastic modulus and hardness, increase with the sulfonation percent, except for the 5 wt% polymer films, where the elastic modulus decreases most likely as a result of higher solvent and/or moisture retention in the films. Conversely, the

mechanical properties significantly decrease with polymer concentration regardless of the sulfonation percent of the films.

A potential correlation is established between the morphology and the mechanical properties of the SIBS thin films. In general, films with a network-like structure exhibit improved mechanical properties as compared to films that exhibit non-interconnected domains. Also, SIBS thin films are more thermo-mechanically stable as compared to Nafion[®] films, even at low sulfonation percent.

Scratch adhesion testing reveals that the practical adhesion for the SIBS thin films is higher as compared to the Nafion[®] films.

RESUMEN

Este trabajo se enfoca en la fabricación y caracterización de películas delgadas de SIBS depositadas por medio de la técnica de “spin-coating” para aplicaciones en dispositivos micro-electroquímicos. Los principales objetivos de este proyecto son determinar los parámetros adecuados para la fabricación de películas delgadas de SIBS que sean continuas y uniformes y también, llevar a cabo la caracterización del material con particular énfasis en la morfología y las propiedades mecánicas y adhesivas. Las propiedades del material se evalúan en función de parámetros críticos como el porcentaje de sulfonación y la concentración de polímero en las películas delgadas. Además, se estudian los efectos de hidratación y temperatura sobre las propiedades mecánicas de las películas. Películas delgadas de Nafion® también se caracterizan con el objetivo de hacer estudios comparativos.

Varias técnicas se utilizan para la caracterización del material incluyendo perfilometría, microscopía óptica, microscopía de fuerza atómica, espectroscopía infrarroja de transformada de Fourier, difracción de rayos X, calorimetría diferencial de rastreo, nanoindentación, pruebas de adhesión y microscopía de rastreo electrónico.

Los resultados indican que tanto la continuidad, la uniformidad y el espesor de las películas de SIBS aumentan en función del porcentaje de sulfonación y de la concentración de polímero. Los resultados de microscopía de fuerza atómica revelan que cuando el porcentaje de sulfonación aumenta en las películas, éstas exhiben una transición morfológica de cilíndrica-lamelar a una morfología más desordenada, parecida a una red de dominios de poliestireno interconectados entre sí.

Los resultados de nanoindentación demuestran que tanto el módulo de elasticidad como la dureza aumentan en función del porcentaje de sulfonación, excepto para las películas fabricadas a una concentración de polímero de 5% (p/p), en donde el módulo de elasticidad disminuye posiblemente debido a una mayor retención de disolvente y humedad en las películas. Por el contrario, las propiedades mecánicas disminuyen significativamente con el aumento en la concentración de polímero, independientemente del porcentaje de sulfonación de las películas.

También se establece una posible correlación entre la morfología y las propiedades mecánicas de las películas de SIBS. En general, las películas con morfología de dominios interconectados muestran mejores propiedades mecánicas en comparación con las de morfología conformada por dominios aislados. Además, las películas de SIBS son termomecánicamente más estables que las películas de Nafion[®], aún a bajos porcentajes de sulfonación.

Los resultados de las pruebas de adhesión revelan que la adhesión de las películas de SIBS es mayor en comparación con las películas de Nafion[®].

CHAPTER 1

INTRODUCTION

Polymer electrolyte membranes (PEMs) have attracted considerable attention over the last few years due to their potential use in microelectrochemical devices such as fuel cells, sensors, biosensors, and actuators.^{1,2} PEM materials are usually made from ionomers and designed to conduct protons. A variety of materials have been tested for PEM applications with Nafion[®] being the material-of-choice. Nafion[®] has good proton conductivity and long-term stability,^{3,4} but unfortunately, it is very expensive and has high methanol crossover, which negatively affects the performance of fuel cells.⁵ Another disadvantage of Nafion[®] is its poor adhesion to different substrates and electrodes.⁶ The latter is a result of low surface energy induced by the presence of fluorinated groups in its backbone, which causes poor adhesion to electrode materials and hence, a decrease in the conduction of protons at the electrode-membrane interface.⁷

Some of the alternative membranes that have been developed in an attempt to replace Nafion[®] include, but are not limited to: perfluorinated ionomers, partially fluorinated polymers, non-fluorinated membranes with aromatic backbones, non-fluorinated hydrocarbons, and acid–base blends.^{8,9} However, matching all the favorable qualities of Nafion[®] has proven a real challenge.

More recently, sulfonated block copolymers have become attractive as PEMs due to their unique morphology, excellent selectivity, and good mechanical and chemical stability.^{5,10,11} Among the wide variety of sulfonated block copolymers that have been

synthesized, poly(styrene-isobutylene-styrene) (SIBS) is a strong candidate because it has lower methanol crossover as compared to Nafion[®], lower cost, it does not have fluorinated groups in its backbone, and at high sulfonation percent, the material exhibits proton conductivities comparable to those of Nafion[®].¹²

Due to the market demand for more cost-effective, smaller, and longer lasting electrochemical devices, today it is not only necessary to develop novel PEM materials that are lower in cost and have comparable materials properties to those of Nafion[®], but also materials that are compatible with silicon technology.^{13,14} The latter is critical in order to be able to integrate PEM materials into micro- and nanometer-sized electrochemical devices. Therefore, growing demands for portable device technology applications have placed the following critical requirements on PEM materials: (i) the need to be developed into thin film technology with materials properties comparable to those observed in the bulk and (ii) their successful integration with silicon micromachining techniques in order to be able to fabricate the devices.^{15,16,17,18,19,20,21}

Undoubtedly, the effective integration of polymer electrolyte thin films into micro-devices will largely depend on their mechanical properties.^{22,23,24} In fact, hardness measurements are often used as a measure of wear resistance, whereas the elastic modulus is used to predict the intrinsic stress in a thin film.^{25,26} These are very important properties because the mechanical failures typically observed in micro-devices usually arise from stress generated during either, the manufacture or operation of the device, as a result of differences in the thermal expansion coefficient or the elastic properties of the various components.²⁷

In addition, due to the fact that micro-devices generate heat under operation, there is a need to use thermo-mechanically stable thin films in order to avoid thermal fatigue damages or failures.^{28,29} Hence, knowledge of the mechanical properties of the polymer electrolyte thin films as a function of temperature is also required for proper design and reliability assessment of any PEM-based micro-devices.³⁰

Some micro-devices, especially sensors and biosensors, are also designed to operate in aqueous media and/or environments with high relative humidity. Water absorption could potentially change the microstructure of a polymer and thus result in variations in its mechanical properties.^{31,32} Therefore, proper assessment of the integration capability of PEM materials must include, water absorption studies as well as careful evaluation of the mechanical and adhesive properties of the films under various conditions.^{33,34,35,36}

Based on the above arguments, the purpose of this investigation was to evaluate the newly-developed SIBS polymers for potential applications in micro- and/or nanometer-sized electrochemical devices. The main goals were to develop SIBS into thin film technology, for the first time, and to perform the corresponding materials characterization studies with particular emphasis on the effect of process variables. As such, the effect of sulfonation percent and polymer concentration on film morphology as well as on the mechanical and adhesive properties of the films were evaluated. Understanding the influence of the fabrication parameters on the materials properties of SIBS thin films is important because this knowledge could ultimately be used to improve the materials properties of the films and therefore, enhance their potential application into microelectrochemical devices.

1.1. Project Objectives

The proposed research project encompasses two major objectives that are summarized below.

The first objective of this research project is the fabrication and characterization of SIBS into thin film technology and the corresponding materials characterization studies including a comparison with Nafion[®] films. In order to fulfill this goal, some of the more specific objectives are: (1) to determine suitable spin-coating parameters to fabricate continuous and defect-free SIBS and Nafion[®] thin films and (2) to characterize the materials properties of SIBS thin films and evaluate the effect of some critical parameters such as sulfonation percent and polymer concentration.

A wide variety of techniques were used to evaluate the materials properties of the spin-coated films. More specifically, thin film quality, that is, the formation of continuous and uniform films, was evaluated using both optical and atomic force microscopy (AFM). The film thickness was measured using profilometry and the chemical and morphological characterization of the films was performed using Fourier Transform Infrared Spectroscopy (FTIR) and AFM, respectively. Similarly, X-ray diffraction was used to assess the microstructure of the polymer films. In addition, the mechanical properties of the thin films were determined using instrumented nanoindentation. Finally, differential scanning calorimetry (DSC) and thermogravimetric analysis (TGA) were used to evaluate the glass transition temperature (T_g) and other thermal transitions of the SIBS polymers.

The second objective of this project is to study the compatibility of SIBS thin films with silicon technology and other device requirements. The specific objectives in this case are: (1) to determine suitable process conditions to fabricate the membrane electrode assemblies (MEAs) and (2) to evaluate the mechanical and adhesive properties of the SIBS thin films.

CHAPTER 2

BACKGROUND

The following chapter introduces the theoretical background of PEM materials as well as their potential application into microelectrochemical devices such as microfuel cells, microsensors, and microactuators. At the end of the chapter, a brief review of polymer electrolyte thin films is also presented.

2.1. Polymer Electrolyte Membranes (PEMs)

Polymer electrolyte membranes or proton exchange membranes are semipermeable polymers generally made from ion-charged polymers or ionomers. PEM materials are the core component of PEM-based electrochemical devices and in general, they provide three major functions: the transport of protons, a physical separation between the electrodes (or reactants), and the insulation that hinders electronic conduction through the membrane.³⁷

The original PEMs were developed by General Electric in 1959 through the polymerization of phenol-sulfonic acid with formaldehyde. Unfortunately, the resulting membranes showed poor mechanical stability, short lifetime, and low power density.^{38,39}

Later, DuPont[®] developed a perfluorosulfonic acid called Nafion[®] by incorporating perfluorovinyl ether groups terminated with sulfonic groups into a tetrafluoroethylene (Teflon) matrix. The chemical structure of Nafion[®] is shown in **Figure 2.1**. This material showed good proton conductivity and long-term stability, which made it the material-of-choice for Polymer Electrolyte Membrane Fuel Cells (PEMFCs).^{40,41,42,43,44,45}

deposition of a thick titanium layer on its surface or by increasing its surface roughness using plasma etching.⁴⁷

Nevertheless, due to the various disadvantages of Nafion[®], numerous membranes have been developed in an effort to replace it. However, matching all the favorable qualities of Nafion[®] has proven a real challenge. Some of these alternatives include, but are not limited to: perfluorinated ionomers, partially fluorinated polymers, non-fluorinated membranes with aromatic backbones, non-fluorinated hydrocarbons, and acid–base blends.^{48,49,50,51} Sumitha *et al.*³⁹ summarized the structure–property relationship for some of these membranes as shown in **Table 2.1**.

More recently, sulfonated block copolymers have become attractive as PEMs due to their unique morphology, excellent selectivity, and good mechanical and chemical stability.^{5,10,11} Sulfonation of block copolymers causes the formation of two microdomains within the polymer matrix. One of these microdomains contains ionic clusters that form conductive channels that facilitate the transport of charge, whereas the other, a nonionic microdomain, provides mechanical stability to the membrane.¹¹

As an example, Bae *et al.*⁵² synthesized a series of sulfonated poly(arylene ether sulfone) (SPE) block copolymers containing fluorinated groups. In this study, bis(4-fluorophenyl) sulfone (FPS) and 2,2-bis(4-hydroxy-3,5-dimethylphenyl) propane were used as comonomers for the hydrophobic blocks, whereas FPS and 9,9-bis(4-hydroxyphenyl) fluorene were used as the hydrophilic blocks. The results showed that SPE block copolymers with ion exchange capacity (IEC) of 2.20 mEq/g exhibited proton conductivities (at 80 °C) of 0.14 S/cm at 80% relative humidity and 0.02 S/cm at 40%

relative humidity. Although these results are comparable with Nafion[®], these membranes are also likely to have poor adhesion to the electrode materials due to their highly fluorinated group content.

Table 2.1. Classification of PEMs and their structure-property relationships.

Category	Structure	Physical properties
Perfluorinated membranes (pf)	<ul style="list-style-type: none"> ▪ Fluorinated backbone like PTFE ▪ Fluorocarbon side chain ▪ Ionic cluster consisting of sulfonic acid ions attached to the side chains 	<ul style="list-style-type: none"> ▪ Membranes are strong and stable in both oxidative and reductive environments
Partially fluorinated membranes	<ul style="list-style-type: none"> ▪ Fluorocarbon base ▪ Hydrocarbon aromatic side chain grafted onto the backbone, which can be modified 	<ul style="list-style-type: none"> ▪ Membranes are relatively strong in comparison to pf, but degrade fast
Non-fluorinated hydrocarbon membranes	<ul style="list-style-type: none"> ▪ Hydrocarbon base, typically modified with polar groups 	<ul style="list-style-type: none"> ▪ Membranes possess good mechanical strength ▪ Poor chemical and thermal stability
Non-fluorinated aromatic membranes	<ul style="list-style-type: none"> ▪ Aromatic base, typically modified with polar/sulfonic acid groups 	<ul style="list-style-type: none"> ▪ Good mechanical strength ▪ Chemically and thermally stable even at elevated temperatures
Acid-base blend membranes	<ul style="list-style-type: none"> ▪ Incorporation of acid component into an alkaline polymer base 	<ul style="list-style-type: none"> ▪ Stable in oxidizing, reducing, and acidic environments ▪ High thermal stability

Another research group, Aviles *et al.*⁵³ reported the synthesis of sulfonated poly (styrene-isoprene-styrene) membranes. This study showed that membranes with high sulfonation levels experienced a greater change in volume (swelling) after water absorption. As an alternative, different cations were incorporated into the membrane to enhance

crosslinking, and thus, produce more rigid membranes. The results, however, demonstrated that contrary to expected some cations such as Mg^{+2} , increased the swelling of the membrane.

In 2011, Elabd & Hickner¹¹ presented a review about the advances in PEM technology. Their list of additional sulfonated block copolymers that had been studied as PEMs is shown in **Table 2.2**. Among the list, sulfonated poly (styrene-isobutylene-styrene) (SIBS) appears as a strong candidate to replace Nafion[®] because it has lower methanol crossover as compared to Nafion[®], lower cost, it does not have fluorinated groups in its backbone, and at high sulfonation levels, these materials have exhibited proton conductivities comparable to Nafion[®].¹² SIBS membranes have sulfonic groups chemically-attached to the styrene blocks, which form polar domains covalently bonded to the isobutylene blocks. The chemical structure of SIBS is shown in **Figure 2.2**. These membranes also exhibit phase segregation at the nanometer scale due to the incompatible nature of its polymer blocks.⁵⁴ Studies have demonstrated that the morphology of SIBS and its properties vary with polymer block composition and sulfonation level. In fact, Elabd *et al.*⁵⁵ observed that when the sulfonation level of the SIBS membrane was increased from 13 to 82%, it experienced a morphological transition from a periodic (ordered) phase to an entirely non-periodic (disordered) phase. They also observed that both, morphological and transport properties, depended on the type of solvent used. For example, proton conductivities in the range of 0.0059 S/cm^{-1} were observed for SIBS samples fabricated from pure toluene, whereas samples fabricated from a toluene/ethanol mixture showed values on the order of $0.0000107 \text{ S/cm}^{-1}$.

The structure-property relationship of SIBS membranes fabricated under different processing conditions has also been studied by Crawford *et al.*⁵⁶ They observed that unsulfonated SIBS exhibited phase-segregated cylindrical domain morphology, unlike sulfonated SIBS (with sulfonation level of approximately 20%), which showed a non-periodic morphology. They also observed that processes with low evaporation rates enhanced long-range order of the polystyrene domain. Dynamic mechanical analysis (DMA) studies confirmed that SIBS membranes exhibited an increased rubbery plateau (E') and a dramatic reduction in the loss factor ($\tan\delta$) as a result of sulfonic group aggregates, which induce crosslinking of the polymer matrix.

Table 2.2. Examples of sulfonated block copolymers that have been studied as PEMs¹¹.

Polymer Electrolyte Membrane	Attributes
Partially Sulfonated Polystyrene-block Poly(ethylene-ran-butylene)-block-Polystyrene	<ul style="list-style-type: none"> ▪ Aliphatic backbone ▪ Widely available ▪ Low polydispersity index (PDI) ▪ Extensively studied
Partially Sulfonated Poly (styrene-isobutylene-styrene) (S-SIBS)	<ul style="list-style-type: none"> ▪ Aliphatic backbone ▪ Widely available ▪ Low PDI ▪ High selectivity
Partially Sulfonated Poly ([vinylidene-difluoride-co-hexafluoropropylene]-b-styrene)	<ul style="list-style-type: none"> ▪ Fluorinated block
Partially Sulfonated Polystyrenesulfonate-block-Polymethylbutylene (PSS-b-PMB)	<ul style="list-style-type: none"> ▪ Aliphatic backbone ▪ Excellent morphological control ▪ Widely tunable synthesis
Partially Sulfonated Poly(styrene-b-vinylidene fluoride-b-styrene)	<ul style="list-style-type: none"> ▪ Fluorinated center blocks
Poly(hexylmethacrylate)-b-Poly(styrene)-b-Poly(hexylmethacrylate) (PHMA-b-PS-b-PHMA)	<ul style="list-style-type: none"> ▪ Aliphatic backbone ▪ High molecular weight ▪ Sulfonated center blocks
Poly (norbornenylethylstyrene-s-styrene)-Poly(n-propyl-p-styrenesulfonate) (PNS-PSSP)	<ul style="list-style-type: none"> ▪ Aliphatic backbone ▪ Crosslinkable ▪ Latent ionic groups
Poly (arylene ether sulfone)	<ul style="list-style-type: none"> ▪ Aromatic backbone ▪ High chemical stability ▪ Demonstrated fuel cell performance
Poly (arylene ether sulfone ketone) (SPESK)	<ul style="list-style-type: none"> ▪ Aromatic backbone ▪ High chemical stability ▪ Demonstrated fuel cell performance

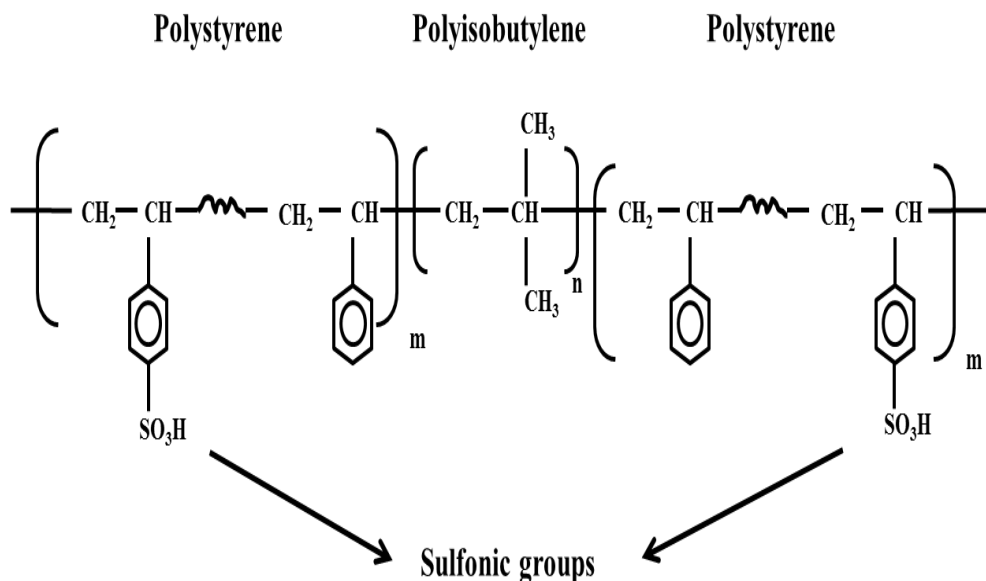


Figure 2.2. Chemical structure of SIBS membranes.

In another study, Napadensky *et al.*¹⁶ fabricated cation-exchanged SIBS membranes in order to evaluate the counter ion effect on swelling and proton conductivity. Results confirmed that double-charged cations (*e.g.* Cu^{+2}) produced more rigid membranes with limited swelling as compared to single-charged cations (*e.g.* Cs^{+1}). They suggest that cations with a higher valence yield higher levels of crosslinking. However, results also showed that excessive crosslinking can dramatically reduce the water uptake, which in turn, can be detrimental for the conduction of protons in fuel cell applications.

2.2. Electrochemical Devices

There are several different kinds of electrochemical devices that can be classified according to the type of electrolyte used and their fabrication process. This section will review some of the previous studies reported on the fabrication, using silicon technology, of micrometer-sized electrochemical devices based on PEMs.

2.2.1 Portable Polymer Electrolyte Membrane Fuel Cells (PEMFCs)

Personal entertainment and communication devices used today such as laptops, cellular phones, tablets, digital cameras, and music players require power sources that are light-weight, have high energy density, and a small form-factor. Portable polymer electrolyte membrane fuel cells (PEMFCs) are strong candidates to replace traditional rechargeable batteries used in devices requiring less than 50 Watts of power.⁵⁷

Portable PEMFCs are typically small open systems, where the fuel (hydrogen, methanol, etc.) is fed and subsequently oxidized at the anode, and the oxidant (*e.g.* air) is fed at the cathode, where it is quickly reduced. In these systems, the electrons flow from the anode to the cathode through an external circuit, thus producing electricity. The solid electrolyte, placed between the two electrodes, provides electronic insulation and carries the proton conduction to complete the circuit. A schematic of a typical fuel cell arrangement is shown in **Figure 2.3**.¹⁵

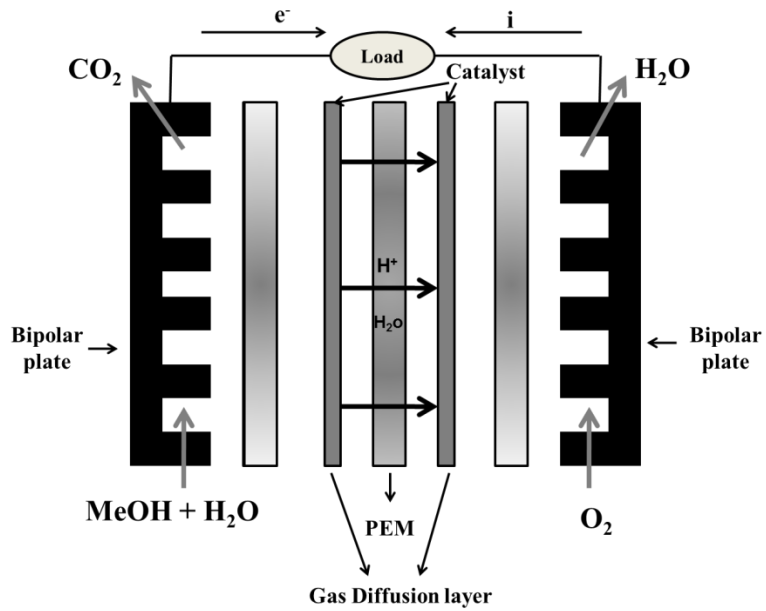


Figure 2.3. Schematic of a Polymer Electrolyte Membrane Fuel Cell (PEMFC) as depicted by Chu *et al.*¹⁵

Global production of portable fuel cells has continuously grown over the last few years. According to the U.S. Department of Energy's 2011 Fuel Cell Market Report⁵⁸, published in July 2012, the total portable fuel cells sold in North America grew by 210% between 2008 and 2011.

Many approaches based on traditional microfabrication techniques have been proposed for the design and fabrication of portable PEMFCs.¹⁷ For example, Jankowski *et al.*⁵⁹ fabricated a two chamber silicon-based μ -PEMFC using Nafion[®]. The specific device design is illustrated in **Figure 2.4**. In this study, the Nafion[®] membrane was spin casted onto an electrode layer previously deposited by sputtering. The cell support was fabricated by patterning silicon wafers using traditional photolithography techniques. A

power density of 37 mW/cm² was obtained for this device under hydrogen fuel supply at 0.45 V and 40°C.

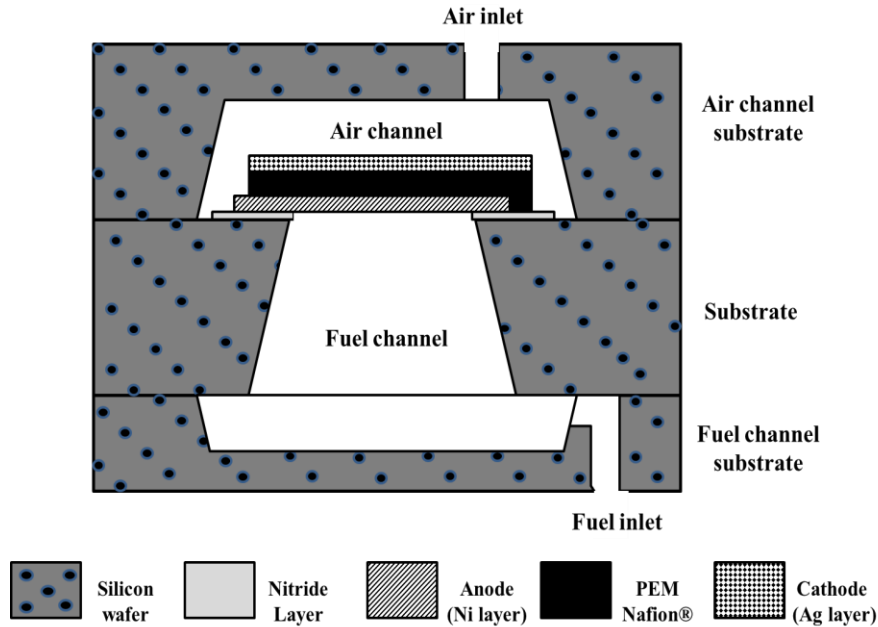


Figure 2.4. Schematic of two chamber design MEMS-based μ -PEMCF proposed by Jankowski and co-workers.⁵⁷

Another research group, Keyur *et al.*¹⁸ have also developed a micrometer-sized hydrogen-air PEMFC on silicon and poly-dimethylsiloxane (PDMS)-based substrates using traditional micromachining techniques such as sputtering, physical vapor deposition, reactive ion etching, and soft lithography. The main objective of this study was to deposit the electrodes directly onto the patterned Nafion[®] membrane using vacuum sputtering in order to simplify the fabrication process and to reduce ohmic losses (*iR*) and metal catalyst loading.

Non-traditional techniques such as nanoimprint lithography (NIL) have also been used in order to prepare fine-line patterned structures with Nafion^{®60}. Zhang *et al.*⁶¹ fabricated micro-convex patterns with diameters of about 600 nm and height of 50 to 70 nm on a Nafion[®] membrane. The structures were fabricated via NIL with silicon templates at 130°C and a platinum layer approximately 20-nm thick was subsequently deposited onto the patterned membrane. The final μ -DMFC device was created by pressing the platinum coated membrane between two micro-channeled silicon plates. The fabricated cell was tested using methanol and air at room temperature. The power density obtained with this prototype was 0.20 mW/cm².

2.2.2. Micro (μ) Sensors

Due to the advancements in silicon technology, it is possible to fabricate very small electrochemical sensors with high sensitivity. Electrochemical micro-sensors use thin film polymer electrolytes as their main component. Many PEMs, especially Nafion[®], have been evaluated as the key electrolyte membrane to detect chemical species such as hydrogen, glucose, CO, H₂, H₂S, and NO_x.^{62,63} For example, in the carbon nanotube/polymer composite-based micro-sensors developed by Lee *et al.*⁶⁴, Nafion[®] plays an important role as the barrier or selective agent, since the carbon nanotubes have high sensitivity but poor selectivity.

In a different micro-sensors application, Star and co-workers⁶⁵ fabricated Nafion[®]-coated carbon nanotube field-effect transistors (CNFETs) for humidity detection. **Figure 2.5** shows a schematic representation of the fabricated CNFET. In this architecture, carbon nanotubes were grown by chemical vapor deposition onto 200 nm of silicon dioxide and

then a 10 nm Nafion[®] membrane was deposited onto the CNFETs by casting from a 0.05 wt% solution. Although relative humidity (RH) is usually related to conductivity, this work demonstrated that it is possible to measure RH from modulation and hysteresis in the conductance of a CNFET by the applied gate voltage.

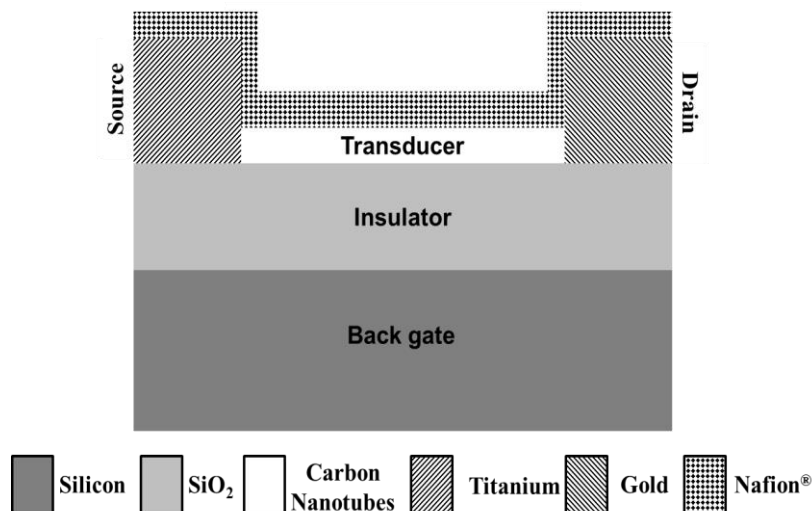


Figure 2.5. Schematic representation of CNFET fabricated by Star *et al.*⁶⁴

Spectroelectrochemical sensors have also been fabricated based on PEM coatings. These devices are usually fabricated by depositing Nafion[®] thin films onto optically transparent substrates. After the analytes (from aqueous solutions) are preconcentrated within the film, these are electrochemically transformed yielding a change in optical signal (absorbance or luminescence), which in turn, is directly related to the analyte concentration.^{66,67}

In biomedicine, the fabrication of implantable glucose micro-sensors (lab-on-a-chip) devices that are highly durable and accurate has also evaluated the use of PEMs such as

Nafion[®].^{68,69,70,71} For example, Kim and co-workers⁷⁰ proposed an amperometric glucose biosensor based on a composite film comprised of sol-gel-derived zirconia and Nafion[®]. The film was used for immobilizing the glucose oxidase enzyme (GO_x) on a platinized glassy carbon electrode. In this case, Nafion[®] was selected because it is biocompatible with the GO_x enzyme and because it serves as a selective barrier (molecular sieve) to eliminate foreign interferences. The results showed that the biosensor responds linearly in the range of 0.03 to 15.08 mM glucose concentration, with a sensitivity of 3.4 μA/mM and a detection limit of 0.037 mM. They also concluded that the presence of Nafion[®] in the composite film helped prevent the interferences from ascorbic acid and uric acid (negatively charged species), which could significantly impact the response of the sensor.

2.2.3. Micro (μ) Actuators

Micro-actuators are microscopic mechanisms (devices) that supply and transmit a measured amount of energy for the operation of another mechanism or system. These mechanisms can be classified as electrostatic, electromagnetic, piezoelectric, fluid, and/or thermal. Generally, micro-actuators are based on a membrane electrode assembly (MEA), which can generate a large deformation when a low voltage is applied. MEAs consist of a thin polymer electrolyte membrane (*e.g.*, Nafion[®]) covered on both sides with noble metal layers as the electrodes. The electrostatic interactions associated with charge transport within the MEA lead to a bending motion and hence, an actuation effect. Since MEA-based micro-actuators work well in both, air and aqueous media, these prototypes are very

attractive for many applications such as microfluidic, biomedical, and biomimetic robots.¹⁹

A prototype MEA-based micro-actuator was developed by Zhou *et al.*⁷² using a commercial Nafion[®] solution. The MEA, composed of Au/Nafion/Au film layers, was fabricated on a silicon wafer using the process flow illustrated in **Figure 2.6**. The dimensions of the micro-actuator were 200 μm wide, 400 μm long, and 0.2 μm thick. Testing concluded that these devices could be fully actuated in water at DC voltages on the order of approximately 3V.

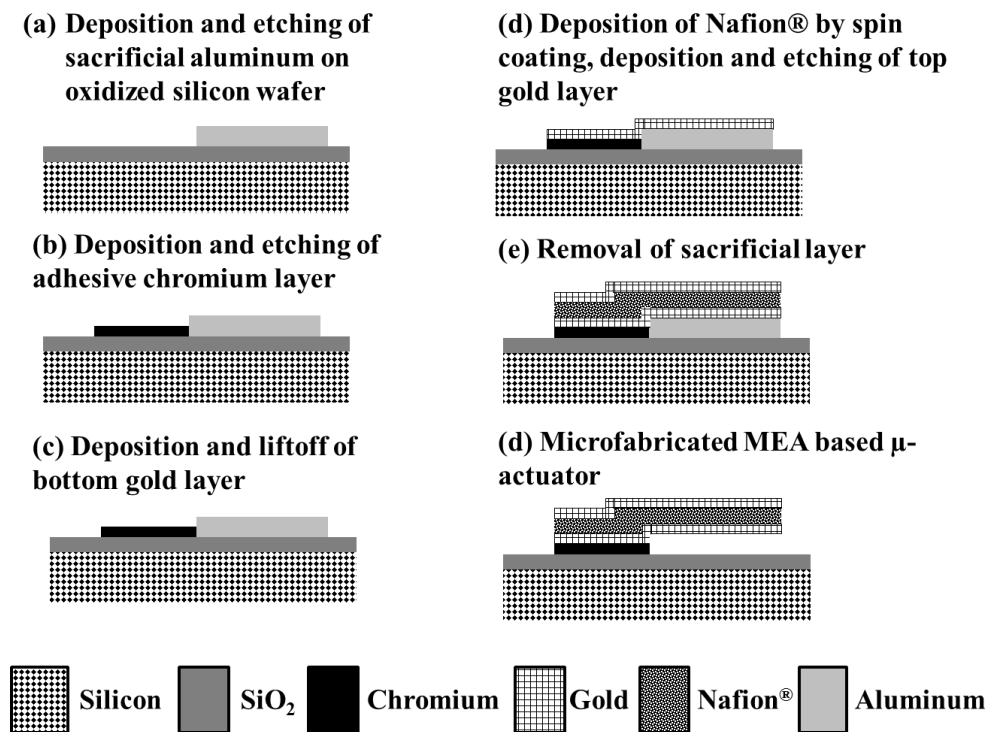


Figure 2.6. Process flow used by Zhou *et al.*⁶⁹ for the fabrication of a Nafion[®] micro-actuator.

2.3 Polymer Electrolyte Thin Films

Conventional μ -PEMFC devices are fabricated using electrolyte membranes with thickness values on the order of 20 to 30 μm . However, much thinner electrolyte membranes (thin films) are required in order to reduce the size of the devices and their ohmic losses.¹⁵

Polymer electrolyte thin films can be deposited using a variety of techniques such as painting, spin-coating, printing, dip coating, solution casting, and layer-by-layer assembly.⁷³

Spin-coating is one of the preferred methods due to its low cost and ease of use. However, fabrication of homogeneous electrolyte thin films via spin-coating can be a true challenge as a result of two competing effects: (1) the formation of PEM aggregates (or micelles), which occurs even at very low polymer concentrations, and (2) the applied shear forces and high evaporation rates generated in this process, which can drive the micellar solution away from thermodynamic equilibrium.⁷⁴

Despite the difficulties, many PEM thin films have been deposited via spin-coating with excellent results. **Table 2.3** summarizes some of the PEM materials that have been deposited using spin-coating and the variety of processing conditions and materials characterization techniques that were used to evaluate the thin films.

Table 2.3. Summary of studies focused on polymer electrolyte thin films fabricated via spin coating.

Ionomer Precursor	Solvent	Subst.	Characterization techniques	Ref.
5% Polystyrene-block-poly(ethylene-ran-butylene)-block-polystyrene (S-SEBS) solution in 1-propanol and dichloroethane.	2-propanol	Quartz ITO Gold	Peel-off test Ellipsometry Contact angle Voltammetry	64
Poly(styrene-ran-styrenesulfonate) P(S-SS _x)	Toluene/THF system	Silica	SAXS STEM	75
Polystyrene-block-poly(ethylene-alt-propylene) (PS-PEP)	THF	Silica	AFM	76
Poly(4-ammonium styrene sulfonic acid)	Water Cyclopentanone	Silicon dioxide	X-ray reflectometry Quartz Crystal Microbalance (QCM)	77
Dow® Perfluorinated Polymer membrane	Water/ethanol system	Silicon	Neutron reflectometry AFM	78
Sulfonated Polystyrene	Toluene/methanol, and THF/methanol systems	Silicon	AFM SEM Contact angle SAXS Ellipsometry	70
Poly(styrene sulfonate-b-methylbutylene) (PSS-PMB)	THF	Silicon	Ellipsometry AFM GISAXS	79
Poly(n-vinyl carbazole) (PVK)	Toluene Benzene THF Chloroform	ITO	X-ray reflectometry AFM SEM Contact angle	80
Nafion® solution in lower aliphatic alcohols and 34% water	-	Silicon	Four-point probes load-cell	81
Nafion® solution in lower aliphatic alcohols and 10% water	-	Glass	Spectrophotometry Ellipsometry Refractometry	82
Sulfonated Poly(styrene-ethylene/propylene-styrene)	Toluene/Methanol system (95/5 w/w)	Silicon	AFM	83

For example, Park *et al.*⁸² studied the domain orientation in thin films fabricated from poly(styrene sulfonate-b-methylbutylene) copolymers (PSS-PMB). For these studies, various PSS-PMB thin films with thickness values on the order of 180 nm and sulfonation percents of 25 and 49 mol% were deposited onto silicon wafer substrates via spin-coating. The surface morphology of the films was evaluated using atomic force microscopy

(AFM), whereas grazing-incidence small-angle x-ray scattering (GISAXS) and transmission electron microscopy (TEM) were used to determine the domain orientation within the films. They found that regardless of the sulfonation percent, all of the films exhibited a phase separated morphology composed of hexagonally-packed cylinders of PMB embedded in a continuous PSS matrix. They also observed that the PMB domain size increased from 22 to 23 nm as the sulfonation percent increased from 25 to 49 mol%.

Similarly, Gromadzki and co-worker⁷⁹ investigated the phase separated morphology of spin-coated sulfonated polystyrene-block-poly(ethylene-alt-propylene) (PS-PEP) thin films via AFM. They observed a morphological transition from a short-range order lamellar structure to a completely disordered morphology as the sulfonation percent increased from 0 to 45%. They also reported that the domain size increased from 60 to 70 nm with a variation in the sulfonation percent from 0 to 27%.

It is also important to note that the complete fabrication of micrometer-sized electrochemical devices requires a lot more processing steps besides the thin film deposition. Other microfabrication techniques such as sputtering, reactive ion etching (RIE), and photolithography are also typically required and the materials properties of the electrolyte film must not be affected by exposure to these processes.^{84,85,86,87} Previous reports on Nafion[®] films suggest that it could be a critical issue when trying to integrate the electrolyte material with traditional silicon microfabrication technology.^{18,19,20,21} For example, Wainrigh *et al.*²⁰ used different solvents in an attempt to increase the viscosity of Nafion[®] solutions so that thicker films could be fabricated. They observed that solvents such as isopropanol and dimethylsulfoxide (DMSO) increased the film thickness but

dramatically reduced the proton conductivity of the Nafion[®] film, whereas ethylene glycol had no effect on it.

As mentioned before, this study focuses on the fabrication and characterization of SIBS thin films for potential applications in microelectrochemical devices. According to the main objectives proposed for this research project, this dissertation was systematically divided as follows. **Chapter 3** covers the project methodology, which includes the thin film fabrication process as well as a brief description of the materials characterization techniques used in this investigation. **Chapter 4** contains the most relevant results concerning the thin film quality and thickness characterization of the SIBS thin films. In turn, the results pertaining to the chemical and morphological characterization of the fabricated films are presented and discussed in **Chapter 5**. The results for the mechanical and adhesion characterization of the SIBS thin films are presented and discussed in **Chapter 6** and **Chapter 7**, respectively. Finally, **Chapter 8** describes the most relevant conclusions and **Chapter 9** provides some recommendations for future work.

CHAPTER 3

PROJECT METHODOLOGY

This chapter presents the sample fabrication procedure as well as the techniques used for the characterization of the materials properties of the SIBS thin films.

3.1. Sample Preparation

3.1.1. Materials

The unsulfonated SIBS polymer used in this work was acquired from Kuraray Co., Ltd., Tsukuba Research Laboratories with the following specifications: 30.84 weight-percent (wt%) styrene, 0.95 specific gravity, $M_w = 71,920$ g/mol, $M_n = 48,850$ g/mol, and polydispersity index (PDI) of 1.47. The SIBS polymers were sulfonated using the procedure suggested by Elabd *et al.*⁵³ and the specific sulfonation mole percent was calculated based on the elemental analysis results obtained from Atlantic Microlab, Inc. (Norcross, GA). The sulfonation percents used in this study were: 0% (SIBS00), 20% (SIBS20), 45% (SIBS45), 70% (SIBS70), and 80% (SIBS80). Nafion[®] perfluorinated resin solution (34 wt. % in lower aliphatic alcohols and water) was purchased from Sigma-Aldrich. The solvents used were hexyl alcohol (Aldrich Reagent grade, 98%), toluene (Fisher Scientific optima, 99.9%), and isopropyl alcohol (Alfa Aesar, 99.5%). Silicon wafers were purchased from Addison Engineering, Inc. (San Jose, California) and used as received.

3.1.2. Thin Film Fabrication Process

The fabrication process used to prepare the films included several steps. The first step was to dissolve the SIBS polymers in an appropriate solvent system. A combination of two solvents was needed to properly dissolve the sulfonated polymers. A polar solvent, hexyl alcohol, was used to dissolve the SIBS hydrophilic part (the one containing sulfonic groups) and a non-polar solvent, toluene, was used for the hydrophobic part. These were mixed at a ratio of 85:15 volume by volume (v/v) solution and stirred for 15 minutes. Similarly, the Nafion[®] solution was mixed with isopropyl alcohol in a ratio of 60:40 volume by volume (v/v) and subsequently stirred for 1 hour. After preparing the solutions, the films were deposited via spin-coating onto silicon wafer substrates using a CEE 200 Spin-Coating system from Brewer Science, Inc. The samples were spun at 2000 RPM for 30 seconds. The films were then soft baked in a hot plate at 50°C for 2 minutes and dried in an oven at 60°C for 48 hours. Some of the films were also thermally-annealed in an oven at 130°C for 98 hours following a procedure similar to the one described by Puskas.⁸⁸

The samples were labeled using the following nomenclature: SIBSXX-Y, where XX corresponds to the sulfonation percent of the polymer and the Y indicates the polymer concentration used. Letters A, B, C, and D correspond to 2.5 wt%, 5 wt%, 10 wt%, and 7 wt% polymer concentration, respectively. For example, sample SIBS80-A has a sulfonation percent of 80% and was fabricated at 2.5 wt% polymer concentration. The additional * symbol that appears for some of the samples indicates that the sample was thermally-annealed. Similarly, the symbol † was used to differentiate the SIBS00-A

samples fabricated from pure toluene. **Table 3.1** shows the specific processing conditions used for some of the samples evaluated in this study.

Table 3.1 Processing conditions used for the fabrication of SIBS and Nafion[®] thin films.

Sample	Polymer Concentration (wt%)	Sulfonation Percent (%)	Thermal Annealing Treatment
SIBS00-A	2.5	0	No
SIBS00-A*	2.5	0	Yes
SIBS00-A [†]	2.5	0	No
SIBS00-A ^{†*}	2.5	0	Yes
SIBS20-A	2.5	20	No
SIBS20-A*	2.5	20	Yes
SIBS45-A	2.5	45	No
SIBS45-A*	2.5	45	Yes
SIBS70-A	2.5	70	No
SIBS80-A	2.5	80	No
SIBS80-A*	2.5	80	Yes
SIBS00-B	5	0	No
SIBS20-B	5	20	No
SIBS45-B	5	45	No
SIBS70-B	5	70	No
SIBS80-B	5	80	No
SIBS00-C	10	0	No
SIBS20-C	10	20	No
SIBS45-C	10	45	No
SIBS45-D	7	45	No
Nafion [®]	-	-	No

3.1.3. Hydration Process

In order to study the hydration effect on the mechanical properties of SIBS and Nafion[®] thin films, some of the samples were exposed to saturated water vapor in a home-made humidity chamber. Due to the temperature sensitivity of these samples, they were pasted

at room temperature (using LOCTITE[®] super glue) onto silicon wafer pieces previously mounted onto 1.25-inch diameter metal stubs. An image of the mounted samples appears in **Figure 3.1**. After sample preparation, the humidity chamber was placed on a hot plate at 35°C and then, 100 mL of liquid water (vapor source) was poured into the chamber. The mounted samples were placed inside the chamber for a period of 12 hours. **Figure 3.2** shows the experimental setup for the humidity chamber.

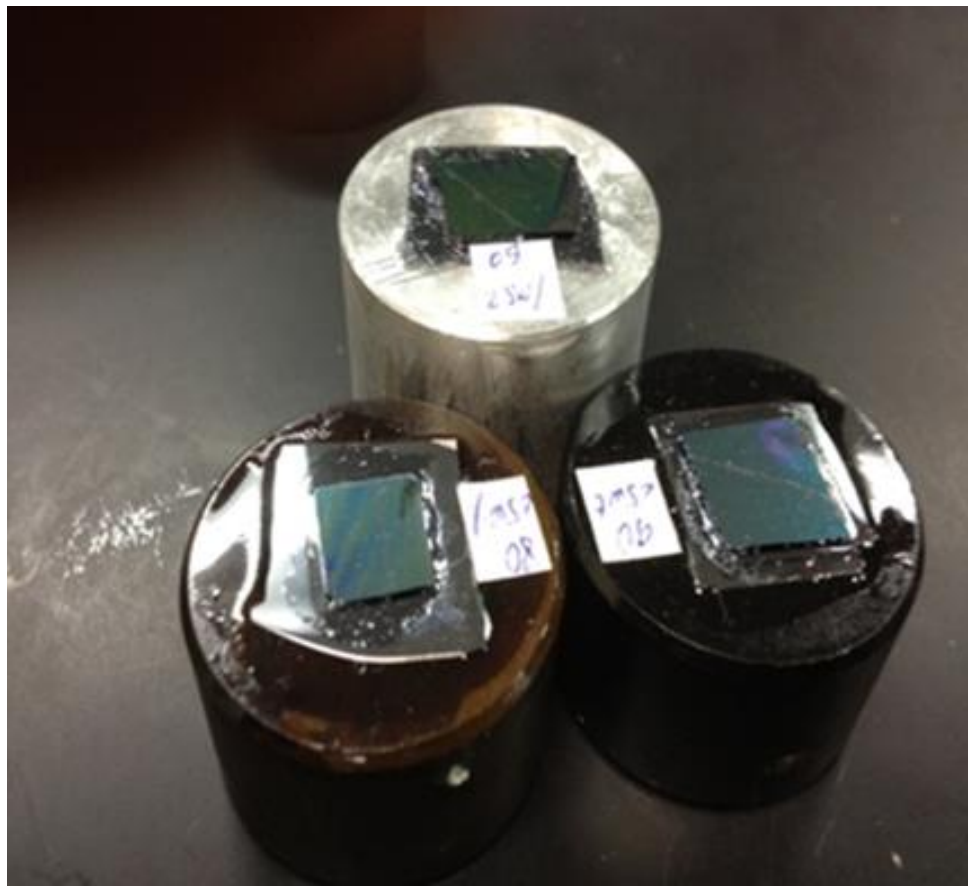


Figure 3.1. Image of nanoindentation samples ready to be hydrated.

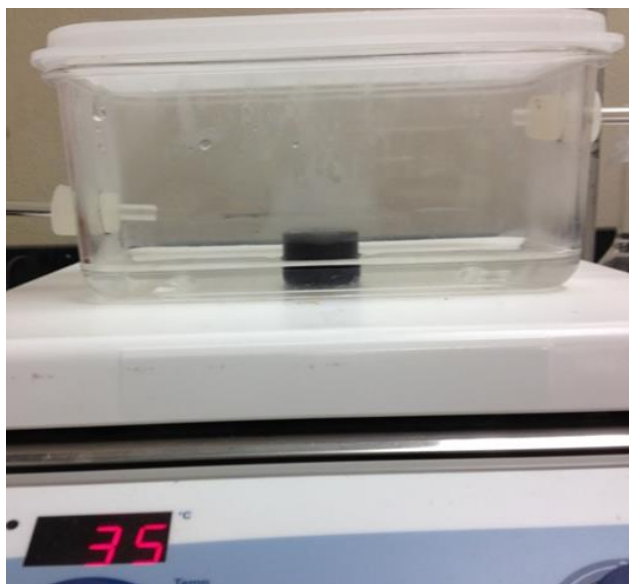


Figure 3.2. Experimental setup used to hydrate the thin film samples.

3.1.4. Membrane Electrode Assembly Fabrication Process

Membrane Electrode Assemblies (MEAs) were fabricated in order to study the adhesive properties of the SIBS thin films and to compare with Nafion[®] films. **Figure 3.3** shows the process flow used for the fabrication of the MEAs. First, a titanium (Ti) thin film of approximately 45 nm thick was deposited onto the silicon wafer substrate via sputtering using an AJA International, Inc. ORION-5-HV sputtering system. The sputtering time and power were set at 5 minutes and 250 W, respectively. The Ti layer was used to improve the adhesion of the palladium (Pd) thin film to the silicon wafer substrate. In the next step of the MEA fabrication, a 1- μm thick Pd film (electrode) was sputtered onto the Ti layer at 100 W for 60 minutes. Finally, the SIBS and Nafion[®] thin films were deposited onto the electrodes via spin-coating according to the procedure described in section 3.1.2.

Table 3.2 lists the process conditions used to fabricate the various MEAs used in this study.

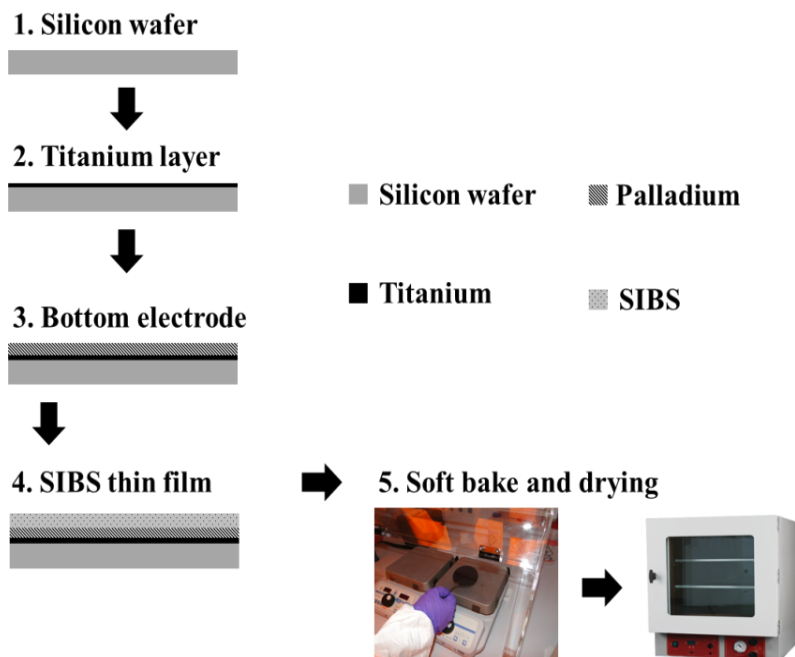


Figure 3.3. Process flow for the MEA fabrication.

Table 3.2. Process conditions used for the MEA fabrication.

SAMPLE	Polymer Concentration (wt%)
SIBS00-C	10
SIBS20-C	10
SIBS45-B	5
SIBS45-C	10
SIBS45-D	7
SIBS80-B	5
Nafion [®]	-

3.2. Materials Characterization Techniques

3.2.1. Optical Microscopy

The quality of the spin-coated films fabricated in this study was evaluated using an inverted optical microscope with model # EPIPHOT 200 from Nikon Corporation. The images were captured using a SCOPTEK® Minisee 1.0 digital camera at different magnifications and processed with the Paint.NET v3.5.8 software.

3.2.2. Profilometry

The film thickness was measured using a P6 Profiler from KLA-Tencor®. For this purpose, a small scratch was made in the films with a razor blade and the step-height difference with the substrate surface was recorded as the film thickness. The process was repeated in several regions of the film to average the results. The measured data was processed with the Apex software from KLA-Tencor®.

3.2.3 Atomic Force Microscopy (AFM)

A DPN 5000 atomic force microscope from NanoInk, Inc. was used in tapping mode to obtain topography and phase images of the spin-coated films. The experiments were performed at room temperature using P-MAN-SICC-0 silicon tips (Pacific Nanotechnology, Inc.) with a spring constant of 40 N/m. The data collected was analyzed using the SPIP® 5.1.8 software from Image Metrology, Inc. Fast Fourier Transform (FFT) images were also acquired using this software.

3.2.4. Fourier Transform Infrared Spectroscopy (FTIR)

FTIR was used to verify the presence of sulfonic functional groups in the SIBS thin films. Infrared (IR) spectra were collected in a Shimadzu IR Affinity-1 FTIR Spectrometer. The attenuated total reflection (ATR) setup was used for samples deposited onto silicon wafer substrates. A blank silicon wafer was used as the background. The spectral range used for these studies was from 600 to 4000 cm^{-1} with a resolution of 4 cm^{-1} and 100 scans per sample.

3.2.5. Differential Scanning Calorimetry (DSC) and Thermogravimetric Analysis (TGA)

The glass transition temperature (T_g) as well as other thermal transitions of the SIBS polymers were evaluated using a TA Instruments Q20 Differential Scanning Calorimeter (DSC). For these studies, the samples were heated from 40 to 200°C at a rate of 5°C/min, followed by a cooling step to 40°C, and a final re-heating step to 200°C at a rate of 5°C/min.

The thermal stability of the SIBS polymers was examined using a Mettler Toledo® thermogravimetric analyzer (TGA) operating with constant nitrogen flow. For these studies, the samples were heated from room temperature to 500°C at a rate of 10°C/min.

3.2.6. X-ray Diffraction (XRD)

The X-ray diffraction technique was used to obtain information about the microstructure of the fabricated SIBS thin films. A Siemens D5000 X-ray diffractometer outfitted with a Cu- κ target ($\lambda = 1.5418 \text{ \AA}$) was used to collect the corresponding thin film diffraction

patterns. The anode was operated at 30 kV of power and 30 mA current using a scanning speed of 6°/min and a step of 0.01° in the 5° to 90° 2 θ range.

3.2.7. Nanoindentation

In the last few years, the nanoindentation technique has become very attractive since it can be used to evaluate the mechanical properties of a variety of materials at the nanometer scale. In fact, previous reports indicate that nanoindentation has been successfully used to measure the mechanical properties of a broad variety of materials including metals, alloys, ceramics, semiconductors, polymers, and composite materials.^{89,90,91,92}

During a nanoindentation experiment, a controlled load (usually on the order of mN) is applied to the indentation tip in contact with the sample's surface. As the applied load increases, the indenter continuously penetrates the sample and after the maximum load is reached, the indenter is withdrawn from the sample also in a controlled manner. Usually, the former step is known as the loading segment, whereas the last one corresponds to the unloading segment. After testing, both the elastic modulus and hardness of the material can be calculated using the Oliver and Pharr (O&P) method. In the first step of the method, the contact stiffness (K_c) is calculated as the slope of the load-displacement curve at the beginning of the unloading segment, where all the deformation can be considered elastic. Finally, the hardness and the apparent elastic modulus of the material can be calculated using a series of equations (presented later).

Many modifications to the original O&P method^{93,94,95} have been proposed in order to account for indentations made on soft materials, where creep compliance and thermal drift effects could have a significant impact. For example, the continuous stiffness measurement (CSM) technique is one of the most relevant modifications to the original O&P method.^{96,97} CSM allows for the direct measurement of the dynamic contact stiffness (K_c) during the loading portion of the indentation cycle. In this method, a small oscillation is superimposed on the static force and the indenter response is detected by a frequency amplifier, which allows for measuring the mechanical properties as a function of the penetration depth into the materials' surface. Once K_c is determined, the contact depth (h_c) can be calculated from the following equation:

$$h_c = h - \varepsilon P / K_c \quad (3.1)$$

where P is the applied load, h is the total penetration depth, and ε is a geometry constant that depends on the shape of the tip.

If a Berkovich indenter is used, then the contact area (A) can be calculated as:

$$A = 24.56h_c^2 + Ch_c \quad (3.2)$$

where C is an experimental factor determined by indenting on a known material such as fused silica. Subsequently, the reduced modulus (E_r) can be calculated with:

$$E_r = \frac{\sqrt{\pi} K_c}{2 \sqrt{A}} \quad (3.3)$$

And the elastic modulus for the material is calculated from:

$$\frac{1}{E_r} = \frac{(1-\nu^2)}{E} + \frac{(1-\nu_i^2)}{E_i} \quad (3.4)$$

where E and ν are the elastic modulus and Poisson's ratio for the material, respectively, and E_i and ν_i are the corresponding properties for the indenter material (usually diamond).

The hardness (H) of the material can also be calculated from the following equation:

$$H = \frac{P}{A} \quad (3.5)$$

To fully assess the effect of the underlying silicon substrate on the mechanical properties of the thin films, a newly-developed nanoindentation method, specifically designed for thin films, was applied to both, the SIBS and Nafion[®] samples. The results were compared against the traditional CSM testing method previously described.

The new thin film method, developed by Agilent Technologies, Inc. in 2010, is based on the Hay-Crawford model. **Figure 3.4** shows a schematic representation of the model, which assumes the film behaves as a spring connected in parallel with the substrate.^{98,99} Mathematically, when two springs are placed in parallel, they can be considered as one by adding their stiffness. As a result, the Hay-Crawford model can be written as:

$$\frac{1}{\mu_a} = (1 - I_0) \frac{1}{\mu_s + F I_0} + I_0 \frac{1}{\mu_f} \quad (3.6)$$

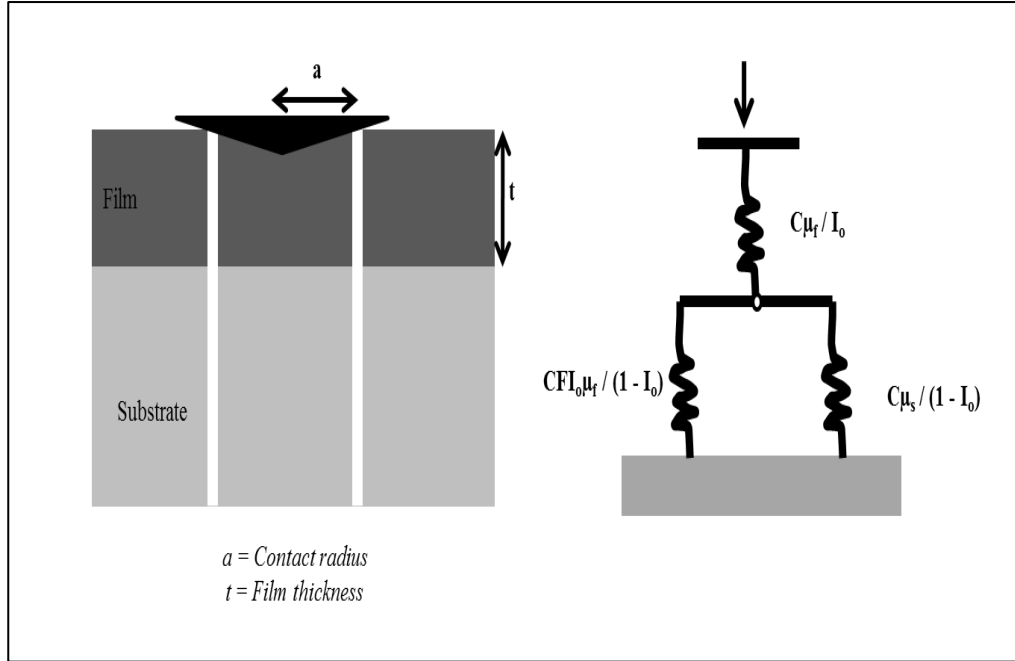


Figure 3.4. Schematic representation of the proposed Hay-Crawford Model.

where μ_a is the apparent shear modulus, and μ_f and μ_s are the shear modulus of the film and the substrate, respectively. In addition, I_0 represents the films' influence, which degrades with depth, and F is a constant calculated by finite element analysis.

The shear modulus of the film can be calculated from the Hay-Crawford equation by solving for μ_f as follows:

$$\mu_f = \frac{-B + \sqrt{B^2 - 4AC}}{2A} \quad (3.7)$$

where,

$$A = FI_0 \quad (3.8)$$

$$B = \mu_s - (FI_0^2 - I_0 + 1)\mu_a \quad (3.9)$$

and

$$C = -I_0 \mu_a \mu_s \quad (3.10)$$

The weighting functions I_0 and I_1 , which govern the film-to-substrate transition for the shear modulus and the Poisson's ratio, respectively, can be calculated as follows:

$$I_0 = \frac{2}{\pi} \arctan \frac{t}{a} + \frac{1}{2\pi(1-v_a)} \left[(1-2v_a) \frac{t}{a} \operatorname{Ln} \left(\frac{1+\left(\frac{t}{a}\right)^2}{\left(\frac{t}{a}\right)^2} \right) - \frac{\left(\frac{t}{a}\right)}{1+\left(\frac{t}{a}\right)^2} \right] \quad (3.11)$$

In the equation for I_0 , t/a represents the ratio of the film thickness to the contact area and v_a , which represents the apparent Poisson's ratio, can be calculated as:

$$v_a = 1 - \left[\frac{(1-v_s)(1-v_f)}{1-(1-I_1)v_f-I_1v_s} \right] \quad (3.12)$$

In the previous equation, v_s and v_f are the Poisson's ratio for the substrate and the film, respectively, and I_1 is a function described by the following equation:

$$I_1 = \frac{2}{\pi} \arctan \frac{t}{a} + \frac{t/a}{\pi} \operatorname{Ln} \left[\frac{1+\left(\frac{t}{a}\right)^2}{\left(\frac{t}{a}\right)^2} \right] \quad (3.13)$$

The apparent shear modulus (μ_a) is obtained from the following equation:

$$E_a = 2\mu_a(1 + \nu_a) \quad (3.14)$$

where the apparent elastic modulus (E_a) is calculated from equation 3.4, whereas the apparent Poisson's ratio (ν_a) is obtained from equation 3.12.

Similarly, the shear modulus of the substrate (μ_s) is calculated by:

$$E_s = 2\mu_s(1 + \nu_s) \quad (3.15)$$

where E_s and ν_s are the elastic modulus and the Poisson's ratio for the substrate, respectively.

Finally, the elastic modulus of the thin film (E_f) can be calculated from:

$$E_f = 2\mu_f(1 + \nu_f) \quad (3.16)$$

For these studies, nanoindentation testing was performed using a G200 NanoIndenter from Agilent Technologies, Inc. with an XP head and a Berkovich tip in order to calculate the hardness and elastic modulus of the films. **Figure 3.5a** displays the G200 NanoIndenter, whereas **Figure 3.5b** and **Figure 3.5c** show the Berkovich tip and the sample stage used for the experiments, respectively.

Indentation testing and data analysis were performed using the NanoSuite[®] software and more specifically, the G-Series CSM thin film method. For these tests, the penetration depth was set at 60% of the total film thickness in order to eliminate issues related with displacements near the surface. A minimum of 240 indentations were made per sample to average the results. The 240 total indentations were divided into 12 arrays (each containing 20 indentations), which were performed at different areas throughout the films. The elastic modulus of the silicon wafer substrate was also calculated via nanoindentation.

All of the tests were performed using the test parameters listed in **Table 3.3**. The nanoindentation experiments required that all samples be mounted onto metal stubs following the procedure described in section 3.1.3 (see Fig. 3.1).

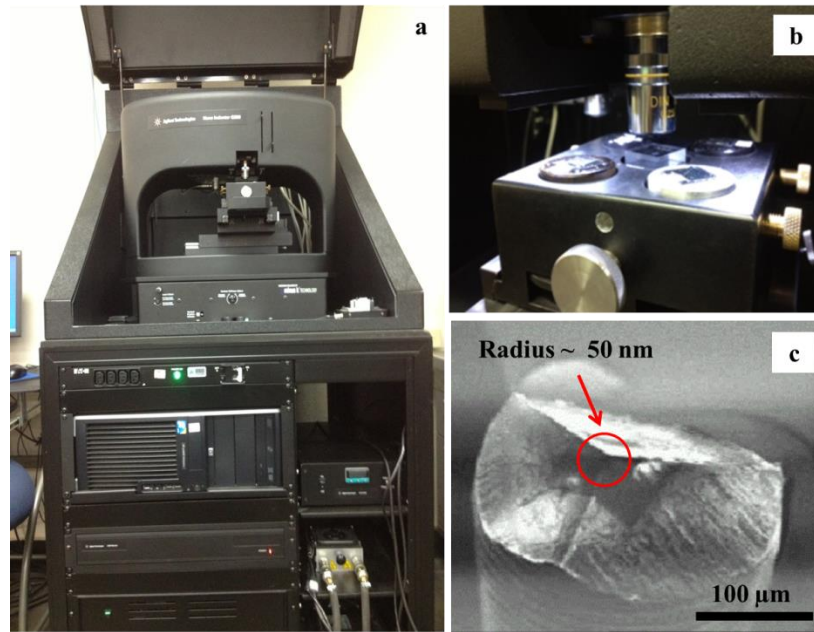


Figure 3.5. (a) Images for the G200 NanoIndenter and (b) the sample tray used for the nanoindentation experiments. Figure 3.5c corresponds to a SEM image of a Berkovich tip, courtesy of Hysitron Inc.

In the present study, the mechanical properties of some SIBS and Nafion[®] thin films were also evaluated at different temperatures. For this purpose, the samples were mounted onto metal disks using an adhesive designed to resist high temperatures (Poly 2000 from Lawson Co.) as shown in **Figure 3.6a**. Subsequently, the samples were screwed on the hot stage which consisted of a thermally insulating ceramic piece bonded to the sample holder, two hose connections for the coolant flow, and a thermocouple (see **Fig. 3.6b**). Also, a heat shield was placed between the indenter head and the stage to prevent damages to the electronic components of the equipment as well as to avoid thermal instabilities of the indenter. After the hot stage was mounted on the nanoindentation equipment, the samples were heated progressively using an automatic temperature

controller. The indentation experiments were performed at seven different temperatures: 30, 50, 70, 100, 130, 150, and 170°C.

Table 3.3. Parameters used for the nanoindentation tests.

Test parameters	
Strain Rate Target	0.05 s ⁻¹
Harmonic Displacement Target	1 nm
Poisson's Ratio, Film	0.35
Poisson's Ratio, Substrate (Silicon Wafer)	0.25
Young's Modulus, Substrate (Silicon Wafer)	178 GPa
Frequency Target	175 Hz

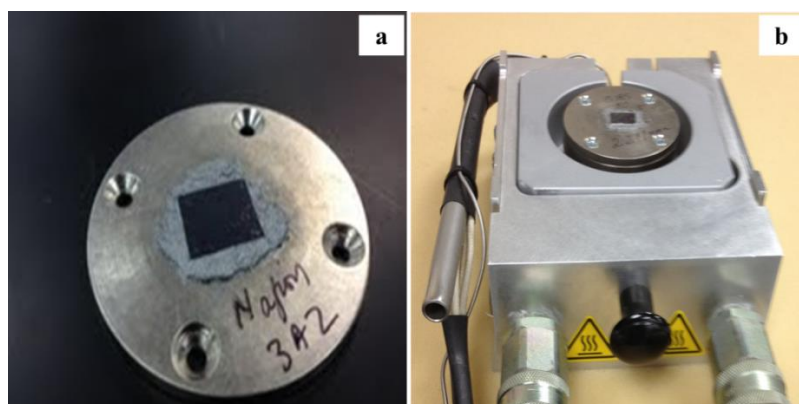


Figure 3.6. Images for (a) the sample mounted on a metal disk and (b) the mounted sample on the hot stage.

The indentation experiments and data analysis were performed using the NanoSuite[®] software described above, but using the NanoSuite[®] G-Series Hot Stage Hardness and Modulus method. Unlike CSM testing, the hot stage method follows the original *O&P* procedure to calculate the elastic modulus and hardness. For the most accurate results, a frame-stiffness correction was performed for each of the experimental temperatures. The penetration depth was set at 25 to 35% of the total film thickness. At each temperature, a

minimum of 10 indentations were made per sample to average the results. **Table 3.4** lists the parameters used for the high temperature nanoindentation tests.

Table 3.4. Parameters used for the hot stage nanoindentation tests.

Test parameter	
Peak Hold Time	1 s
Max. Program Load	0.15 - 0.32 mN
Time to Load	1 s
Poissons Ratio	0.30

3.2.8. Adhesion Testing

As previously noted, the polymer thin films can be potentially used in a wide variety of applications. However, due to their small thickness, these must necessarily be supported by substrates. Unfortunately, during micromachining, these film-substrate systems can be exposed to stresses (*e.g.* polishing, sputtering, etching, etc.) that could deteriorate and/or remove the films.^{100,101} Previous reports also indicate that adhesion can be largely affected by the substrate cleaning process, deposition method, film thickness, film properties, substrate type, substrate temperature, and so forth.^{102,103,104,105,106,107,108,109} Before describing the method used to determine adhesion, it is important to define this property.

3.2.8.1. Adhesion Background

According to the Oxford dictionary, the word “adhesion” comes from the verb “adhaerere” which refers to the action or process of adhering to a surface or object.¹¹⁰ The

term “adhesion” can also be defined as the action of sticking together particles of similar (homohesion) or different substances (heterohesion).¹¹¹

When it comes to the adhesion studies, it is relevant to determine the “locus of failure.” For example, if the break occurs at the film-substrate interphase, then this phenomenon is called an *adhesive failure*, but if the failure takes place within the film (or in the substrate), the event is called *cohesive failure*.^{112,113}

In spite of the definitions presented from a qualitative viewpoint, the reality is that it is very difficult to define “adhesion” in quantitative terms. In the present review, three different approaches are presented to describe adhesion: basic adhesion, reversible adhesion, and practical adhesion.

Basic adhesion refers to the type and strength of binding forces between the film and the substrate.¹¹⁰ These forces are divided into two main groups: chemical bonds and intermolecular forces. The former group comprises the interactions with high binding energies such as ionic, covalent, and metallic bonds. In contrast, the intermolecular forces are distinguished by being the weakest interactions. Notable in this group are the hydrogen bonds and Van der Waals forces (*i.e.*, Debye, Keesom, and London dispersion forces). Unfortunately, from a practical point of view, this definition is not useful, since in most cases, it is very complicated (or impossible) to measure the energies pertaining to each of these types of interactions.

Reversible adhesion, also known as “thermodynamic” adhesion, is also related to the strength of binding forces. However, unlike basic adhesion, the magnitude of these forces is described in terms of fundamental thermodynamic quantities such as surface free

energies.¹¹⁴ The definition of thermodynamic adhesion is based upon the change in free surface energy experienced by the system adhesive-adherend before and after the contact.

In general, the reversible adhesion is defined as follows:

$$W_{AB} = Y_A + Y_B - Y_{AB} \quad (3.16)$$

where W_{AB} is the reversible work of adhesion, while Y_A and Y_B represent the specific surface free energy of substances A and B, respectively. The term Y_{AB} corresponds to the interfacial specific free energy. This model is useful when both A and B are liquids (or when one is solid and the other is liquid), but unfortunately, for systems such as solid thin films deposited on rigid substrates, this definition is impractical because it is very difficult to obtain the specific surface free energy (Y) for solid thin films.

The ASTM defines this particular form of adhesion as “the force or work required to remove or detach a film or coating from its substrate irrespective of the locus of failure”.¹¹² The force of adhesion can be related to work of adhesion as follows:

$$W = \int f(x) dx \quad (3.17)$$

This equation implicitly assumes that changes in force depend on the distance of separation between the surfaces in contact.¹¹⁵

Since the practical adhesion is an extrinsic property which depends on the film/substrate properties (*e.g.* hardness, elastic modulus, microstructure, surface roughness, etc.), as well as on the test parameters (loading rates, displacement rates, type of applied force, etc.),

the values of experimental adhesion obtained by different methods may not be directly comparable. It should also be mentioned that the practical adhesion may not be a direct measure of basic adhesion, since the former also includes the work spent in other processes, such as the work required to generate plastic deformation in a film during a scratch adhesion test.¹¹²

Today, there are a variety of methods used to measure the adhesion of thin films. Usually, these methods can be divided into categories that include, among others, destructive and non-destructive methods, qualitative and quantitative tests, and mechanical and non-mechanical methods. However, the mechanical methods are some of the most popular due to their versatility and ease-of-use. These techniques are distinguished by the use of an external force to detach the film from the substrate. These forces can generate detachment of the film in either, the normal or lateral direction to the interface. Mittal¹¹⁰ classified the scratch test methods considering the direction of applied stress as shown in **Table 3.5**.

Table 3.5. Adhesion test methods based upon the application of stress.

Scratch test method	
Normal detachment	Lateral detachment
- Direct pull-off method	- Scotch tape method
- Moment or topple method	- Peel test method
- Ultrasonic method	- Tangential shear method
-	- Scratch or stylus method

3.2.8.2. Scratch Adhesion Testing with Nanoindentation

Within the wide variety of mechanical methods that can be used to measure the adhesion of thin films, the scratch adhesion test is becoming increasingly popular due to its applicability to a broad range of coatings, including but not limited to: ceramic, metals, polymers, and nanocomposites thin films.^{116,117,118,119,120} In addition, the development of high-resolution scratch test systems as well as of simple and standardized scratch test procedures has also helped to popularize this technique.¹²¹ As its name suggests, the scratch adhesion test basically consists of producing controlled damage in a thin film by drawing an indenter of defined geometry across the film surface at constant velocity and using either a constant or progressively increasing normal force.¹²² Then, the resulting damage is assessed by optical microscopy and the normal force which produces a specific type of damage is considered as the critical load.

Usually, a high critical load (required to cause interfacial failure) suggest that there is a good adhesion between the film and the substrate. It should be noted that the scratch adhesion test does not measure the basic adhesion; on the contrary, this method only gives a measurement of the practical adhesion strength of a film-substrate system.¹¹²

Scratch adhesion testing was used to characterize the interfacial adhesion between layers of materials. Specifically in this study, the primary objective was to determine the load (critical load) required to cause adhesion failure between the polymer electrolyte thin films and the sputtered Pd electrodes. A complete description of the MEA prototypes that were used to perform these tests was previously presented in section 3.1.4.

The G200 NanoIndenter was also used to perform the scratch tests. A three-step ramp-load-scratch sequence similar to the one shown in **Figure 3.7** was performed on each MEA. The testing procedure also included a measurement of the lateral force applied during the scratch.

Basically, the test sequence consists of a single line pre-scan of the area to be scratched, followed by the ramp-load scratching step, and a final scan to evaluate the residual deformation.

The tests were performed at room temperature using a tip with cube-corner geometry and under the conditions summarized in **Table 3.6**. A minimum of five tests were carried out per sample to average the results. Finally, scanning electron microscopy (SEM) was used to study the mode of failure exhibited by the film-substrate systems post scratching.

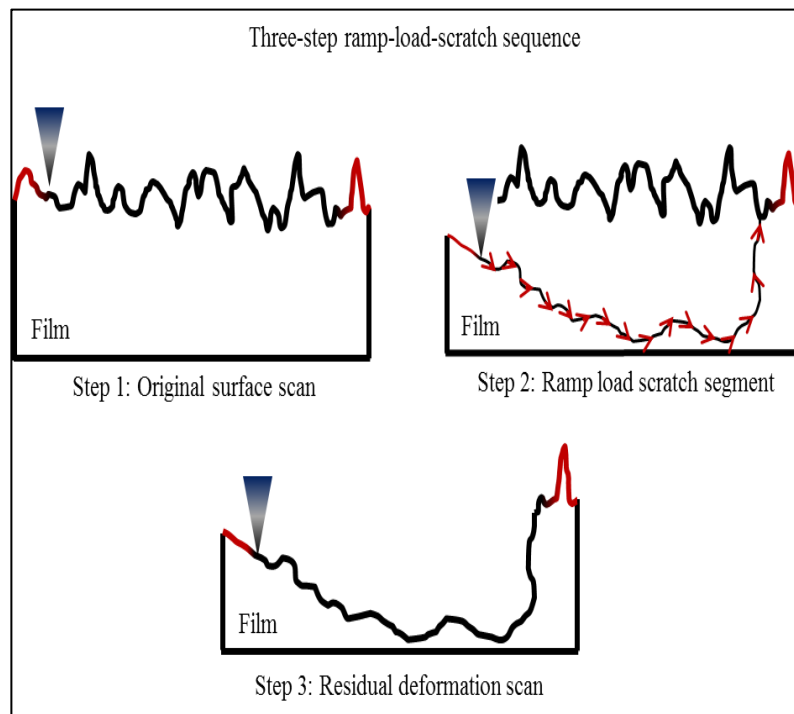


Figure 3.7. Schematic representation of a three-step ramp-load-scratch sequence used for the adhesion testing.

Table 3.6. Parameters used for the scratch adhesion tests.

Experimental conditions	
Scratch length	200 μm
Scratch velocity	20 $\mu\text{m/s}$
Max. scratch load	20 mN
Profiling velocity	5 $\mu\text{m/s}$
Pre and post profile lengths	20 %
Profiling load	0.05 μN
Number of scratches per sample	5

3.2.9 Scanning Electron Microscopy (SEM)

Microscopic examination of the scratch tracks was performed using SEM. The micrographs were obtained using a JEOL-JSM-6930LV scanning electron microscope and employing an accelerating voltage of 5 kV. The images were obtained following standard procedures for low conductive samples.

CHAPTER 4

PHYSICAL CHARACTERIZATION OF SIBS THIN FILMS

The effect of critical variables on the quality as well as the thickness of the spin-coated SIBS thin films are further discussed in this chapter. Some of the main aspects concerning the surface defects observed in these films are also discussed in detail.

4.1. Thin Film Quality

In this study, the effect of processing variables on thin film quality was evaluated. Some of the parameters considered were the solvent system, the sulfonation percent, and the polymer concentration in the films. AFM and optical microscopy were used to evaluate the uniformity and continuity of the films as well as to characterize the different types of defects present at the surface.

The AFM topography images depicted in **Figure 4.1** show solvent system effects on the quality of films fabricated from SIBS00 at 2.5 wt% polymer concentration. Figure 4.1a corresponds to the sample fabricated from a mixture of 85:15 (v/v) toluene and hexyl alcohol, whereas Figure 4.1b shows a film fabricated from pure toluene. Figures 4.1c and 4.1d show a characteristic line profile for each of the surface topographies presented in Figures 4.1a and 4.1b, respectively. The sample fabricated from the solvent mixture (Fig. 4.1a) shows a significant amount of drop-like patterns, which appear to be polymer aggregates randomly distributed across the silicon wafer surface. Furthermore, the profile for this film (Fig. 4.1c) indicates that the aggregates have heights ranging from 140 to 240

nm. The profile also shows some flat segments (as indicated by the arrows in the figure), which likely correspond to areas of the substrate that are not covered with the polymer film. In comparison, the film fabricated from pure toluene (Figs. 4.1b and 4.1d) appears to be more uniform and/or continuous throughout the wafer surface. It is important to note that the profile lines shown in Figures 4.1c and 4.1d have different scales (see Y-axis values). The former exhibits height variations on the order of 200 nm, whereas the last one shows a variation on the order of 8 nm.

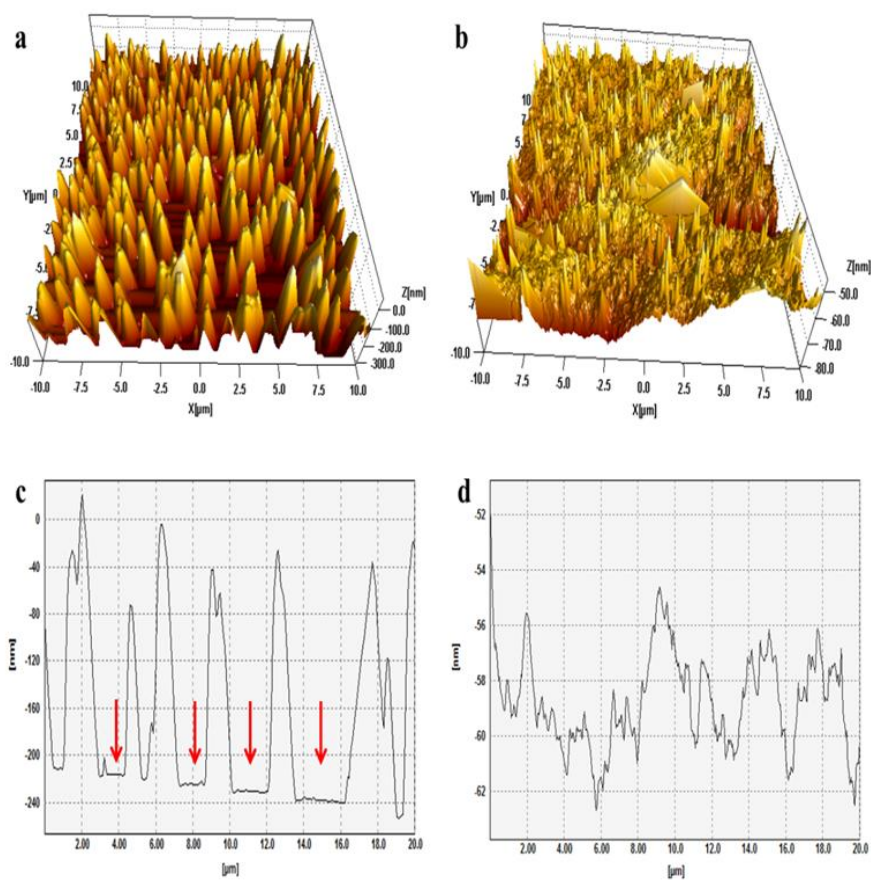


Figure 4.1. AFM topography images for SIBS00 thin films fabricated at 2.5 wt% polymer concentration using: (a) a mixture of toluene and hexyl alcohol, and (b) pure toluene. Figures 4.1c and 4.1d: characteristic line profiles for the films in 4.1a and 4.1b, respectively.

A similar behavior was observed by Xia *et al.*¹²³ for dilute poly(styrene-*b*-ethylene/butylene-*b*-styrene) (SEBS) solutions. They used non-polar solvents with solubility parameters (δ) close to those of the two the polymer blocks in SEBS and the results revealed that the continuity of the films improved when the solvents used had solubility parameters closer to that of poly(ethylene/butylene) (PEB). PEB is the polymer block present in the highest concentration in SEBS.

In the case of samples fabricated from SIBS00 polymer, the mixture of toluene and hexyl alcohol is less compatible as compared to pure toluene likely as a result that the effective solubility parameter (δ) of the mixture with hexyl alcohol ($\delta = 10.5 \text{ (cal/cm}^3)^{1/2}$)¹²⁴ is significantly higher as compared to pure toluene ($\delta = 8.9 \text{ (cal/cm}^3)^{1/2}$)¹²⁰. Therefore, the presence of the alcohol hinders the complete dissolution of the two polymer blocks in SIBS ($\delta_{PIB} = 8.1 \text{ (cal/cm}^3)^{1/2}$ and $\delta_{PS} = 9.1 \text{ (cal/cm}^3)^{1/2}$)¹²⁵ and prevents the formation of a continuous film on the silicon substrate.

The sulfonation percent effects on thin film quality were also investigated. **Figure 4.2** shows AFM topography images for thin films fabricated at 2.5 wt% polymer concentration from a mixture of toluene-hexyl alcohol (85:15 v/v) and SIBS polymers with sulfonation percents of: 20, 45, and 80% (Figures 4.2a to 4.2c). Characteristic line profiles for each of the topographies are presented in Figures 4.2d through 4.2f. In this case, the SIBS20-A film (Fig. 4.2a) shows similar topography as compared to the previously presented SIBS00-A film (Fig. 4.1a). That is, a significant amount of polymer aggregates randomly distributed across the surface. However, the profile for the SIBS20-A film (Fig. 4.2d) shows smaller polymer aggregates and not as many discontinuous regions as with the SIBS00-A film. Therefore, this suggests that the film continuity

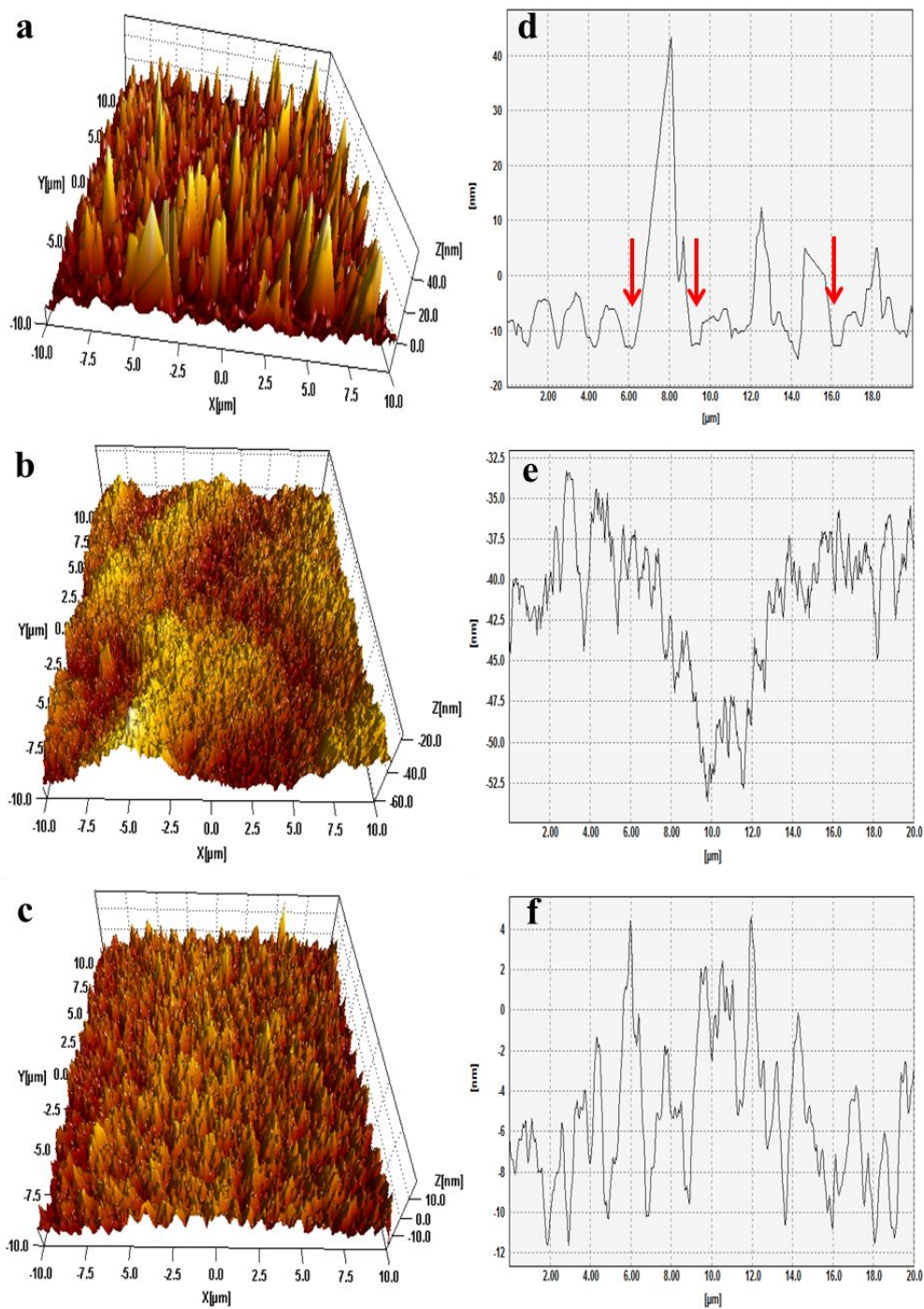


Figure 4.2. AFM topography images of SIBS thin films fabricated at 2.5 wt% polymer concentration from block copolymers with sulfonation percents of: (a) 20, (b) 45, and (c) 80%. Figures 4.2d – 4.2f: line profiles for the films in 4.2a to 4.2c, respectively.

increases with sulfonation % in the range from 0 to 20%. Further enhanced film uniformity or continuity is observed for the SIBS45-A and SIBS80-A films (Fig. 4.2b and 4.2c), which show AFM profiles that are similar to the film fabricated with pure toluene (Fig 4.1b).

A possible explanation for the poor quality of the SIBS20-A film could be that the ratio of hexyl alcohol to toluene in the solvent mixture is too high considering the low sulfonation percent of the polymer. Therefore, to further understand the behavior, a sample of SIBS20 at 2.5 wt% polymer concentration was prepared using a mixture of 99:1 (v/v) toluene and hexyl alcohol.

The results, presented in **Figure 4.3**, support the hypothesis as the continuity of the film is significantly enhanced when the amount of hexyl alcohol is reduced in the mixture.

With regards to the films with higher sulfonation percent, their improved uniformity suggests that physical cross-linking of the poly(styrene) (PS) chains, promoted by higher ionic density, increases the viscosity of the SIBS solutions. This, in turn, favors the formation of continuous films even at low polymer concentrations.

Film continuity is a critical requirement for the application of these polymers into microfuel cells and microsensors as the mechanical and electrical performance of the films could be influenced by it.

Another relevant piece of information that can be obtained from the AFM profiles is an estimation of the surface roughness of the films. For the films that were continuous across the surface, namely SIBS45-A, SIBS80-A, and SIBS20-A processed with the 99:1 (v/v) solvent mixture, the estimated surface roughness for the films was 9.52 nm, 5.54 nm, and 10.63 nm, respectively.

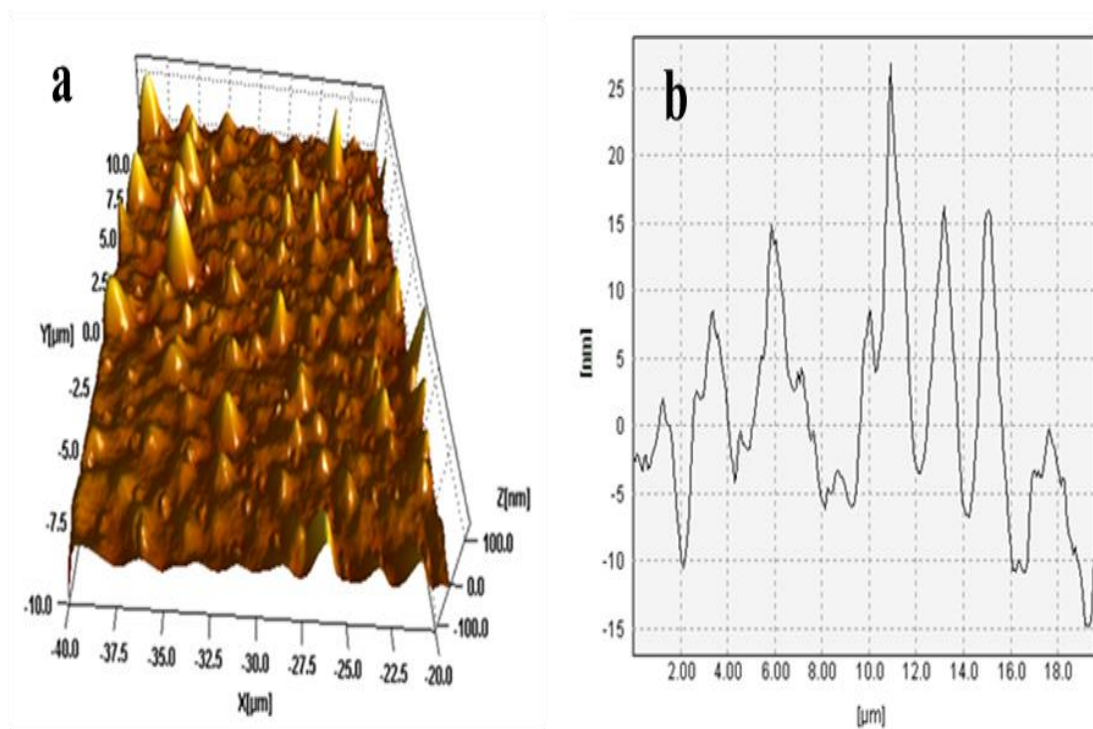


Figure 4.3. (a) AFM topography image for SIBS20 film fabricated at 2.5 wt% polymer concentration and using a mixture of toluene and hexyl alcohol. (b) Corresponding line profile.

Films with higher polymer concentrations were also fabricated in order to study the effect of this processing parameter. **Figure 4.4** shows AFM topography images for thin films fabricated at 5 wt% polymer concentration from SIBS polymers with sulfonation percents

of: 0, 20, 45, and 80% (Figures 4.4a through 4.4d, respectively). All of the images show continuous films deposited on silicon substrates regardless of the sulfonation percent of the block copolymer used. However, noticeable differences between the films can be observed. For the SIBS00-B film (Fig. 4.4a), some polymer aggregates are observed and the estimated surface roughness for the film is 10.01 nm. In comparison, much smoother surfaces are observed for the SIBS20-B, SIBS45-B and SIBS80-B films with surface roughness values on the order of 4.57 nm, 4.01 nm and 4.82 nm, respectively.

In addition, further comparing these results with the ones previously presented for films fabricated at 2.5 wt% polymer concentration (Fig. 4.1a for SIBS00-A and Fig. 4.2a for SIBS20-A) shows an overall improvement in the continuity of the films with an increase in the polymer concentration.

Similarly, **Figure 4.5** displays the AFM topography images for thin films fabricated at 10 wt% polymer concentration from SIBS polymers with sulfonation percents of: 0, 20, and 45% (Fig. 4.5a through 4.5c, respectively).

As suspected, all of the images suggest further improved film continuity as compared to samples prepared at lower polymer concentration. Also, the unsulfonated sample (SIBS00, Fig. 4.5a) still shows a much rougher surface as compared to the others. The surface roughness was measured at 66.60 nm, 2.36 nm, and 5.53 nm for the SIBS00, SIBS20, and SIBS45 films, respectively.

Table 4.1 summarizes the surface roughness values for the films shown in Figures 4.2, 4.4, and 4.5.

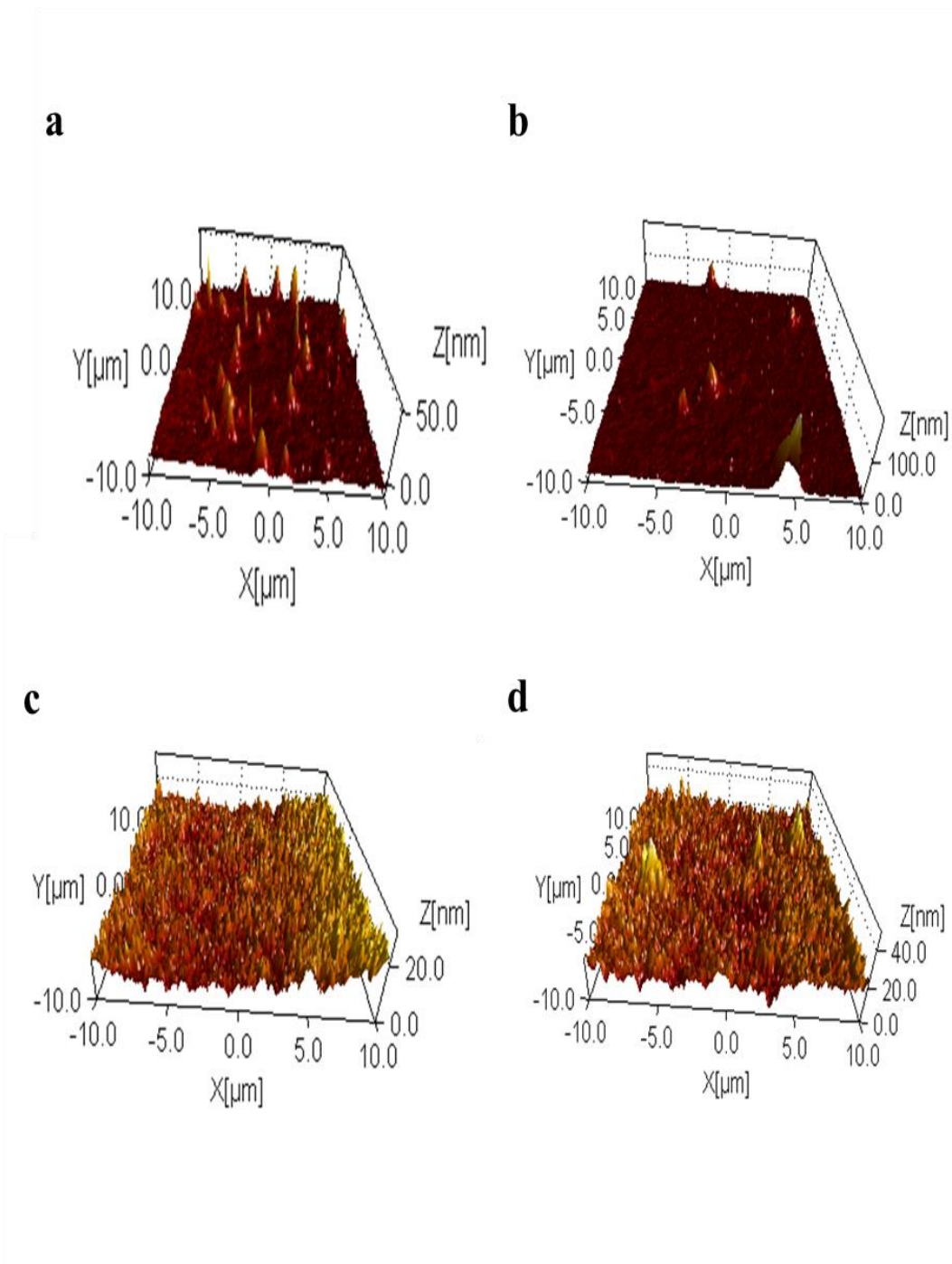


Figure 4.4. AFM topography images for SIBS thin films fabricated at 5 wt% polymer concentration from block copolymers with sulfonation percents of: (a) 0, (b) 20, (c) 45%, and (d) 80%.

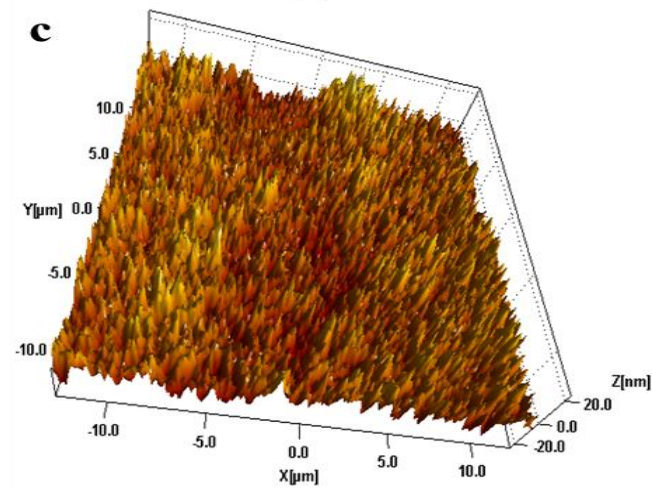
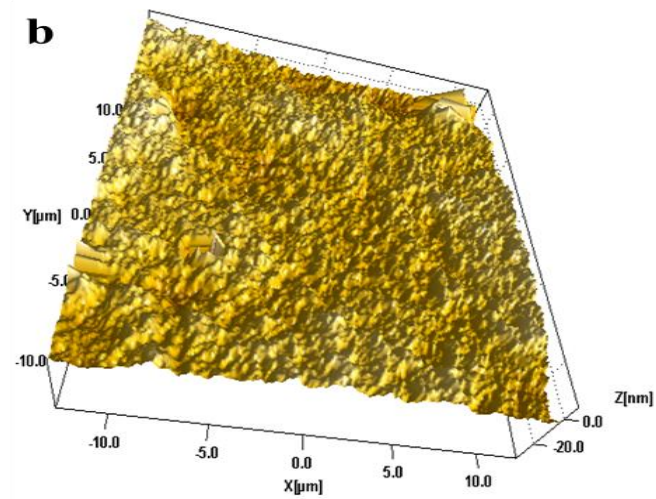
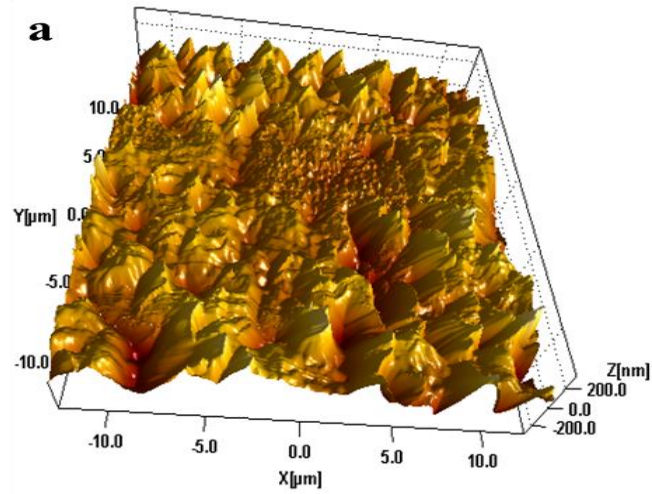


Figure 4.5. AFM topography images for SIBS thin films fabricated at 10 wt% polymer concentration from block copolymers with sulfonation percents of: (a) 0, (b) 20, and (c) 45%.

Table 4.1. Surface roughness measurements for the continuous films.

Sample	Figure	Roughness (nm)
SIBS45-A	4.2b	9.52
SIBS80-A	4.2c	5.54
SIBS00-B	4.4a	10.01
SIBS20-B	4.4b	4.57
SIBS45-B	4.4c	4.01
SIBS80-B	4.4d	4.82
SIBS00-C	4.5a	66.60
SIBS20-C	4.5b	2.36
SIBS45-C	4.5c	5.53

Further analysis of the fabricated films using optical microscopy shows the formation of several defects throughout the surface of the films. **Figure 4.6** shows the optical microscopy images for SIBS thin films processed at different polymer concentrations and sulfonation percent. Figures 4.6a through 4.6c correspond to films fabricated at 2.5 wt% polymer concentration from SIBS polymers with sulfonation percents of 0, 45, and 80%,

respectively. Similarly, Figures 4.6d through 4.6f show the corresponding films fabricated at 5 wt% polymer concentration.

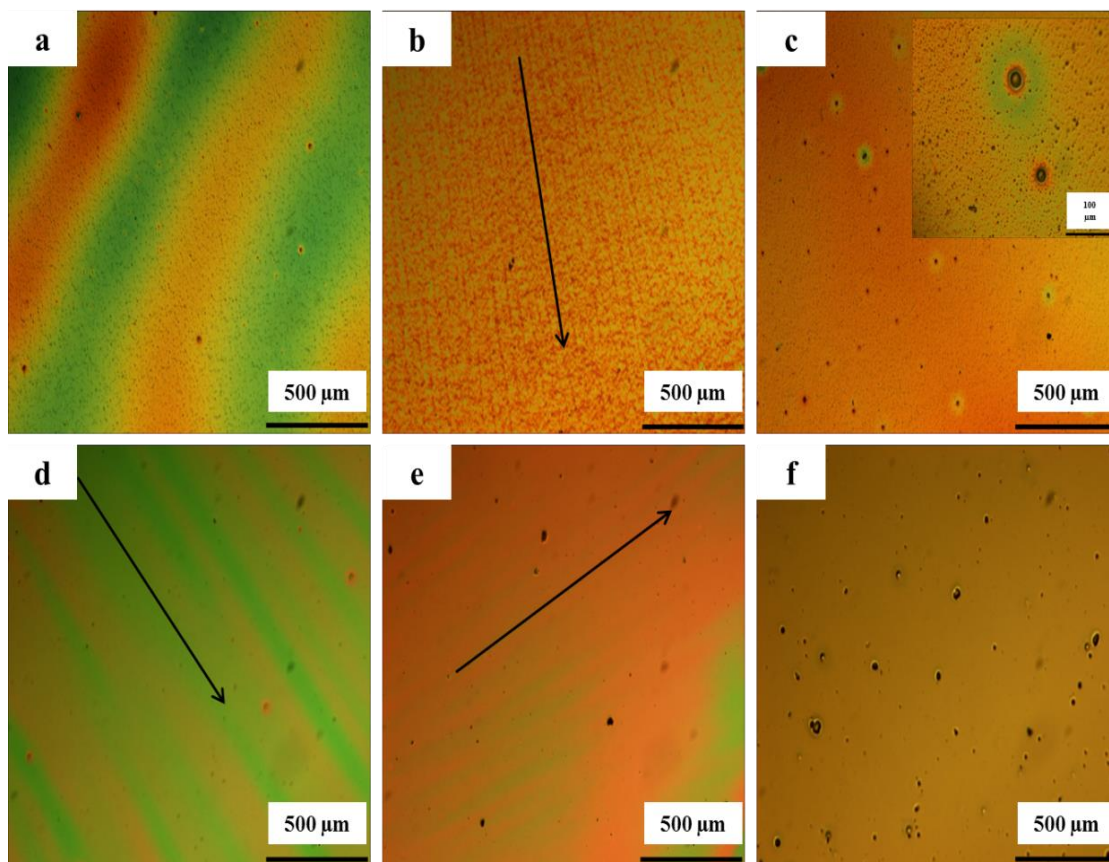


Figure 4.6. Optical microscopy images for SIBS thin films fabricated from polymers with sulfonation percents of 0, 45, and 80%. Figures 4.6a to 4.6c at 2.5 wt% polymer concentration. Figures 4.6d to 4.6f at 5 wt% polymer concentration, respectively.

Figures 4.6a through 4.6c correspond to films fabricated at 2.5 wt% polymer concentration from SIBS polymers with sulfonation percents of 0, 45, and 80%, respectively. Similarly, Figures 4.6d through 4.6f show the corresponding films fabricated at 5 wt% polymer concentration.

The results show a characteristic defect in the form of pin holes for all the films, but the defect concentration increases with sulfonation percent regardless of the polymer concentration used to fabricate the films. In addition, the insert in Figure 4.6c shows the relative size of the defects, which appears to be in the micrometer range.

The formation of these defects throughout the SIBS films could be the result of high evaporation rates of both, solvent and moisture, promoted during the spin coating process and the subsequent “soft-bake” step.

Due to the fact that the hygroscopic nature of SIBS increases with sulfonation percent,^{126,127} it is likely that solutions prepared from SIBS polymer at 80% sulfonation result in higher levels of absorbed moisture, which in turn, induces the formation of additional pin holes.

Even though pin-hole formation is a common problem in spin-coated films, identifying ways to reduce their appearance is important as they are related to one of the most common failure modes observed in PEM fuel cells and sensors, fuel crossover.¹²⁸

Another characteristic defect observed in the SIBS films was “striations”. These are generally observed as a result of differences in surface tension throughout the film during the spin coating process and the phenomenon is known as “Marangoni effects”.^{129,130,131}

The formation of oriented striations can be observed in **Figure 4.6** where the black arrows are used to indicate the direction of the flow or the ridge orientation. Since these defects are wavy in nature, the brightness contrast observed in the images corresponds to height differences in the films. Although this type of defect is also characteristic of spin-coated films, understanding their relative size is critical as they determine the surface

roughness of the films, and could ultimately impact the adhesion of SIBS thin films to the different substrate and electrode materials.

4.2. Thin Film Thickness

After the fabrication process, the thickness of the films was measured using a surface profiler. **Table 4.2** summarizes the thickness measurements for some of the films fabricated in this study.

Table 4.2. Thickness measurements for thin films fabricated using different process conditions.

Sample	Polymer Concentration (wt%)	Sulfonation Percent (%)	Film Thickness (μm)
SIBS00-A [†]	2.5	0	0.238 ± 0.017
SIBS45-A	2.5	45	0.293 ± 0.005
SIBS70-A	2.5	70	0.357 ± 0.010
SIBS80-A	2.5	80	0.362 ± 0.007
SIBS00-B	5	0	0.688 ± 0.011
SIBS20-B	5	20	0.703 ± 0.007
SIBS45-B	5	45	0.753 ± 0.011
SIBS70-B	5	70	1.644 ± 0.086
SIBS80-B	5	80	1.817 ± 0.033
SIBS00-C	10	0	1.618 ± 0.050
SIBS20-C	10	20	2.029 ± 0.059
SIBS45-C	10	45	2.964 ± 0.060
SIBS45-D	7	45	1.165 ± 0.026
Nafion [®]	-	-	1.528 ± 0.070

The results show an overall film thickness variation in the range of 0.24 to 2.96 μm , which is an indication that the process variables had a significant effect on the thickness. For example, at high polymer concentration (10 wt%), the film thickness increased from an average value of 1.62 to 2.96 μm with an increase in the sulfonation percent from 0 to 45%. Similarly, at 5 wt% polymer concentration, the film thickness increased from 0.69 to 1.82 μm in the sulfonation range from 0 to 80%, respectively.

The increase in film thickness as a function of sulfonation percent is likely also a result of the increased viscosity observed in the SIBS solutions as a higher degree of cross-linking is promoted in the presence of higher ionic content. Profilometry results also indicated that, as expected, film thickness increases with polymer concentration. The films fabricated at 10 wt% polymer concentration are approximately 10 times thicker as compared to films with 2.5 wt% polymer concentration.

4.3. Summary

Uniform and continuous SIBS thin films with different sulfonation percents were successfully deposited onto silicon wafer substrates via spin coating using a variety of processing conditions. The effects of critical process variables such as polymer concentration, the solvent system used to fabricate the films, and the sulfonation percent were evaluated in terms of the quality and thickness of the fabricated films. The results showed that the film continuity and uniformity was improved as a function of both sulfonation percent and polymer concentration. The effect of the solvent system was also

elucidated as the continuity of the SIBS20 film was markedly enhanced when the amount of hexyl alcohol was reduced in the mixture.

Overall, the optimum film quality likely requires a proper balance of the critical parameters because variations in the process variables could also result in more surface defects. The rapid evaporation of solvent and water during the spin-coating process induces “striations” and pin-hole formation in the films.

Finally, the thickness of the films also increased as a function of both the sulfonation percent and the polymer concentration.

CHAPTER 5

CHEMICAL AND MORPHOLOGICAL CHARACTERIZATION OF SIBS THIN FILMS

This chapter contains the main research findings regarding the chemical and morphological characterization of the SIBS thin films. The first section covers the results of chemical characterization, whereas the second one covers the morphological characterization results. The effect of critical variables such as sulfonation percent and polymer concentration, as well as the thermal annealing treatment on the phase separated morphology of the thin films, are also discussed in detail.

5.1. Chemical Characterization

FTIR spectroscopy was used for the chemical characterization of the SIBS thin films to verify the presence of sulfonic functional groups. **Figure 5.1** shows the IR spectrum for an unsulfonated SIBS thin film fabricated at 10 wt% polymer concentration. The sample exhibits IR peaks between 670 cm^{-1} and 3000 cm^{-1} which correspond to C-H, C-C, and C=C atomic bonding vibrations.^{132,133} The characteristic peaks for this triblock copolymer can be observed at 2947 cm^{-1} , 1489 cm^{-1} , 1471 cm^{-1} , 1456 cm^{-1} , 1383 cm^{-1} , 1363 cm^{-1} , 1228 cm^{-1} , 921 cm^{-1} , 760 cm^{-1} , and 670 cm^{-1} .

Table 5.1 presents a list of all of the characteristic peaks and their corresponding vibrational mode descriptions. For example, the peaks observed at 2947 cm^{-1} and 1456 cm^{-1} are generally attributed to the C-H stretching and bending vibrations, respectively.

In turn, the peaks at 1383 cm^{-1} and 1363 cm^{-1} are representative of the methyl (CH_3) swing vibrations, which occur in the PIB blocks. Also, the peaks observed at 1489 cm^{-1} and 760 cm^{-1} correspond to the $\text{C}=\text{C}$ stretching and C-H deformation vibrations, which take place in the aromatic rings of the PS blocks.

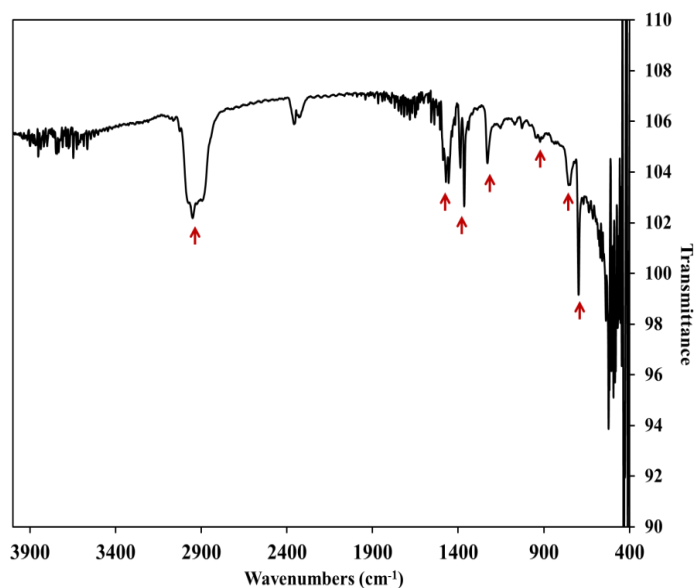


Figure 5.1. FTIR spectrum for an unsulfonated SIBS thin film fabricated at 10 wt% polymer concentration.

Table 5.1. Main IR peaks of unsulfonated SIBS and their corresponding vibrational mode descriptions.

Wavenumber (cm ⁻¹)	Vibration Mode
670	Out-of plane C-H bending vibrations in the aromatic ring
760	Out-of plane C-H bending vibrations in the aromatic ring
921	C-C stretching vibrations
1228	C-H bending vibrations in CH_2
1383	CH_3 swing vibrations
1363	CH_3 swing vibrations
1456	C-H bending vibrations
1489	$\text{C}=\text{C}$ stretching vibrations in the aromatic ring
2947	C-H stretching vibrations

Figure 5.2 presents the infrared spectra for SIBS thin films fabricated at 2.5 wt% polymer concentration with sulfonation percents of: 0, 45, 70, and 80%. The critical differences in the spectra for the sulfonated SIBS thin films can be observed in the region from 1000 cm^{-1} to 1160 cm^{-1} , where four characteristic peaks appear at 1006 cm^{-1} , 1034 cm^{-1} , 1127 cm^{-1} , and 1156 cm^{-1} .

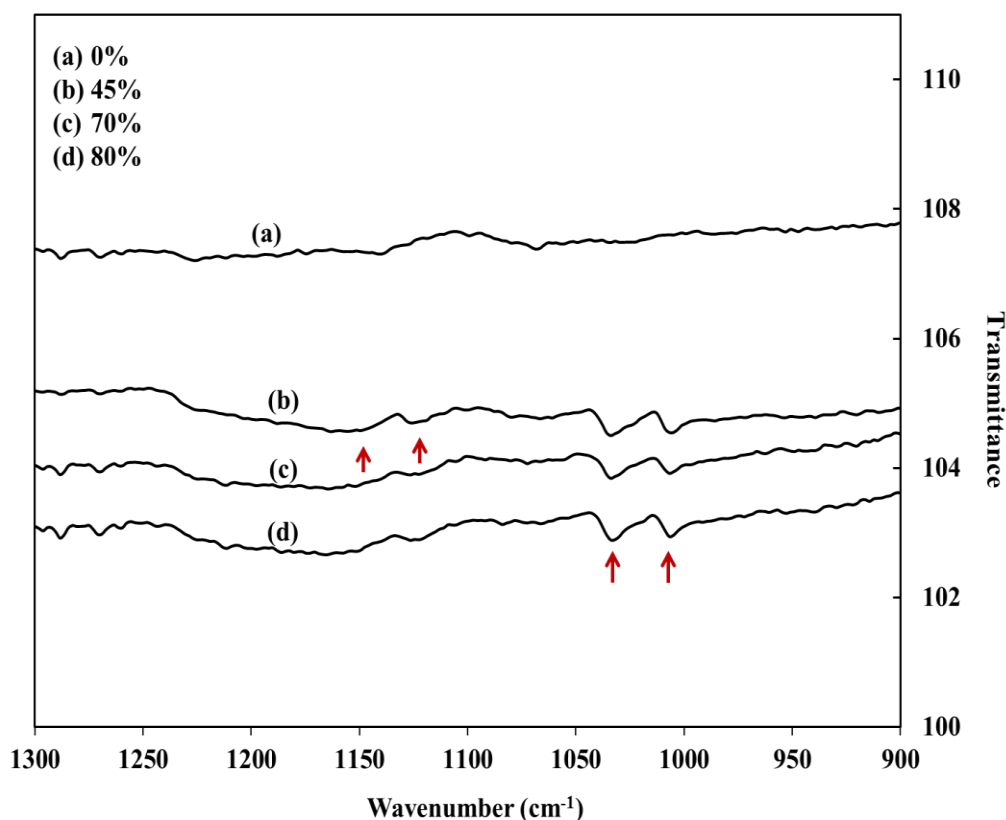


Figure 5.2. FTIR spectra for SIBS thin films fabricated at 2.5 wt% polymer concentration with sulfonation percents of: (a) 0%, (b) 45%, (c) 70%, and (d) 80%.

These peaks can be attributed to the molecular vibrations of the sulfonic groups.¹³⁴ More specifically, the peak observed at 1006 cm^{-1} is representative of the in-plane bending vibrations of the aromatic ring para-substituted with the sulfonic group, whereas the peak

at 1127 cm^{-1} is normally attributed to the sulfonic anion bonded to the aromatic ring. In addition, peaks at 1127 and 1156 cm^{-1} are related to asymmetric and symmetric vibrations of the sulfonic group, respectively.¹³⁵

These characteristic IR peaks are observed for all the sulfonated SIBS thin films regardless of the polymer concentration used to prepare the films. As expected, however, their relative intensity increases as the concentration of polymer increases in the film. The corresponding spectra at 5 wt% polymer concentration and 10 wt% polymer concentration are presented in **Figure 5.3** and **Figure 5.4**, respectively.

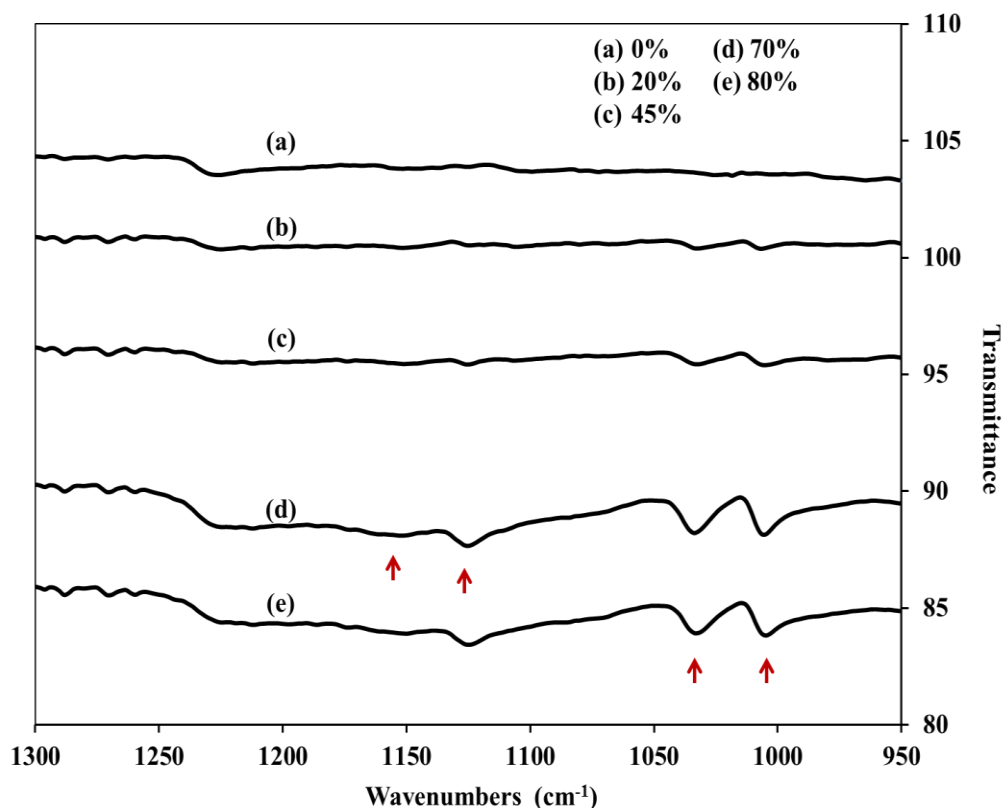


Figure 5.3. FTIR spectra for SIBS thin films fabricated at 5 wt% polymer concentration with sulfonation percent of: (a) 0%, (b) 20%, (c) 45%, (d) 70%, and (e) 80%.

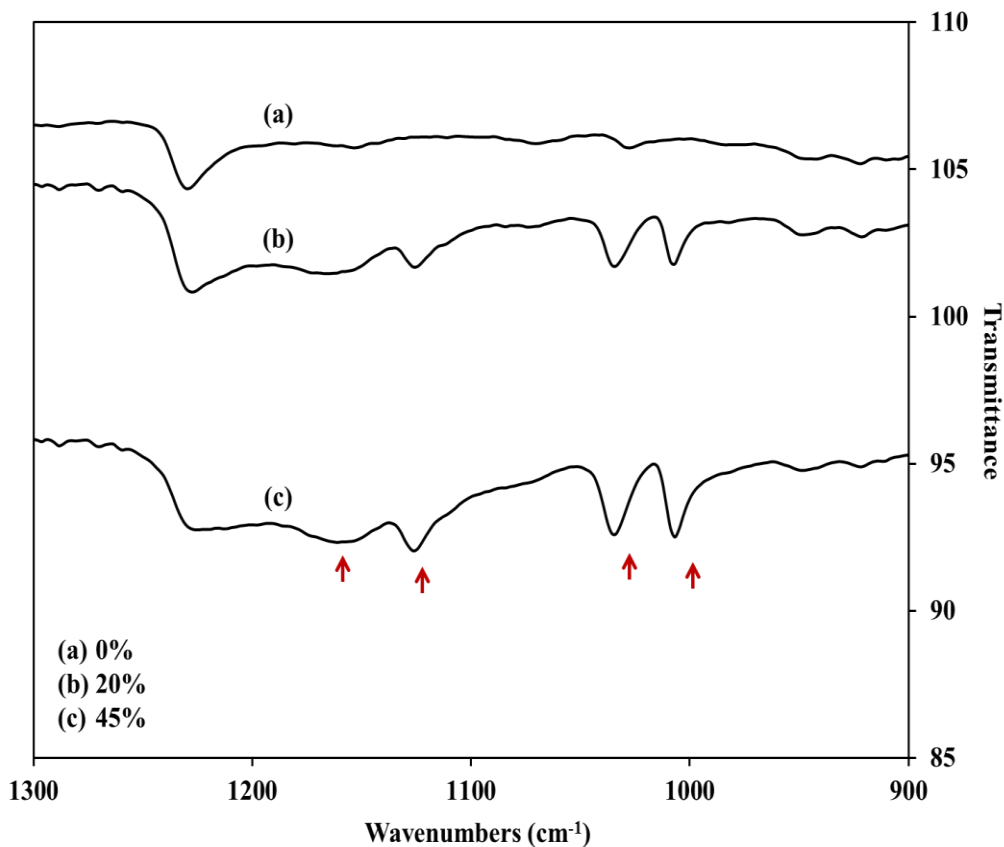


Figure 5.4. FTIR spectra for SIBS thin films fabricated at 10 wt% polymer concentration with sulfonation percent of: (a) 0%, (b) 20%, and (c) 45%.

5.2. Morphological Characterization

The effect of process variables on the morphology of SIBS thin films was evaluated using a combination of materials characterization techniques. Some of the process variables that were investigated included the solvent system, the sulfonation percent, the polymer concentration, and a thermal annealing treatment. AFM was the primary technique used to study the morphology of the films.

5.2.1. Solvent Effects

The solvent effects on film morphology were evaluated using two different solvent systems: pure toluene and an 85:15 (v/v) mixture of toluene and hexyl alcohol. The films were prepared with SIBS00 polymer and compared as a function of the solvent system used.

Figure 5.5 shows the AFM phase images for the two samples. Since the film fabricated with the 85:15 solvent mixture was not continuous across the wafer surface, Figure 5.5a was obtained by scanning a small area of the silicon substrate that was covered with polymer. The results show that both samples exhibit the same type of phase-separated morphology. More specifically, it can be described as a combination of perpendicular polystyrene (PS) cylinders and a few lamellae with average domain size on the order of 29 to 32 nm, embedded in a continuous polyisobutylene (PIB) matrix. Therefore, the specific solvent system used in this study does not appear to have an effect on the morphology of the films.

The specific morphological description presented for the SIBS films is based on supporting evidence from preliminary reports. For example, Puskas *et. al.*¹⁰⁸, studied the effect of PS segment composition on the morphology of spin-coated SIBS00 films. They concluded that for samples with 20 wt% PS content, the film morphology was mostly formed by PS spheres embedded in a PIB continuous matrix. However, at 34 wt% PS content they observed a cylindrical/lamellar morphology, instead.

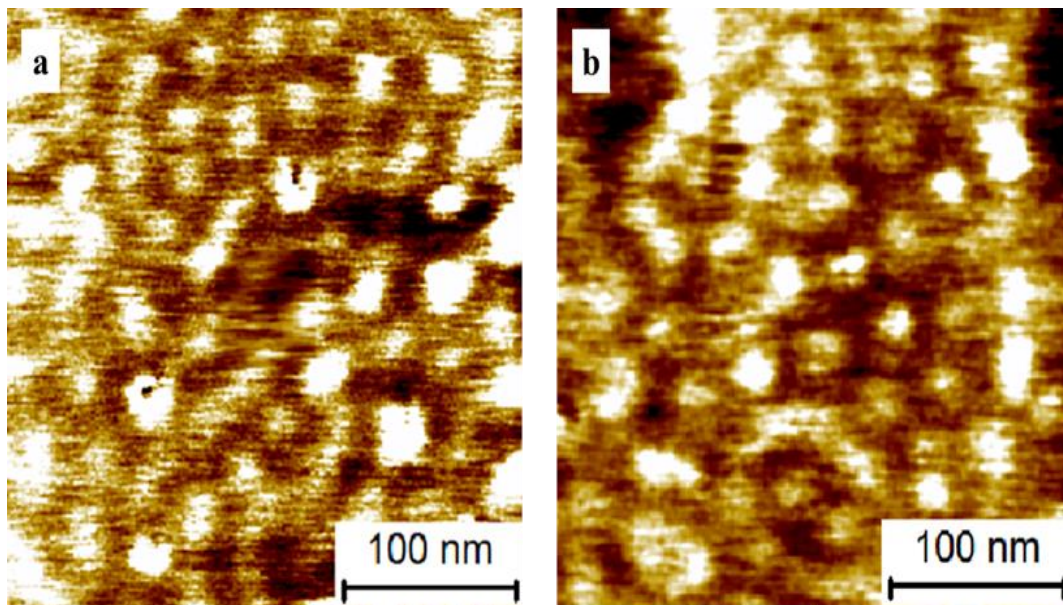


Figure 5.5. AFM phase images for thin films fabricated with SIBS00 polymer and using two different solvent systems: (a) 85:15 (v/v) toluene/hexyl alcohol mixture and (b) pure toluene.

This morphological transition suggests that the fraction of PS controls the phase separated morphology that is formed in the unsulfonated SIBS block copolymers.

These results are also consistent with the findings of Elabd and collaborators¹¹, who studied the morphology of solvent-casted SIBS (~30 wt% PS) films via SAXS. They also found that the morphology for SIBS00 films was cylindrical, or more specifically, composed of hexagonally-packed cylinders (HPC) with short-range order.

Based on these reports, which show that unsulfonated SIBS polymers with 30 wt% PS typically exhibit cylindrical morphologies, and considering that the SIBS00 polymer used in this work also has ~30 wt% PS, the presence of spheres in Figure 5.5 is likely discarded as a morphology that consists of vertically-aligned cylinders is more probable.

5.2.2. Sulfonation Percent and Thermal Annealing Treatment Effects

Figure 5.6 presents the AFM phase images for SIBS films fabricated from polymers with different sulfonation percents and under a variety of thermal annealing conditions. The sulfonation range studied in this case was from 0 to 80% sulfonation and all the films were fabricated at 2.5 wt% polymer concentration. Figures 5.6a through 5.6d correspond to films without a thermal annealing treatment, whereas Figures 5.6e through 5.6h are for the films after thermal annealing at 130°C.

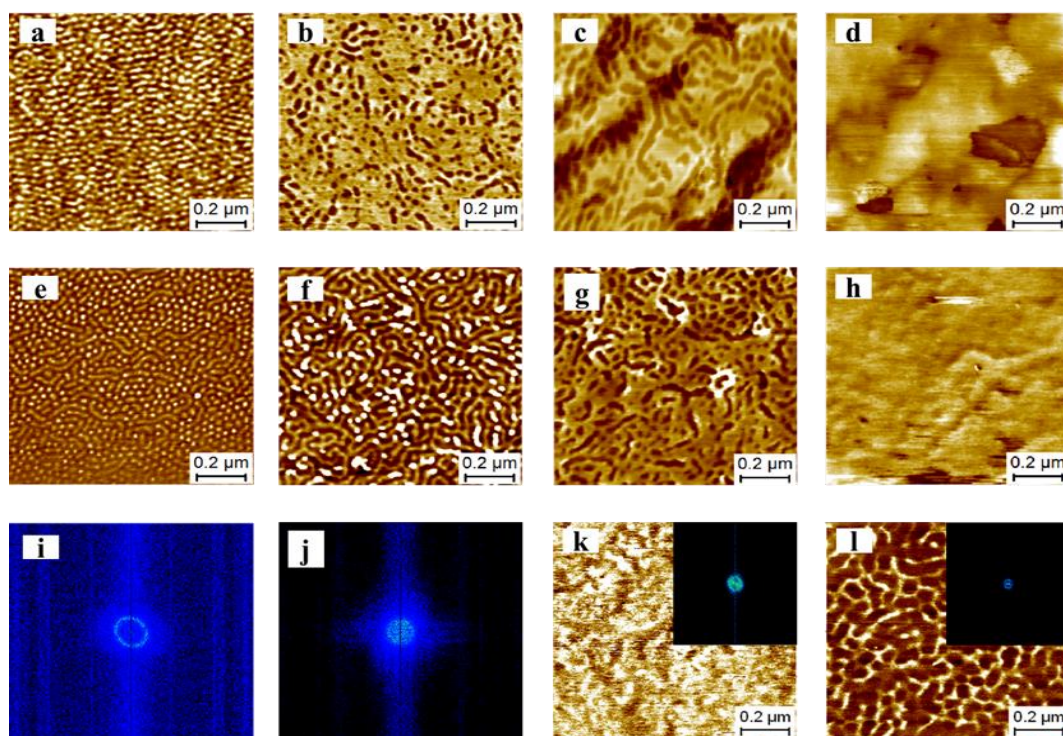


Figure 5.6. AFM phase images for SIBS thin films at different sulfonation percents. Figures 5.5a to 5.5d: Samples without thermal annealing fabricated from SIBS polymers with sulfonation percents of: (a) 0, (b) 20, (c) 45, and (d) 80%. Figures 5.5e to 5.5h: Corresponding AFM phase images for the thermally annealed (130°C) samples. Figures 5.5i and 5.5j: Corresponding FFT images for the annealed (130°C) samples shown in Figures 5.5e and 5.5f. Figures 5.5k and 5.5l: Samples fabricated from SIBS polymers with sulfonation percents of: (k) 45 and 150°C thermal annealing, and (l) 80% and 170°C thermal annealing.

The results for the SIBS00-A films demonstrate that the thermally annealed sample (Fig. 5.6e) has a more ordered phase-separated morphology as compared to the sample without annealing (Fig. 5.6a). In both cases, however, the specific type of morphology can be described, just like before, as a combination of PS cylinders and few lamellae. It is worth mentioning that despite Figure 5.6e shows some HPC on the film surface, most of the perpendicularly-aligned cylinders are randomly distributed across the film. According to Crawford et. al.¹³⁶ and Storey and co-workers¹³⁷, the long-range order in SIBS00 polymers increases with decreasing solvent evaporation rates. Therefore, because the spin-coating process induces much higher evaporation rates as compared to a solvent-casted process (used for others studies), this could explain the short-range ordered morphology observed in the SIBS00-A films.

In comparison, the SIBS20-A film without annealing (Fig. 5.6b) shows large aggregated regions and some interconnected domains, which drastically transform into a more ordered morphology for the annealed film (Fig. 5.6f). The latter can be described as consisting of lamellae (also perpendicular to the substrate) with an average domain size of 38.13 ± 2.31 nm embedded in a PIB matrix. A similar behavior was observed by Elabd and collaborators¹³⁸, who studied the phase separated morphology of solvent-casted SIBS films with different sulfonation percents via small angle X-ray scattering (SAXS). They also reported a short-range ordered lamellar morphology for the SIBS films with sulfonation percents ranging from 17 to 36%.

On the other hand, the thermal annealing treatment at 130°C did not appear to have a significant effect in the films with higher sulfonation percent. This can be observed from the similarities in the AFM phase images for the SIBS45-A and SIBS80-A samples

without a thermal annealing treatment (Fig. 5.6c and 5.6d, respectively) and after annealing (Fig. 5.6g and 5.6h, respectively). Nevertheless, a phase-separated morphology is still observed for the SIBS45-A film, whereas the SIBS80-A does not appear to have segregated morphology. In the case of the SIBS45-A film, the morphology is somewhat similar to the SIBS20-A film without annealing, but with a higher degree of interconnected lamellae. However, unlike the SIBS20-A film, the PS aggregates in the SIBS45-A film do not disappear after the thermal annealing process. The network-like structure observed in the SIBS45-A film has an average domain size of 40.80 ± 6.01 nm. Figures 5.6i and 5.6j correspond to Fast Fourier transform (FFT) images for the SIBS00-A and SIBS20-A annealed films, respectively. The FFT is an image processing tool that can be used to determine the shape, size, and orientation of the phase-separated morphology in block copolymer films. In addition, for a block copolymer film with isotropic morphology, the diameter of the ring (k^* , the wave vector at which the intensity of the FFT ring is a maximum) can be used to determine the characteristic polymer domain size as $1/k^*$.^{139,140,141} Therefore, the FFT images for the thermally annealed samples further corroborate the ordered to disordered morphological transition observed with an increase in the sulfonation percent. That is, the well-defined ring shown for the SIBS00-A film (Fig. 5.6i) tends to disappear as the sulfonation percent and/or the ionic content increases in the film. Furthermore, the results also indicate that the average PS domain size increases with ion inclusion as the diameter of the ring significantly decreases with sulfonation of PS segments.

The specific morphological reordering observed for the thermally annealed SIBS00-A and SIBS20-A films (as compared to the films without annealing) can potentially be explained

by comparing the glass transition temperature (T_g) of the polymer with the annealing temperature (T_a) used for the process. The idea is that when $T_a > T_g$, the polymer chains become mobile and the entire structure could get rearranged towards an equilibrium state.^{142,143,144} In order to support this hypothesis, the T_g for all of the SIBS polymers was evaluated using DSC analysis.

Figure 5.7 shows the DSC curves for the different SIBS polymers studied, but only in the region where the T_g for the PS segments is observed. The reason for this is that previous studies have shown that the sulfonic groups are chemically attached to the PS segments and therefore, the T_g for the PIB segments remains constant.¹³³

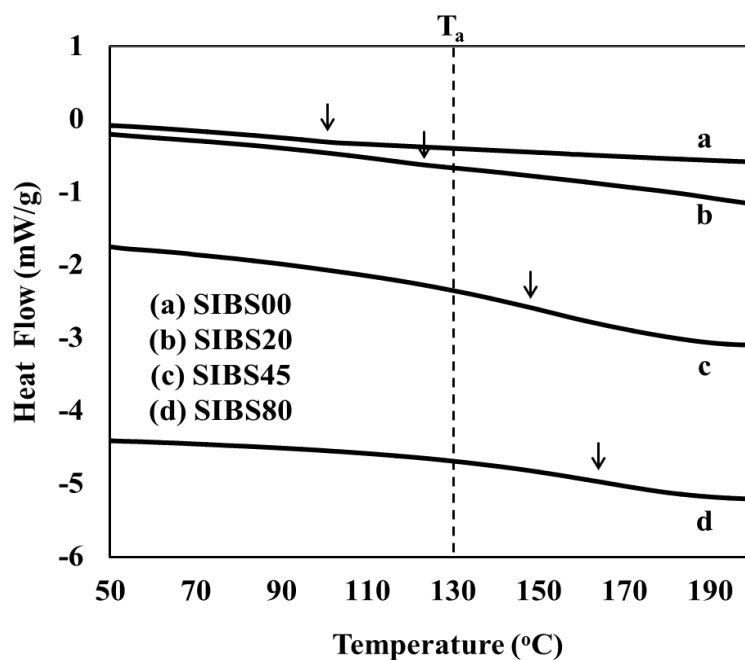


Figure 5.7. DSC curves for SIBS polymers with sulfonation percents of: (a) 0%, (b) 20%, (c) 45%, and (d) 80%. Data presented is for the second re-heating step in the cycle.

The DSC results show that the T_g for the PS segment (as indicated by the vertical arrows) increases as a function of the sulfonation percent. More specifically, for the SIBS00 and SIBS20 polymers, these are exhibited at 98°C and 120°C, respectively. Because the T_g for these two polymers is lower than the T_a used for the process (130°C), this could therefore explain the change in morphology after thermally annealing the films. As the T_g for the SIBS45 and SIBS80 polymers were recorded at 145°C and 162°C, respectively, this also explains that no changes in morphology were detected in such cases upon thermally annealing the films at 130°C.

In order to further assess the morphology of the SIBS45-A and SIBS83-A films under equilibrium conditions (*i.e.* above the T_g), these films were annealed at 150°C and 170°C, respectively. The annealing time used was the same as for the other samples (98 hours). The results are presented in the last two images of Figure 5.6. Figure 5.6k corresponds to the AFM phase image for the newly annealed SIBS45-A film, whereas Figure 5.6l shows the phase image for SIBS80-A film. The differences observed in Figures 5.6g and 5.6k for the films fabricated with SIBS45, as well as in Figures 5.6h and 5.6l for the films fabricated with SIBS80, suggest that the thermal annealing treatment above the T_g had an effect on the phase separated morphology of these films. For example, the network-like structure observed in the SIBS45-A film after thermal annealing at 130°C (Fig. 5.6g) was not observed in the SIBS45-A film at equilibrium (Fig. 5.6k). Also, the image for the SIBS80-A film annealed at 130°C (Figure 5.6h) does not appear to have segregated morphology; however, the image for the SIBS80-A film at equilibrium (Fig. 5.6l) clearly shows a phase separated morphology consisting of a network of PS domains embedded in a

continuous PIB matrix. The average PS domain size for this film was measured at 48.72 ± 7.63 nm.

An important observation for the films annealed at temperatures above the T_g is that there is a morphological transition as the sulfonation percent increases from 0 to 80%. The images show a clear transition from a short-range ordered cylindrical/lamellar morphology to a more disordered morphology (network-like structure) as the sulfonation percent increases. Also, the PS domain size increases from 29 nm to 49 nm as the sulfonation percent increases from 0% to 80% as shown in **Table 5.2**. These morphological transitions are likely because the incorporation of ionic groups into the polymer matrix causes an increase in segregation, much like increasing the PS content in the block copolymer does.¹⁸

Table 5.2 PS domain size as a function of the sulfonation percent in the SIBS thin films.

Sulfonation %	PS domain size (nm)
0	30.50 ± 1.50
20	38.13 ± 2.31
80	48.72 ± 7.63

XRD experiments were also performed in order to evaluate structural changes (at the atomic level) in the SIBS thin films as a function of sulfonation percent. **Figure 5.8** shows

the X-ray diffraction patterns for three SIBS thin film with different sulfonation percents as well as the blank silicon wafer that was used as the substrate for depositing the films (background for the study). All the films were fabricated at 10 wt% polymer concentration.

Figure 5.8a shows the XRD diffraction pattern for the silicon substrate. As expected, the peak at $2\theta = 71^\circ$ reflects the single crystal nature of this type of substrate. An important thing to note, however, is that there is no overlap between the characteristic peak for the substrate and the interest region for the polymers. The latter appears to be in the range of 2θ from 8° to 28° .

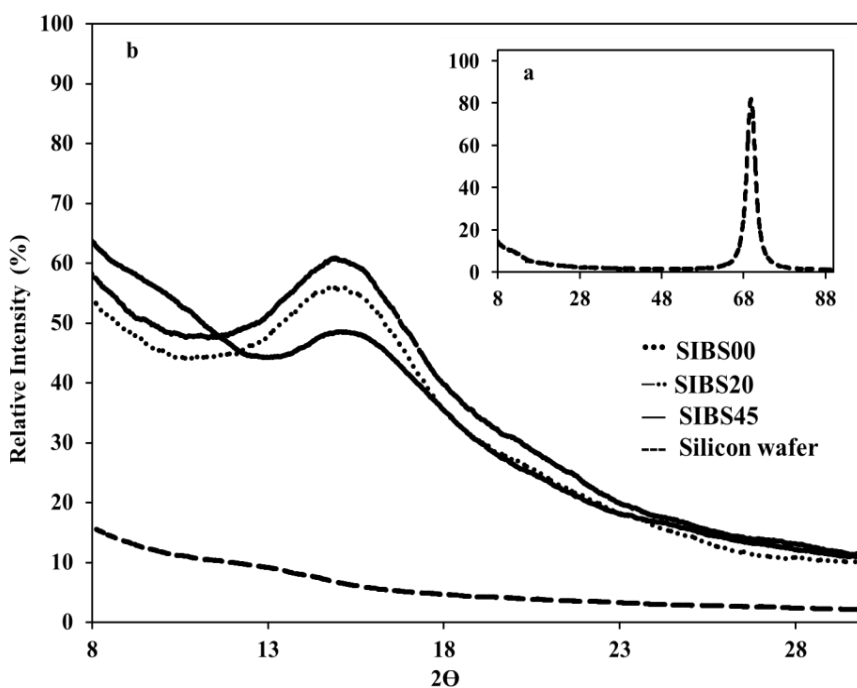


Figure 5.8. X-ray diffraction patterns for: (a) blank silicon wafer substrate and (b) SIBS thin films with different sulfonation percent.

Although all the SIBS samples exhibited a broad peak characteristic of amorphous polymers (Fig. 5.8b), the thin film with the highest sulfonation percent (SIBS45-C) showed a peak shift towards a higher angle ($2\theta = 15^\circ$) as compared to the SIBS00-C film, which showed the peak at $2\theta = 14^\circ$. A possible explanation for this observation could be that the distance between ionic clusters decreases with sulfonation percent. In addition, these profiles also indicate that the peak definition decreases with sulfonation percent, which could be explained if the inclusion of the sulfonic groups into the polymer matrix produced a more disordered atomic structure.¹⁴⁵

5.2.3. Polymer Concentration Effects

Because previous reports suggest that the phase-separated morphology of block copolymers can be controlled by solution concentration,¹⁴⁶ the effects of polymer concentration on film morphology were also investigated. **Figure 5.9** shows the AFM phase images for films fabricated from SIBS00 and SIBS20 using two different polymer concentrations: 2.5 wt% (Figs. 5.9a and 5.9c, respectively) and 10 wt% (Figs. 5.9b and 5.9d, respectively).

The results suggest that the morphology does not change for either type of polymer as the concentration in the film is increased, but rather that the size of the PS domains does change in the range from 2.5 to 10 wt% polymer concentration. In the case of the films fabricated with SIBS00 polymer, the domain size increases from 26.31 (± 3.05) nm to 34.42 (± 6.19) nm and for the films prepared from SIBS20, the domains increase from 43.09 (± 5.98) nm to 68.05 (± 17.19) nm. These results are also consistent with the FFT

images inserted in Figures 5.9c and 5.9d for the SIBS20 films, which show that the diameter of the ring decreases with an increase in the polymer concentration.

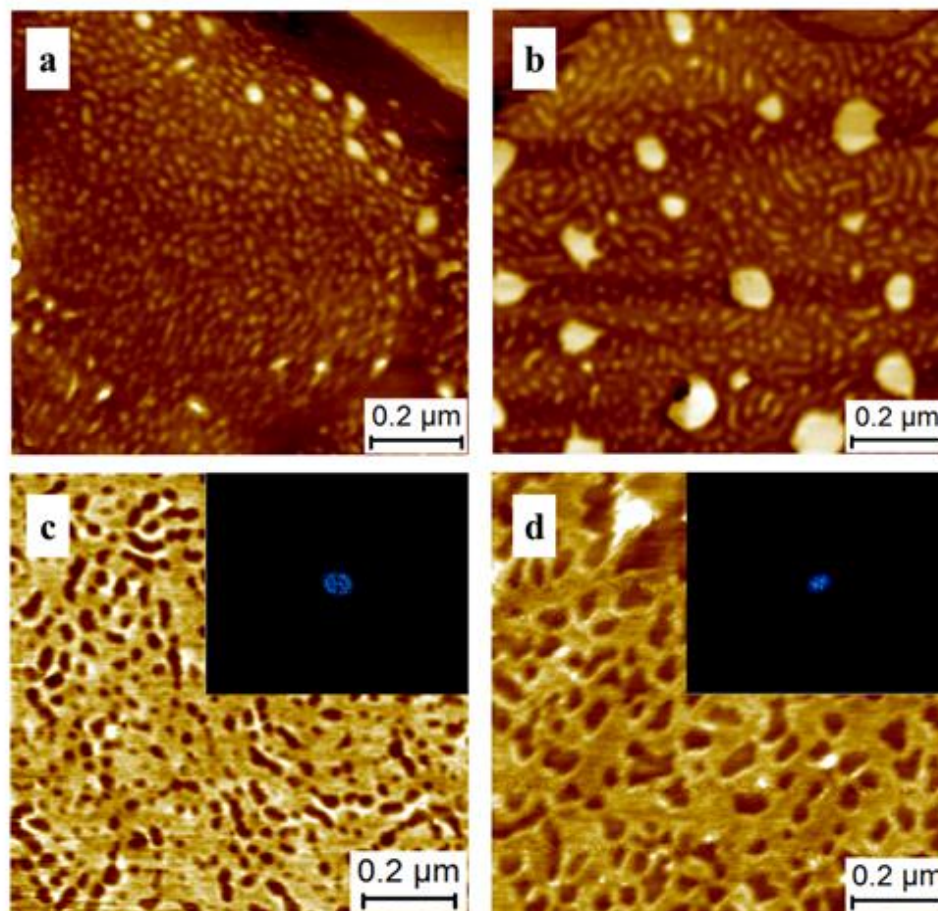


Figure 5.9. AFM phase images for films fabricated from SIBS00 and SIBS20 at: 2.5 wt% polymer concentration (Fig. 5.8a and 5.8c, respectively) and at 10 wt% polymer concentration (Fig. 5.8b and 5.8d, respectively).

A potential explanation for this observation could be that at low polymer concentrations, the polymer chains are more dispersed and under the rapid solvent evaporation of the spin-coating process, they do not have enough time to form into large domains.

In contrast, high polymer concentrations promote the formation of larger domains because the polymer chains in solution are closer together and/or could even be arranged into

micelles. Similar observations were reported by Fang *et al.*¹⁴⁷ when they studied the effect of the polymer concentration on the phase-separated morphology for PS-poly(acrylic acid) blends.

5.3 Summary

The effect of critical variables such as polymer concentration and sulfonation percent on the resulting morphology of the SIBS thin films was evaluated as well as the effect of a thermal annealing treatment.

AFM studies revealed phase-separated morphologies with critical transitions from a short-range ordered cylindrical/lamellar morphology to a more disordered morphology (network-like structure) as the sulfonation percent increased from 0 to 80%. In addition, the results showed that the PS domain size increases with both sulfonation percent and polymer concentration. The thermal treatment used in the fabrication of the films also had a significant effect in re-ordering the morphology, but only in the cases where the annealing temperature was above the T_g of the polymer.

CHAPTER 6

MECHANICAL CHARACTERIZATION OF SIBS THIN FILMS

This chapter presents the results of the mechanical characterization of SIBS and Nafion[®] thin films via nanoindentation. The first section presents the substrate-independent mechanical properties of the thin films and the second part covers the effect of variables such as sulfonation percent, polymer concentration, temperature, and hydration treatment on the mechanical properties of the films.

6.1. Substrate-Independent Mechanical Properties

Instrumented nanoindentation was used to evaluate the mechanical properties of SIBS thin films. **Figure 6.1** shows the typical load versus displacement data obtained for an indentation array. The specific data presented is for twenty indents performed on a SIBS45-C sample. It is important to note that the normalized displacement into surface is calculated using the following equation:

$$\text{Normalized Displacement into Surface} = \frac{\text{Penetration depth}}{\text{Film thickness}} * 100\% \quad (6.1)$$

For example, a normalized displacement of 30% in a 100 nm-thick film indicates that the penetration depth of the tip into the film was 30% of the total film thickness or 30 nm.

All of the curves in Figure 6.1 show the same behavior. That is, the normalized displacement into the surface increases continuously as the applied load increases. At the maximum load (~0.5 mN), the tip reaches a normalized displacement into the surface of approximately 55%. Then, the tip continues to penetrate into the surface at a constant

load, during the step known as the “holding segment”. Subsequently, the polymer film exhibits a certain degree of recovery (elastic behavior) as the tip is withdrawn from the sample. Finally, the step observed after the unloading segment corresponds to the thermal drift measurement.

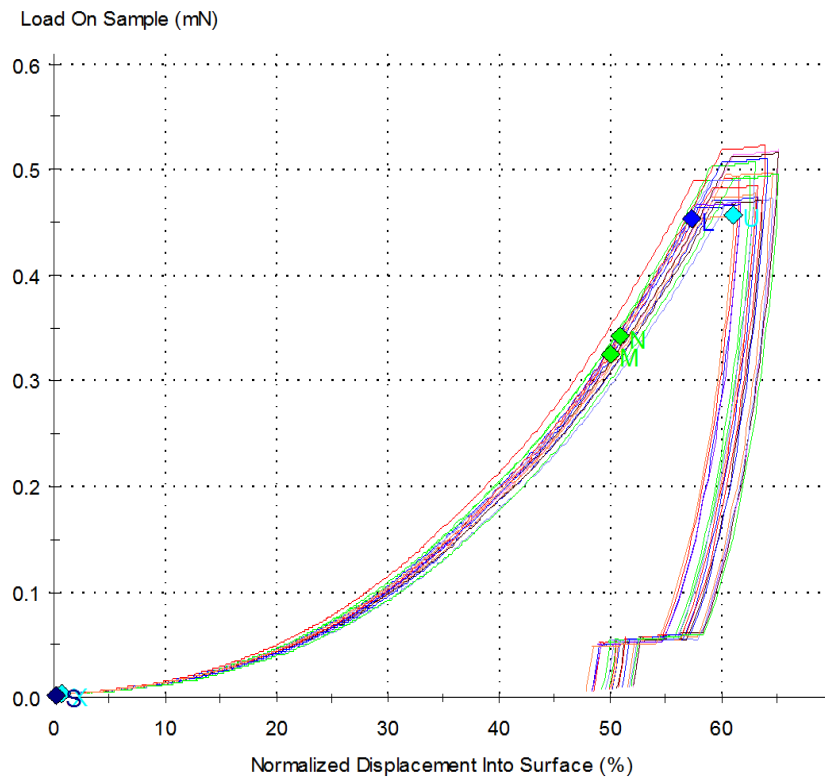


Figure 6.1. Load versus displacement data obtained for an indentation array in SIBS45-C.

Figure 6.2 corresponds to a typical indentation array as observed by optical microscopy. The distance between adjacent indentations was set at 25 μm in order to avoid potential interference.

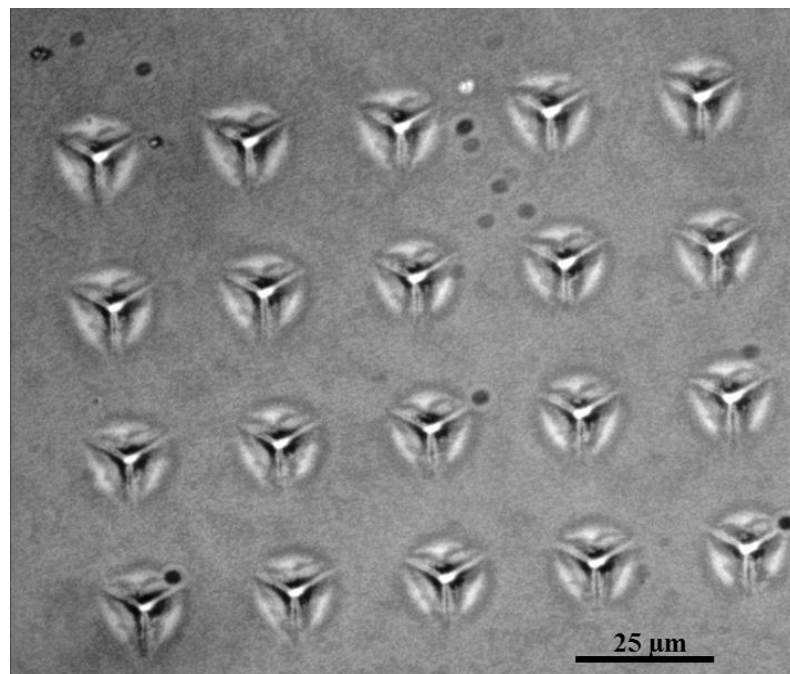


Figure 6.2. Optical microscopy image for a 5x4 indentation array on sample SIBS45-C

For all the SIBS thin films, both the apparent elastic modulus and the substrate-independent elastic modulus, were calculated using the G-Series CSM thin film method as described in section 3.2.7.

Figure 6.3 displays both the apparent (E_a) and substrate-independent elastic modulus (E_f) as a function of normalized displacement for different SIBS thin films. Figures 6.3a to 6.3c correspond to films with sulfonation percent of 0% and fabricated at 2.5 wt%, 5 wt%, and 10 wt% polymer concentration, respectively. Similarly, Figures 6.3d through 6.3f correspond to films with a sulfonation percent of 45% and fabricated at 2.5 wt%, 5 wt% and 10 wt% polymer concentration, respectively.

The continuous lines refer to the apparent elastic modulus, while the dotted lines represent the substrate-independent elastic modulus measurements. In general, the apparent elastic modulus shows the same behavior for all the samples. The curve rapidly decreases with the normalized displacement and then progressively increases, which is an indication that the influence of the substrate is strongly dependent on the penetration depth.

At the beginning of the indentation process, near the surface, the elastic modulus is overestimated due to artifacts related to the surface detection and/or the film roughness. As the penetration into the surface increases, the elastic modulus of the SIBS thin films is also overestimated due to the significant contribution of the substrate (silicon wafer), since it has a much higher elastic modulus ($E = 178$ GPa) as compared to the SIBS thin films.

In contrast, the substrate-independent elastic moduli for the films remain relatively constant even at high normalized displacements. This suggests that the substrate effects were indeed eliminated from the calculated value for the films.

Similarly, **Figure 6.4** shows both the apparent (E_a) and substrate-independent elastic modulus (E_f) as a function of normalized displacement for SIBS thin films with sulfonation percents of 20% and 70%. Figures 6.4a and 6.3b correspond to films with sulfonation percent of 20% and fabricated at 5 wt%, and 10 wt% polymer concentration, respectively.

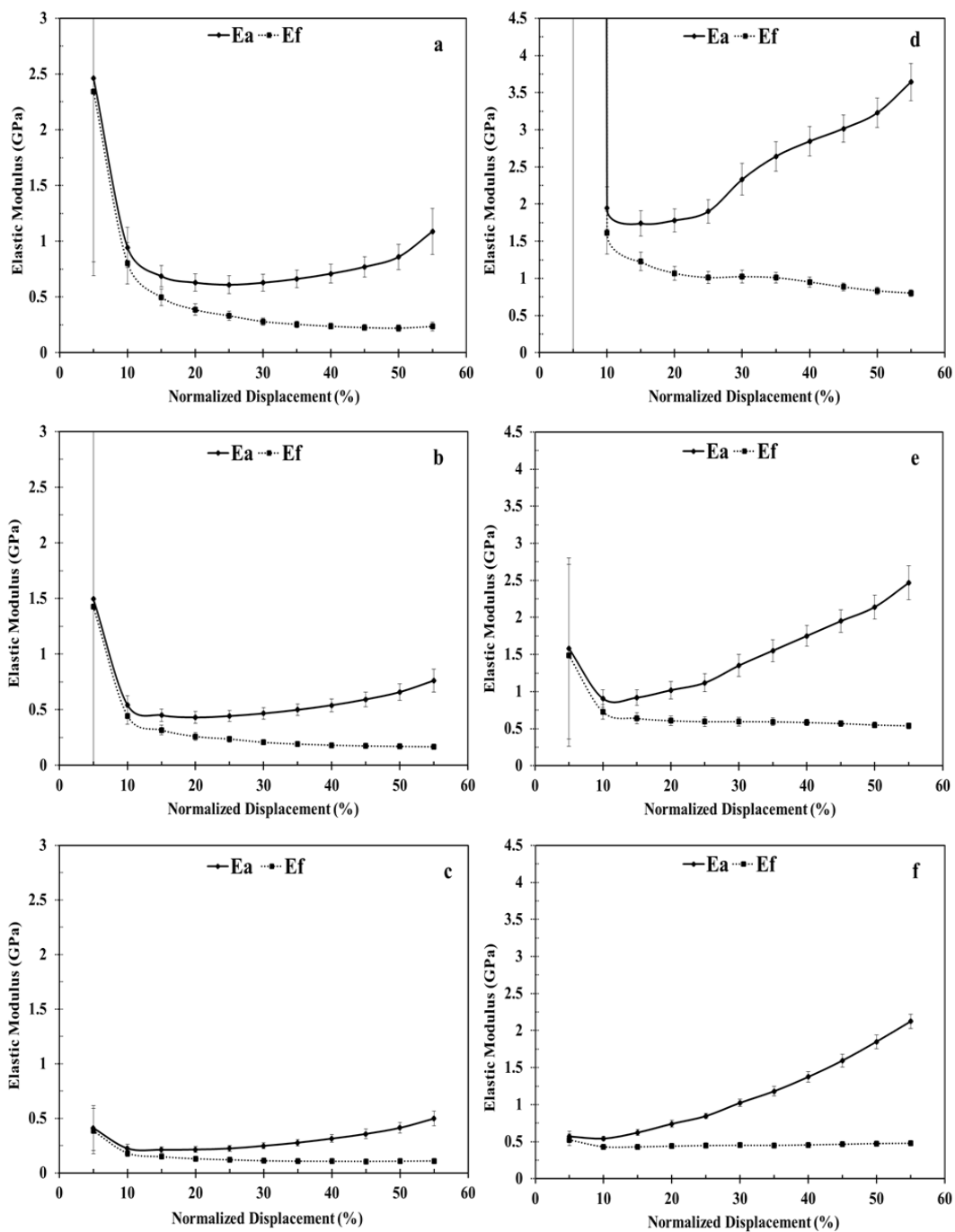


Figure 6.3. Apparent and substrate-independent elastic modulus as a function of normalized displacement for different SIBS films. Figures 6.3a – 6.3c: Corresponding results for films with sulfonation percent of 0% and fabricated at 2.5 wt%, 5 wt%, and 10 wt% polymer concentration, respectively. Figures 6.3d – 6.3f: Corresponding results for films with sulfonation percent of 45% and fabricated at 2.5 wt%, 5 wt%, and 10 wt% polymer concentration, respectively.

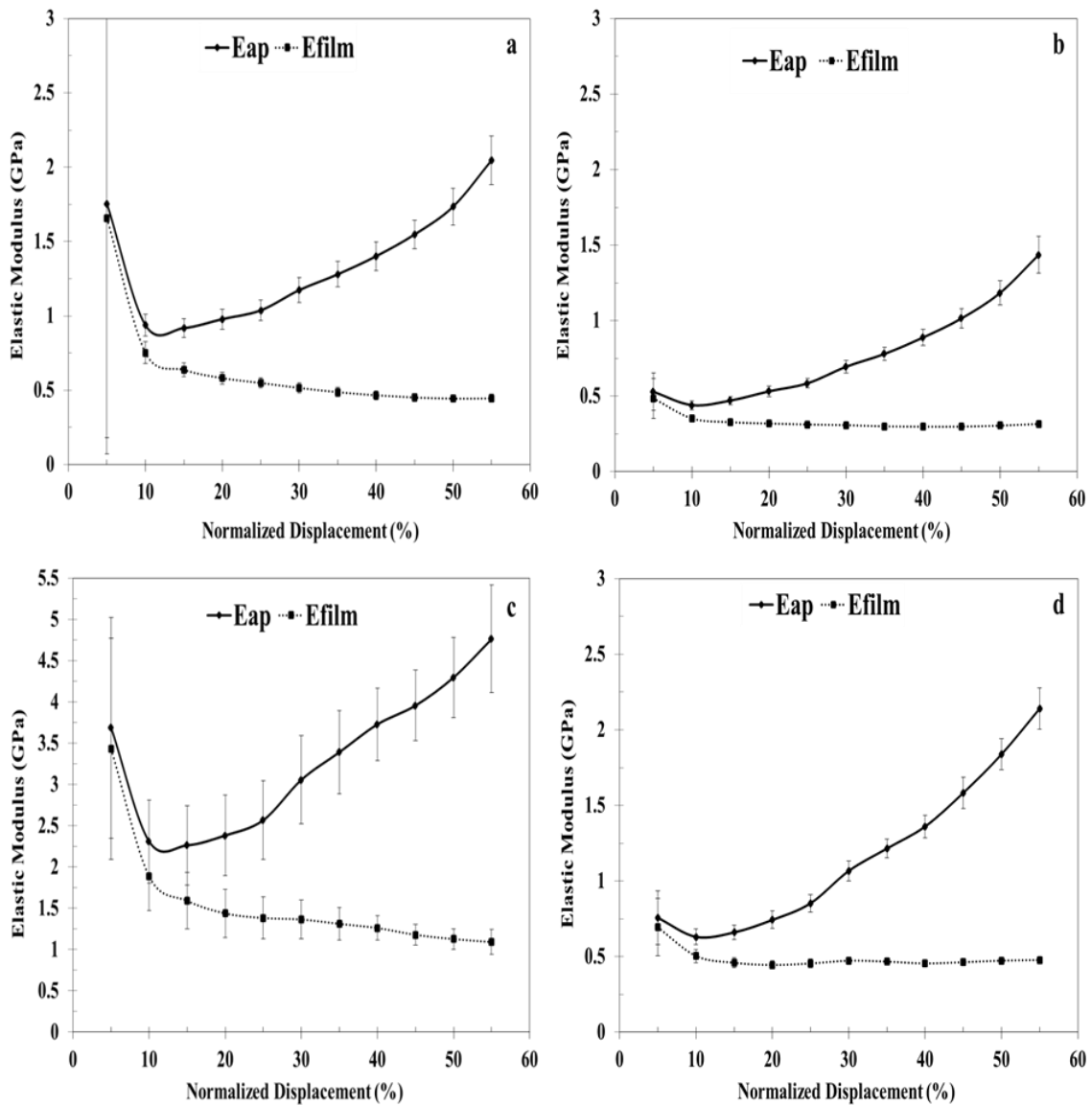


Figure 6.4. Apparent and substrate-independent elastic modulus as a function of normalized displacement for different SIBS films. Figures 6.4a and 6.4b: Corresponding results for films with sulfonation percent of 20% and fabricated at 5 wt% and 10 wt% polymer concentration, respectively. Figures 6.4c and 6.4d: Corresponding results for films with sulfonation percent of 70% and fabricated at 2.5 wt% and 5 wt% polymer concentration, respectively.

Similarly, Figures 6.4c and 6.4d correspond to films with a sulfonation percent of 70% and fabricated at 2.5 wt% and 5 wt% polymer concentration, respectively. It can be observed that all of the curves in Figure 6.4 exhibit a similar behavior similar to the one previously described for the Figure 6.3.

On the other hand, **Figure 6.5** and **Figure 6.6** show 3D elastic moduli maps for different SIBS thin films fabricated at 5 wt% polymer concentration and sulfonation percents of: 0% (Fig. 6.5a), 20% (Fig. 6.5b), 45% (Fig.6.5c), 70% (Fig.6.6a), and 80% (Fig.6.6b). The images were obtained using MATLAB[®] 7.6 software and correspond to variations in the elastic modulus across the area covered by an indentation array. Significant differences are observed for most of the samples across the mapped areas. For example, the SIBS45-B (Fig. 6.5a) and SIBS 70-B samples (Fig. 6.6a) exhibit an elastic modulus variation ranging from 0.46 GPa to 0.62 GPa, and from 0.40 GPa and 0.51 GPa, respectively. A possible explanation for this variation could be related to the fact that SIBS thin films exhibited short-range order phase separated morphology. In others words, the heterogeneous nature of the film morphology probably caused the observed variations in mechanical properties.

Table 6.1 summarizes the substrate-independent elastic modulus values for the different SIBS samples studied. The results were averaged over 240 indentations performed on each sample. The data reveals an overall elastic modulus variation in the range of 0.11 GPa to 1.13 GPa, which is an indication that the studied variables had a significant effect on the mechanical properties of the films. More specifically, sample SIBS80-A exhibited an elastic modulus of 1.14 GPa, which is comparable to the measured value for the

Nafion[®] film (1.21 GPa). Overall, the results show standard deviations ranging from 0.05 to 0.08 GPa.

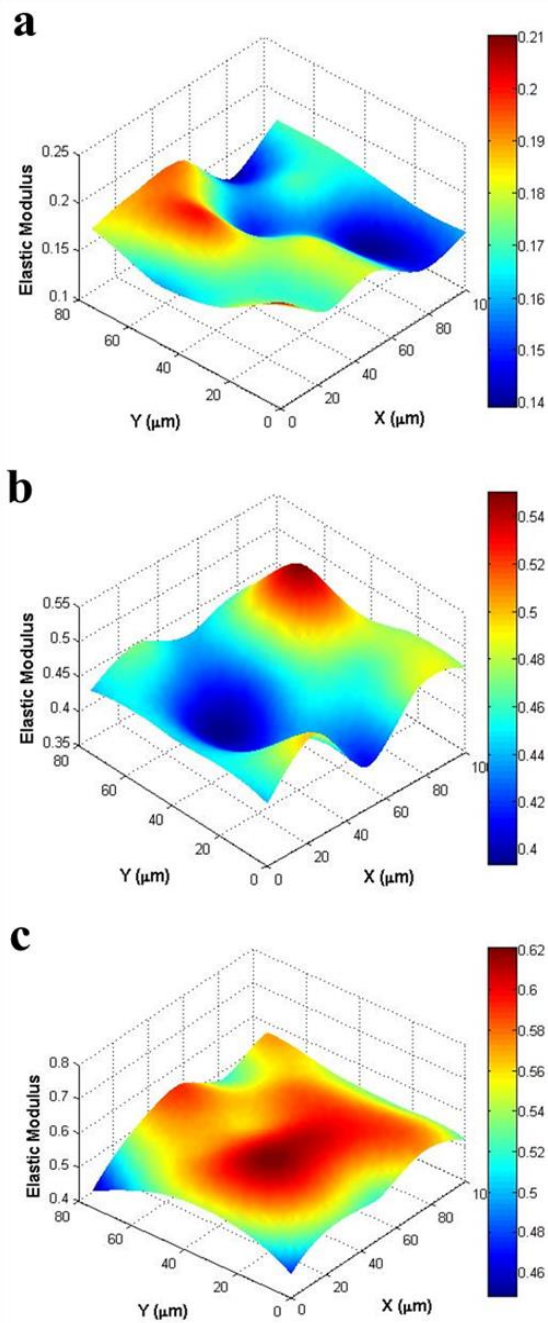


Figure 6.5. Elastic moduli maps for SIBS thin films fabricated at 5 wt% and with different sulfonation percent: (a) 0%, (b) 20%, and (c) 45%.

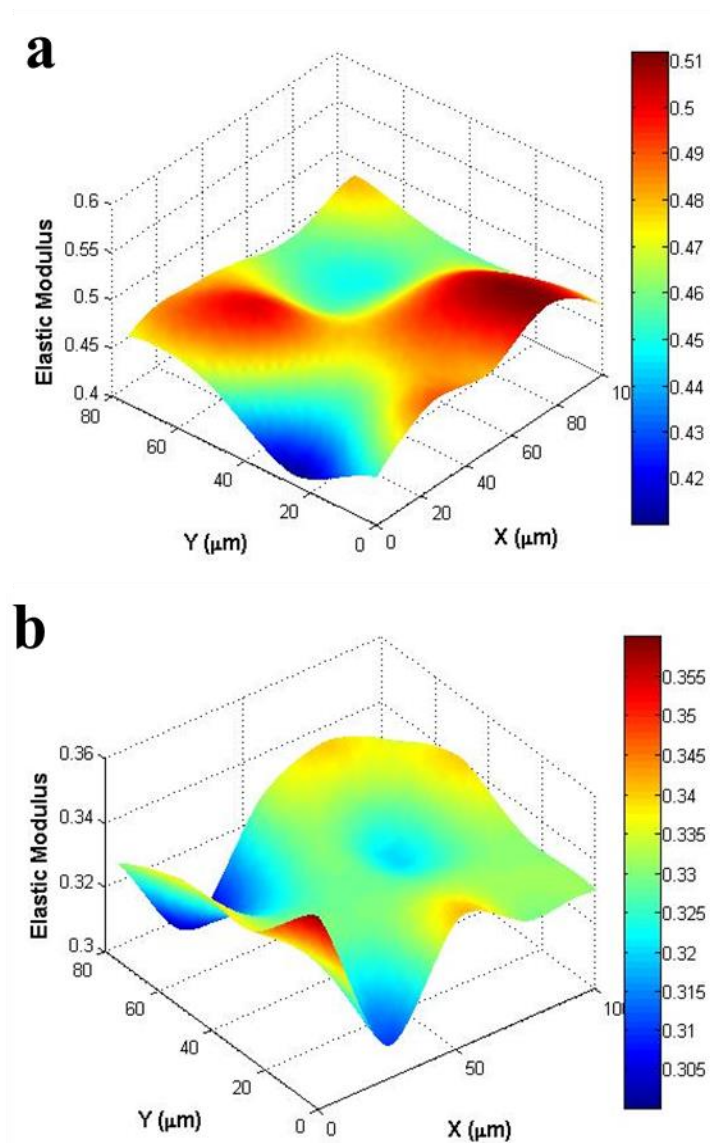


Figure 6.6. Elastic moduli maps for SIBS thin films fabricated at 5 wt% and with different sulfonation percent: (a) 70% and (b) 80%.

Also, the average elastic modulus obtained for all the SIBS samples corresponds to an average measurement between the elastic modulus of the PIB and PS polymer blocks. PIB is an elastomer and therefore has a low elastic modulus. Typically, the elastomers have elastic moduli ranging between 7.0×10^{-4} and 4.0×10^{-3} GPa¹⁴⁸. In contrast, the PS block

imparts mechanical strength to SIBS since this polymer has a higher elastic modulus (~2 GPa).¹⁴⁹

Table 6.1. Average results for the measured substrate-independent elastic modulus and hardness of the SIBS thin films.

Sample	Elastic Modulus (GPa)	Hardness (GPa)
SIBS00-A	0.220 ± 0.018	0.012 ± 0.0
SIBS45-A	0.825 ± 0.055	0.052 ± 0.0
SIBS70-A	1.127 ± 0.076	0.079 ± 0.0
SIBS80-A	1.143 ± 0.060	0.073 ± 0.0
SIBS00-B	0.173 ± 0.005	0.010 ± 0.0
SIBS20-B	0.449 ± 0.013	0.020 ± 0.0
SIBS45-B	0.548 ± 0.030	0.030 ± 0.0
SIBS70-B	0.479 ± 0.027	0.030 ± 0.0
SIBS80-B	0.329 ± 0.026	0.020 ± 0.0
SIBS00-C	0.113 ± 0.009	0.010 ± 0.0
SIBS20-C	0.313 ± 0.024	0.020 ± 0.0
SIBS45-C	0.483 ± 0.023	0.020 ± 0.0
Nafion®	1.207 ± 0.068	0.090 ± 0.0

In order to explain these results, it is also important to consider the contact area between the tip and the SIBS samples during the nanoindentation experiments. To illustrate this, the contact area for the sample SIBS00-A (thinner film) was calculated at three different normalized displacements into the surface: 10%, 30%, and 50%. For a Berkovich tip, the contact area depends on the tip penetration h , and this can be calculated using equations 3.1 and 3.2. At 10% normalized displacement, the contact area is on the order of $9 \times 10^4 \text{ nm}^2$, which is equivalent to one tenth of the AFM phase image presented for SIBS00-A (Figure 5.6e) since it covers approximately $1 \times 10^6 \text{ nm}^2$ of the total film surface. At 30%

and 50% normalized displacements, the projected contact area is on the order of $1.13 \times 10^6 \text{ nm}^2$ and $3.37 \times 10^6 \text{ nm}^2$, respectively. These values are equivalent to one and three times the image shown in the Figure 5.6e, respectively.

Since the SIBS00-A sample exhibited a PS domain size on the order of 29 nm and considering that the calculated contact areas are on the order of micrometers, it is possible to conclude that the indenter interacts with both PS and PIB polymer blocks during a regular indentation step. Therefore, this is likely the reason why the average elastic modulus obtained for the SIBS00-A sample corresponds to a value between the elastic modulus of the PIB and PS polymers blocks. Moreover, the average elastic modulus obtained for this sample was higher as compared to the elastic modulus for the PIB blocks (70 wt% in SIBS), likely as a result that the PS blocks offer mechanical strength to the continuous PIB phase.

Another approach could be to consider the additive laws to calculate a theoretical value for the elastic modulus of SIBS as follows:

$$E_{\text{SIBS}} = E_{\text{PS}} \cdot \phi_{\text{PS}} + E_{\text{PIB}} \cdot (1 - \phi_{\text{PS}}) \quad (6.2)$$

where E_{SIBS} , corresponds to the elastic modulus of SIBS, whereas E_{PS} and E_{PIB} correspond to the elastic modulus of the PS and PIB segments, respectively. ϕ_{PS} represents the weight fraction of PS. Since $E_{\text{PS}} \gg E_{\text{PIB}}$, equation 6.2 can be rewritten as:

$$E_{\text{SIBS}} = E_{\text{PS}} * \phi_{\text{PS}} \quad (6.3)$$

Now, if PS has an elastic modulus of approximately 2 GPa and the PS weight fraction in SIBS is 0.3, the theoretical E_{SIBS} value is 0.6 GPa. Therefore, the predicted value for the elastic modulus of SIBS thin films on the order of 10^{-1} GPa corresponds well with the experimental values measured (shown in Table 6.1).

The hardness was also calculated for the different samples studied. **Figures 6.7** shows the hardness results as a function of normalized displacement for the different SIBS thin films. Figures 6.7a through 6.7c correspond to films with sulfonation percent of 0% and fabricated at 2.5 wt%, 5 wt%, and 10 wt% polymer concentration, respectively. Similarly, Figures 6.7d through 6.7f correspond to films with sulfonation percent of 45% and fabricated at 2.5 wt%, 5 wt% and 10 wt% polymer concentration, respectively.

All the curves shown in Figure 6.7 exhibit the same behavior. Near the surface, the hardness is overestimated due to issues related to the surface detection (as shown in Figures 6.3 and 6.4 for the elastic modulus). Then, the value for the mechanical property remains relatively constant. As expected, these results suggest that the hardness for the SIBS thin films is unaffected by the substrate, even at high penetration depths. As mentioned before, hardness measurements are less sensitive to the substrate influence due to the fact that the extent of the plastic field is much smaller as compared to the extension of the elastic field.⁹⁸

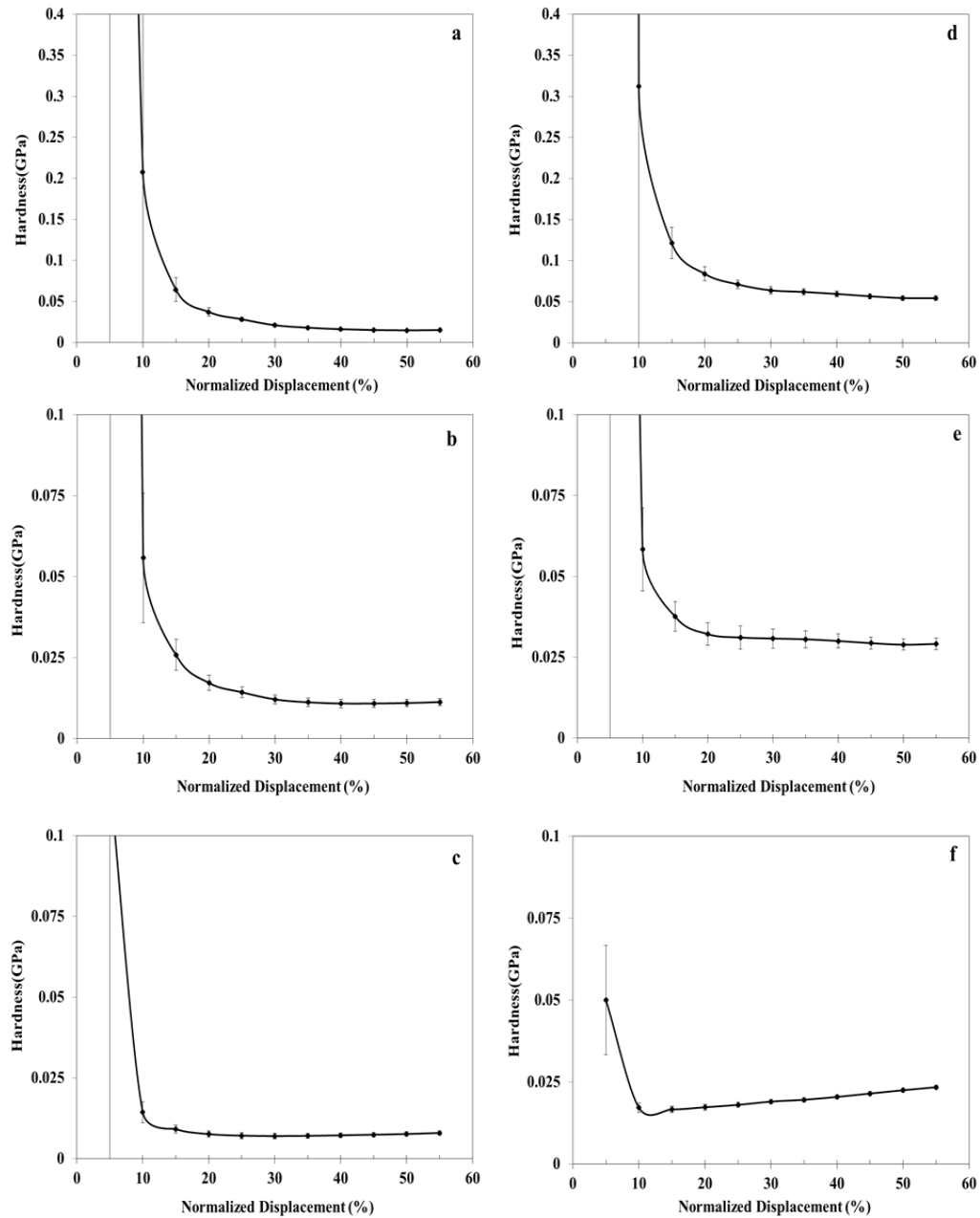


Figure 6.7. Hardness as a function of normalized displacement for different SIBS films. Figures 6.7a – 6.7c: Corresponding results for films with sulfonation percent of 0% and fabricated at 2.5 wt%, 5 wt% and 10 wt% polymer concentration, respectively. Figures 6.7d – 6.7f: Corresponding results for films with sulfonation percent of 45% and fabricated at 2.5 wt%, 5 wt% and 10 wt% polymer concentration, respectively.

Figure 6.8 shows the hardness results for SIBS thin films with sulfonation percents of 20% and 70%. Figures 6.8a and 6.8b correspond to films with sulfonation percent of 20% and fabricated at 5 wt% and 10 wt% polymer concentration, respectively, whereas Figures 6.8c and 6.8d correspond to films with sulfonation percent of 70% and fabricated at 2.5 wt% and 5 wt% polymer concentration, respectively. It can be observed that all of the curves in Figure 6.8 exhibit a similar behavior similar to the one previously described for Figure 6.7.

The averaged hardness results for all the samples are also summarized in Table 6.1. The results show an overall hardness variation in the range of 0.01 to 0.08 GPa, which is an indication that the studied variables had an effect on the mechanical properties of the SIBS thin films.

On the other hand, since $H_{PS} \gg H_{PIB}$, it is also possible to obtain a theoretical hardness value for SIBS using the additive law as follows:

$$H_{SIBS} = H_{PS} * \phi_{PS} \quad (6.4)$$

Now, if PS has a hardness value of approximately 0.172 GPa¹⁴⁸ and the PS weight fraction in SIBS is 0.3, the theoretical H_{SIBS} value is 0.05 GPa. In this case also, the theoretical value for the hardness on the order of 10^{-2} GPa, corresponds well with the experimental values measured for the films (shown in Table 6.1).

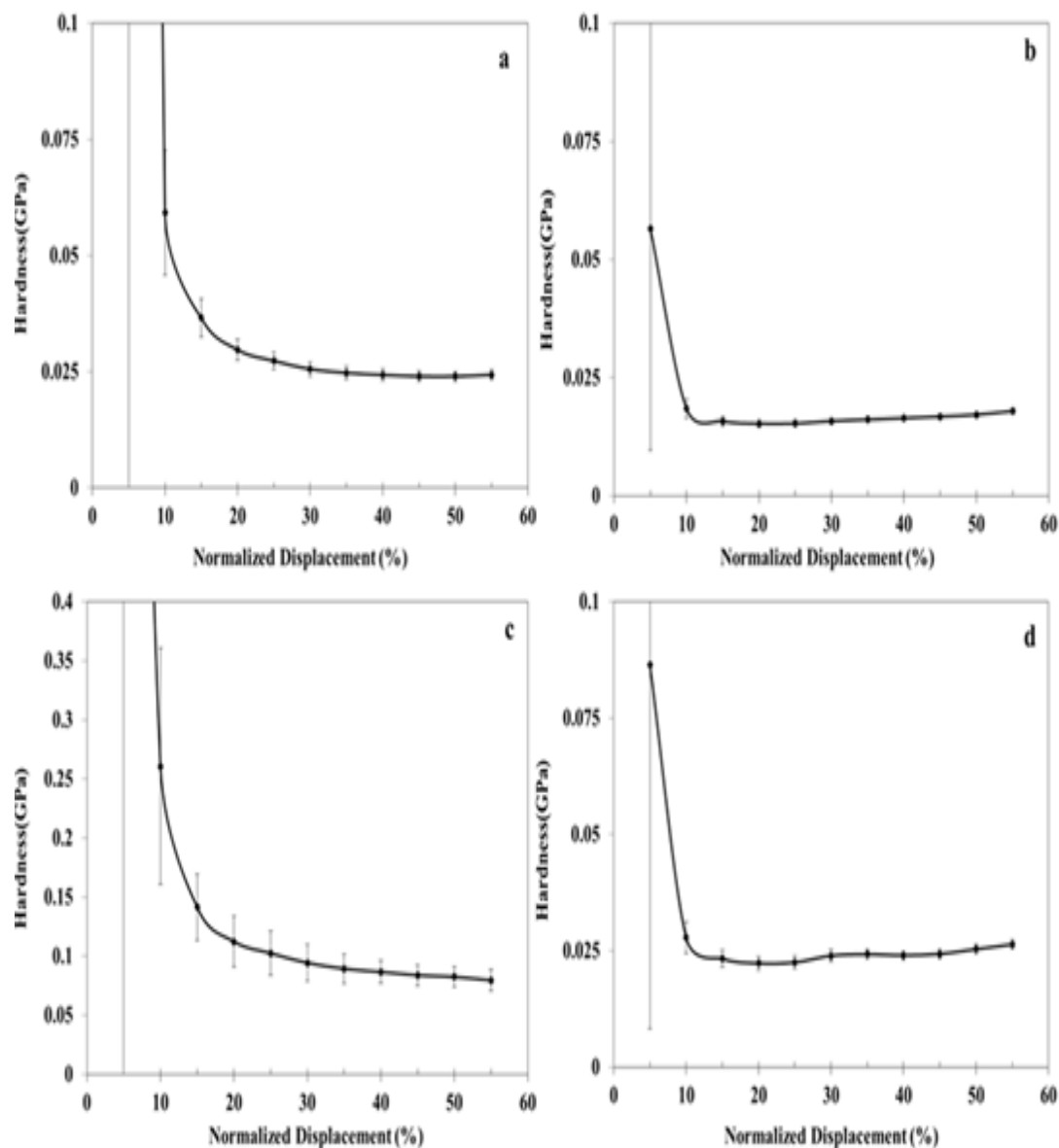


Figure 6.8. Hardness as a function of normalized displacement for different SIBS films. Figures 6.8a and 6.8b: Corresponding results for films with sulfonation percent of 20% and fabricated at 5 wt% and 10 wt% polymer concentration, respectively. Figures 6.8c and 6.8d: Corresponding results for films with sulfonation percent of 70% and fabricated at 2.5 wt% and 5 wt% polymer concentration, respectively.

6.2. Mechanical Characterization

6.2.1. Sulfonation Percent Effects

Figure 6.9 shows the mechanical properties as a function of sulfonation percent in the range from 0% to 80% for SIBS thin films fabricated at 2.5 wt%, 5 wt%, and 10 wt% polymer concentration. Figures 6.9a and 6.9b correspond to substrate-independent elastic modulus and hardness, respectively.

The results shown in Figure 6.9a suggest that regardless of polymer concentration, the elastic modulus increases with sulfonation percent in the range of 0 to 45%. However, at higher sulfonation percent, the trend in the elastic modulus is different for the films fabricated at 2.5 wt% and 5 wt% polymer concentration. For the 2.5 wt% polymer concentration film, the elastic modulus increases with the sulfonation percent, reaching a maximum value of 1.14 GPa at 80% sulfonation, whereas the elastic modulus progressively decreases for the 5 wt% polymer concentration film. A similar behavior is observed for the hardness of the SIBS thin films.

Both, the elastic modulus and hardness, increase with sulfonation percent in the range of 0% to 45 % likely as a result of changes in the phase-separated morphology of the films.

AFM results suggested a morphological transition for SIBS films from a short-range ordered cylindrical/lamellar morphology to a more disordered morphology (network-like structure) as the sulfonation percent increased from 0% to 45%. As such, a network-like structure is likely to produce more rigid polymers as compared to a cylindrical/lamellar

morphology because in a continuous network, polymer chain mobility is more restricted as compared to a morphology with non-interconnected domains.

However, despite the films fabricated from SIBS80 polymer also exhibited a network-like structure, the results for the samples fabricated at 5 wt% polymer concentration indicated that both the elastic modulus and hardness considerably decrease at a sulfonation percent of 80%. A potential explanation for this finding could be that the moisture content is significantly higher for films with high sulfonation percents due to the hydrophilic nature of sulfonic acid groups. Also, the films thickness noticeable increases with the sulfonation percent for the 5 wt% polymer concentration films. This, in turn, could favor solvent retention since the diffusion resistance increases with the film thickness. In addition, the solvent retention in ionomers can also increase with the sulfonation percent, likely due to: (1) the interaction between the solvent and the sulfonic groups¹⁵⁰ and (2) the solvent trapped in the network-like structure (nanochannels) that takes place at high sulfonation percent. In order to confirm this hypothesis, the thermal behavior for all of the SIBS polymers was evaluated using DSC analysis.

Figure 6.10 presents the DSC curves for SIBS polymers with different sulfonation percents. The data presented is for the first heating step in the cycle. The results reveal the presence of an endothermic peak in the data for the SIBS45 and SIBS80 polymers. While the SIBS45 polymer exhibits a maximum heat flow value of 18 mW/g at 170°C, the SIBS80 polymer shows a maximum heat flow value of 45 mW/g. In contrast, the curves for the unsulfonated polymer, as well as for the polymer with low sulfonation percent (SIBS20), did not exhibit any endothermic peaks.

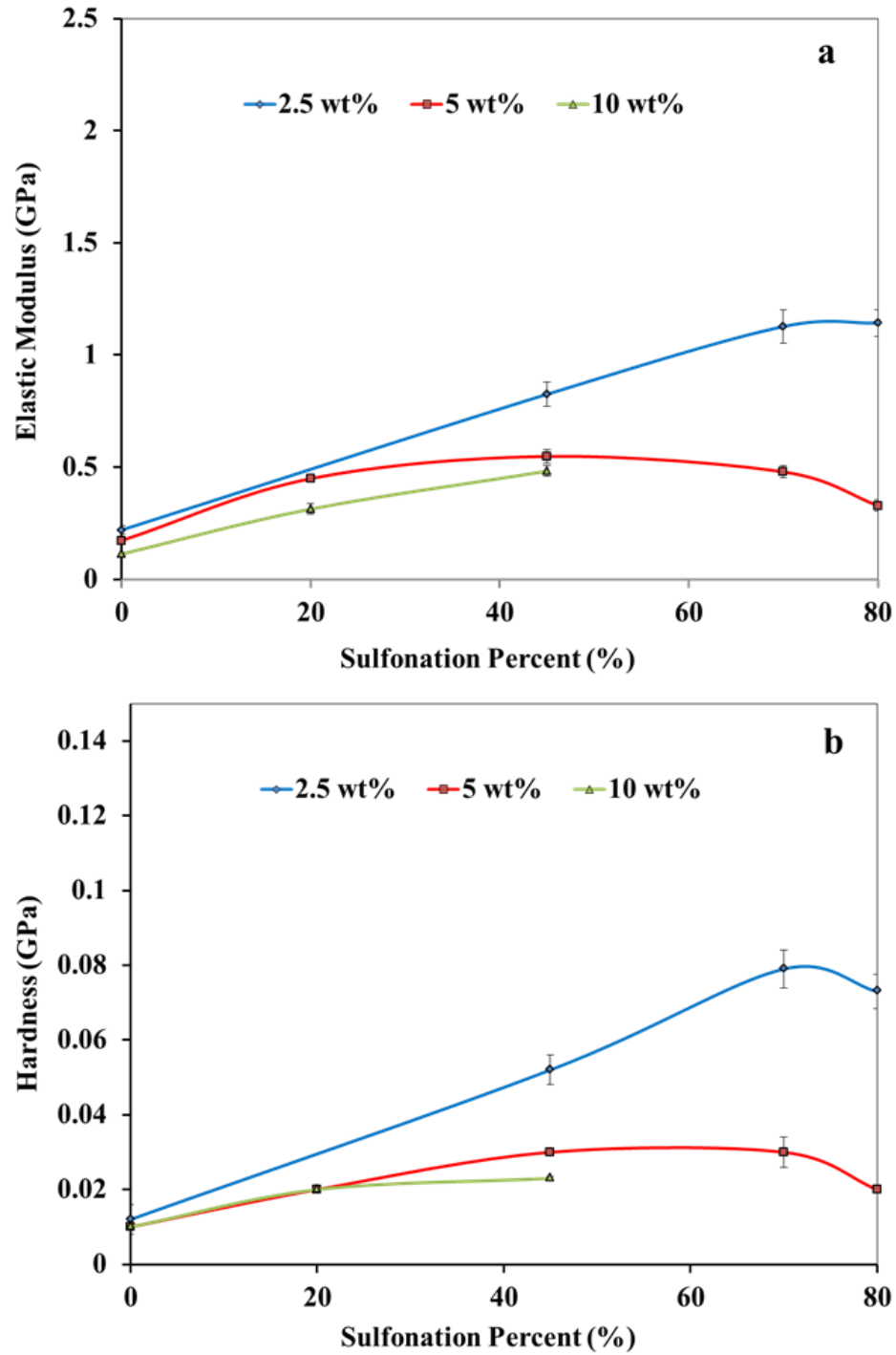


Figure 6.9. (a) Substrate-independent elastic modulus and (b) hardness for SIBS thin films as a function of sulfonation percent and polymer concentration.

Usually, the solvent and/or moisture evaporation result in an endothermic peak in the first-heating step DSC curve, which tends to disappear in the subsequent re-heating stages. The evaporation of high quantities of solvent (or moisture) requires higher heat flows to maintain the set temperatures, resulting in more pronounced endothermic peaks. Therefore, the observed endothermic peaks suggest the presence of residual solvent and/or moisture in the films with higher sulfonation percents. Moreover, since the intensity of the endothermic peak significantly increases with the sulfonation percent, it is possible to conclude that the solvent retention in the SIBS polymers significantly increases with the sulfonation percent.

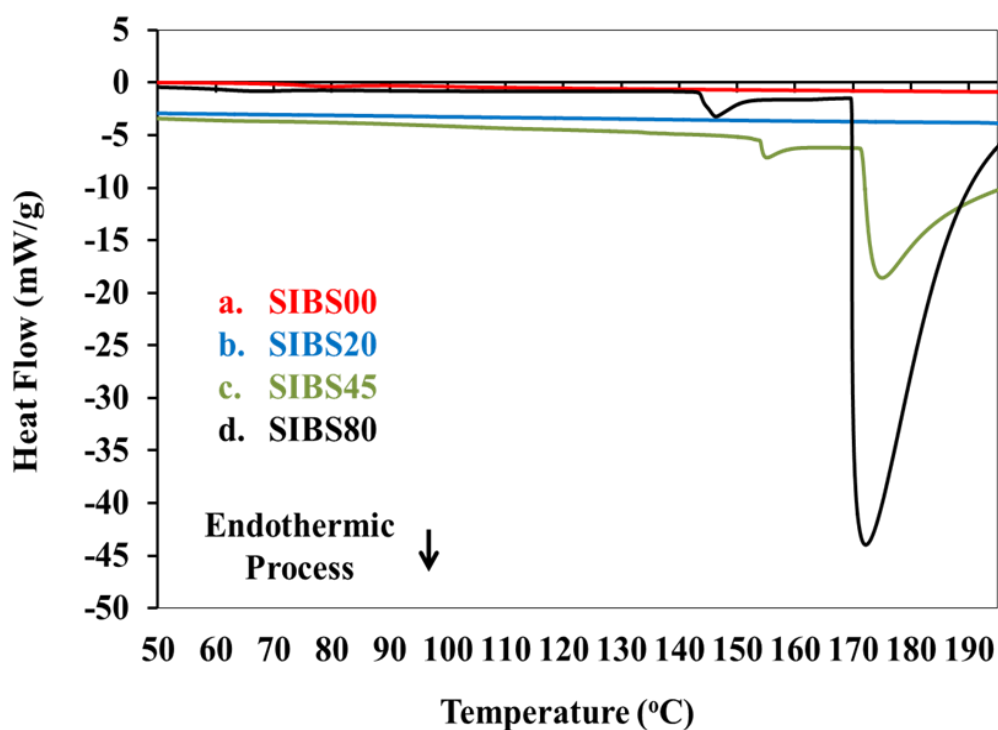


Figure 6.10 DSC curves for SIBS polymers with sulfonation percents of: (a) 0%, (b) 20%, (c) 45%, and (d) 80%. Data presented is for the first-heating step in the cycle.

Figure 6.11 shows the TGA curves for SIBS polymers with sulfonation percents of 0%, 20%, 45%, and 80%. All the curves for sulfonated polymers exhibit three weight loss stages. The first one is observed in the temperature range from 50 to 200°C, whereas the second and third can be observed in the range from 200 to 330°C and from 330 to 450°C, respectively. However, the discussion focuses on the first weight loss stage (50 - 200°C) as this is the area typically related to the evaporation of atmospheric moisture absorbed by the sulfonic groups as well as to the evaporation of residual solvent. The TGA curves clearly show that the weight loss (first stage) increases with the sulfonation percent. While the unsulfonated SIBS polymer does not exhibit weight loss, the SIBS80 polymer shows a weight loss of approximately 15%. These findings clearly suggest that the retention of both water and solvent increase with the sulfonation percent, which is also consistent with the DSC data presented in Figure 6.10.

Both moisture and residual solvent could act as plasticizers in the polymer matrix and, in turn, result in a significant reduction in the mechanical properties.^{151,152,153} In general, plasticizers are small molecules that upon insertion between macromolecular chains could weaken the intermolecular forces between them.¹⁵⁴ In this case, the strong hydrogen bonds, acting between the sulfonic acid groups, could be weakened by the presence of moisture and residual solvent, and thus result in a considerable reduction in the mechanical properties of highly sulfonated SIBS films.

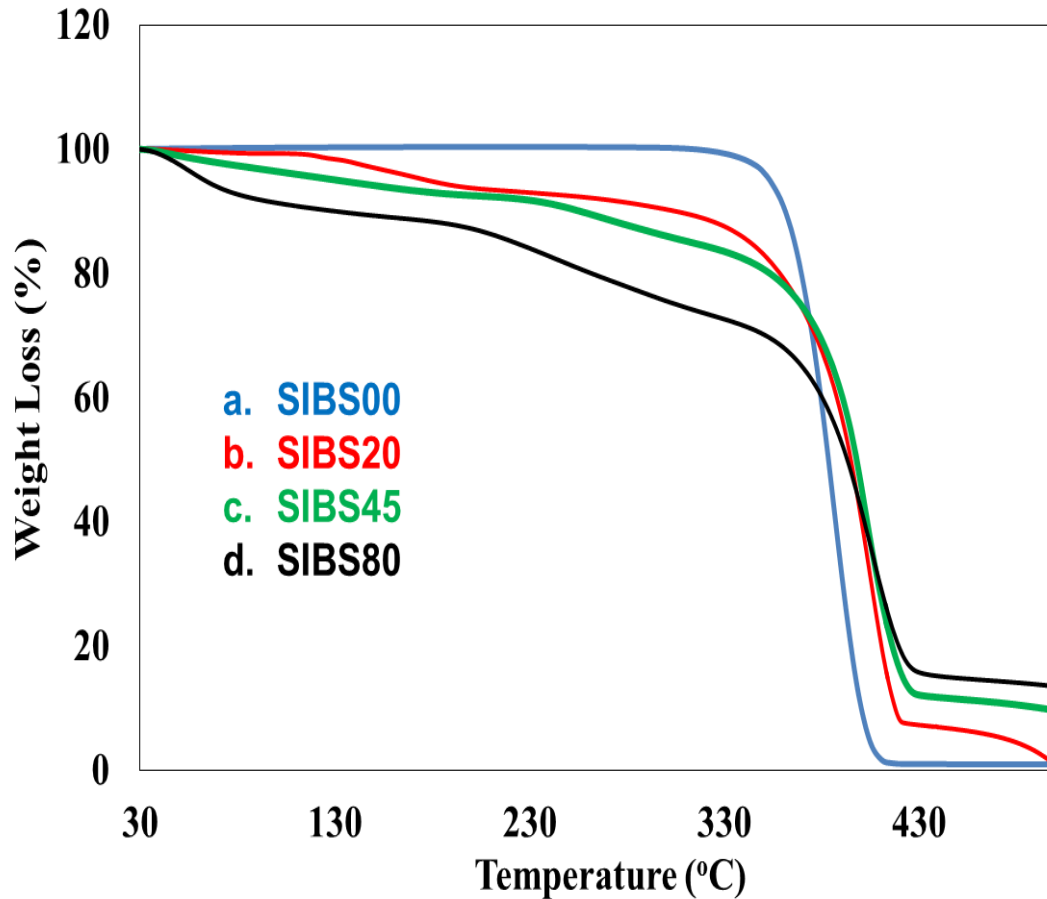


Figure 6.11 TGA curves for SIBS polymers with sulfonation percents of: (a) 0%, (b) 20%, (c) 45%, and (d) 80%.

6.2.2. Polymer Concentration Effects

The results presented in Figure 6.9 also reveal the strong effect of the polymer concentration on the mechanical properties of the SIBS thin films. For example, for films with sulfonation percent of 45 %, the elastic modulus decreases from 0.82 GPa to 0.48 GPa and the hardness decreases from 0.052 GPa to 0.020 GPa as the polymer concentration is increased from 2.5 wt% to 10 wt%.

In general, the elastic modulus and the hardness decrease with increasing polymer concentration but the differences are more pronounced towards the highly sulfonated films.

The effect on the mechanical properties of the SIBS thin films as a function of polymer concentration is likely related to differences in the resulting thickness of the films. For example, the SIBS thin films with sulfonation percent of 45% experienced an overall increase of almost ten times in thickness as the polymer concentration increased from 2.5 wt% to 10 wt%. Similarly, for the rest of sulfonated samples, the films also experienced an increase in thickness with the polymer concentration. The thickness data for the films was previously presented in Table 4.1. However, it is important to note that regardless of film thickness, all the samples were subjected to the same drying conditions. As such, thicker films could contain more humidity and residual solvents that could act as plasticizers as compared to thinner films due to the fact that diffusion resistance increases with film thickness.

Another potential explanation for the fact that the mechanical properties of SIBS thin films increase as the film thickness decreases, could be that for deep indentations, especially in thinner films, the polymer chains are greatly restricted in the narrow space between the indenter and the substrate. Hence, the inhibited mobility of the polymer chains promotes polymer stiffening. This phenomenon, known as hard-wall effects, was also observed by Zhou and co-workers¹⁵⁵ when investigated the effect of film thickness on the mechanical properties of poly (methyl methacrylate) thin films deposited on silicon wafer.

6.2.3. Temperature Effects

Nanoindentation tests were performed under different temperature conditions on SIBS and Nafion[®] thin films in order to study the effect of temperature on the mechanical properties of the materials. **Figures 6.12a** and **Figure 6.12b** present the data for the elastic modulus and hardness, respectively, for a variety of SIBS and Nafion[®] films as a function of temperature.

In this case, the elastic modulus was calculated using the NanoSuite[®] G-Series Hot Stage Hardness and Modulus method. As mentioned in section 3.2.7, this method is based on the standards *O&P* method.

The results in Figure 6.12a show that, for the unsulfonated sample (SIBS00-C), the elastic modulus remains relatively constant (at 0.375 GPa) in the temperature range of 30 to 100°C. However, at 130°C it was not possible to determine the mechanical properties for this sample. Unfortunately, the SIBS00 polymer exhibits a T_g on the order of 98°C (see Fig. 5.7) and therefore, when the unsulfonated SIBS sample is heated above this temperature (T_g), the polymer behaves as a viscous liquid and data cannot be collected using the nanoindentation system.

These results also suggest that the thermo-mechanical stability of unsulfonated SIBS directly depends on the T_g of the PS blocks. In fact, low-molecular weight amorphous PS polymer also exhibits an abrupt decrease in the storage modulus E' at it T_g (E' approaches

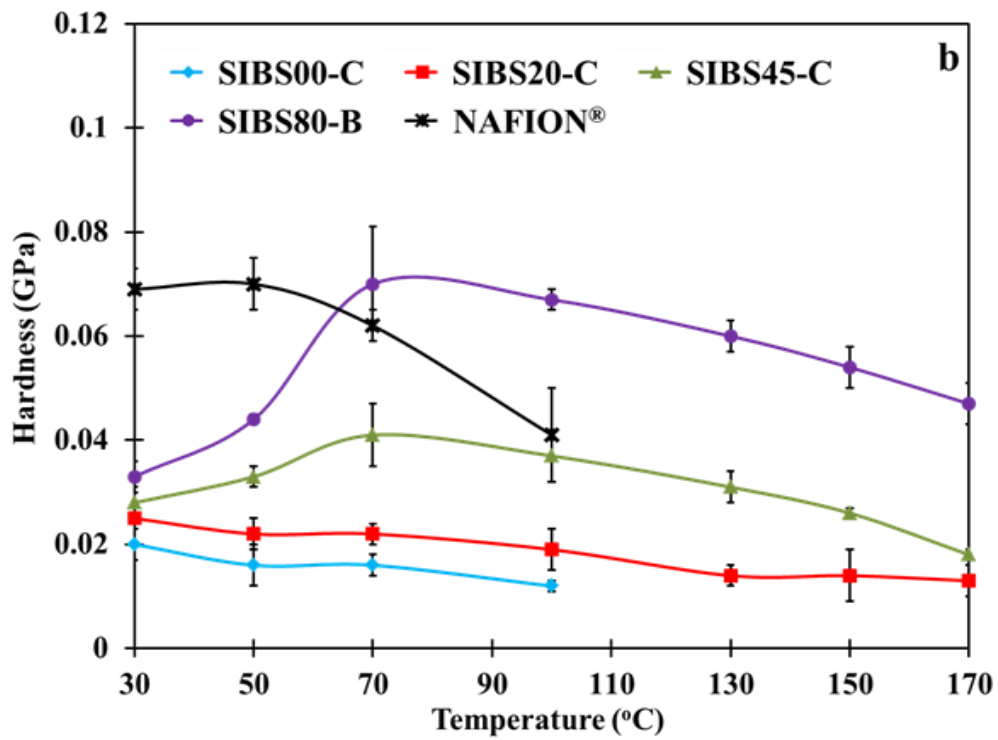
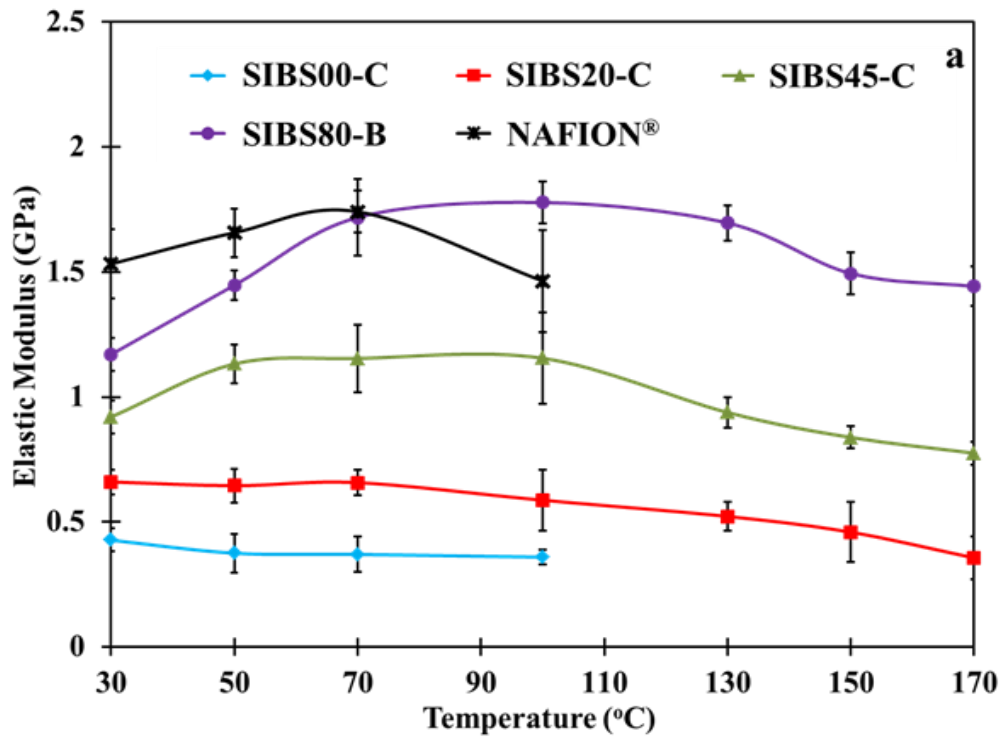


Figure 6.12 (a) Elastic modulus and (b) hardness as a function of temperature for a variety of SIBS and Nafion® films.

to zero), due precisely to the noticeable viscous flow that take place above this temperature.

In comparison, the sample with 20% sulfonation (SIBS20-C) shows a different behavior. In this case, the elastic modulus remains constant up to about 100°C and then gradually decreases from an average value of 0.657 GPa to 0.356 GPa as the temperature increases from 100°C to 170°C. For the samples with sulfonation percents above 45%, the elastic modulus initially increases with temperature, then exhibits a region of constant behavior and finally decreases in the range near 170°C. However, the initial increase in the elastic modulus observed at low temperatures is much more significant for the SIBS80-B sample. In addition, the region of constant elastic modulus behavior also extends to a higher temperature as compared to the other samples.

For the Nafion[®] film, the elastic modulus shows an increasing trend from an average value of 1.53 to 1.74 GPa as a function of temperature from 30 to 70°C. Beyond this temperature, no further measurements were possible. A possible explanation for this behavior could be the fact that Nafion[®] has a transition temperature below 130°C. More specifically, Yeo and Eisenberg¹⁵⁶ observed a α transition in Nafion[®] at 111°C, which was related to the long-range motion of the polytetrafluoroethylene (PTFE) backbone. Similarly, Jung and Kim¹⁵⁷ observed a T_g for Nafion 117 at 125°C, which was also assigned to the relaxations of the PTFE backbone. In addition, Martinez *et al.*¹⁵⁸, studied the thermal transition of Nafion[®] membranes in the H⁺ form with an equivalent weight 1100. They observed a thermal transition around of 100°C which was attributed to the T_g of the polar phase (ionic domains) of Nafion[®]. According to the last, it is likely that the

viscous flow experienced by the Nafion[®] at temperatures above its T_g causes excessive thermal drift.

Similar trends are observed with the hardness of the materials as a function of temperature. The results presented in Figure 6.12b show that the samples with low sulfonation percents (SIBS00-C and SIBS20-C) exhibit a reduction in hardness as the temperature increases. In contrast, for the samples with high sulfonation percents (SIBS45-C and SIBS80-B), hardness increases in the range of temperature from 30 to 70°C. Beyond 70°C, the hardness progressively decreases with temperature from an average value of 0.041 to 0.018 GPa for the SIBS45-C sample, and from 0.070 to 0.047 GPa for the SIBS80-B sample.

For the Nafion[®] film, hardness initially increases from an average value of 0.069 to 0.070 GPa in the temperature range from 30 to 50°C, and then suddenly decreases to 0.041 GPa at 100°C.

In general, these results suggest that sulfonated thin films possess higher thermo-mechanical stability as compared to unsulfonated SIBS and Nafion[®] films, even at low sulfonation percent.

Also, the increasing trend observed in the mechanical properties for the samples with high sulfonation percent between 30 and 70°C, can likely be attributed to losses in moisture (plasticizer), which in turn, result in a stiffer polymer matrix. The moisture that is eliminated by moderate heating, corresponds to (1) the water of adsorption retained in the film by physical absorption (Van der Waals forces) and (2) the water of capillarity contained in the narrow porous of the films.^{159,160,161}

For the SIBS80-B sample, the constant elastic modulus behavior extends to a higher temperature, likely because the inclusion of a higher amount of sulfonic groups in into the polymer matrix generates bulkiness. Thus, the amount of thermal energy that is necessary to move a closely-packed chain is much larger than those required to move a chain with significant free volume.

It should be also considered that the “physical” crosslinks (hydrogen bonds) formed through the polymer matrix of sulfonated SIBS also prevent the complete viscous flow in the temperature range of 130 to 170°C. The last, is likely the mainly reason why the inclusion of sulfonic groups causes an increase in the T_g of the sulfonated polymers.^{162,163}

It has also been reported that sulfonation of PS blocks considerably improves the thermomechanical stability of SIBS block copolymers. For example, Crawford *et al.*⁵⁴ studied the effects of sulfonation on the mechanical properties of SIBS in bulk through Dynamic Mechanical Analysis (DMA). They found that SIBS is more thermally stable as compared to the unsulfonated block copolymer, since in the former there was no indication of changes in storage modulus (E') at 100°C, unlike unsulfonated copolymer where E' significantly decreased. They also suggested that the enhancement of the high-temperature modulus with sulfonation is likely to occur as a result of increases in hydrogen bonding of sulfonic acid groups, which in turns leads to increased “physical” crosslinking.

In turn, all of the sulfonated samples experienced a progressive decrease in mechanical properties with further increase in temperature likely due to the fact that high kinetic

energy disrupts the physical crosslinks, which in turn result in the softening of these materials.

6.2.4. Hydration Treatment Effects

Nanoindentation was also used to explore the variation in mechanical properties associated with the hydration treatment of SIBS thin films. **Figure 6.13** presents the mechanical properties for both the dry and the hydrated samples for four SIBS thin films with different sulfonation percents. Figure 6.13a and 6.13b correspond to substrate-independent elastic modulus and hardness, respectively.

These results suggest that the hydration treatment had no effect on the mechanical properties of SIBS thin films. However, it has been reported that high water retention within a polymer matrix (in bulk) can deteriorate its mechanical properties¹⁶⁴, a possible explanation for these results could be that the hydration time (12 hours) was not long enough to completely hydrate the films. Another hypothesis to support these findings may be related to the desorption of the adsorbed moisture during the indentation experiments, since the loading step does not start until the thermal drift rate drops below 0.05 nm/s and this process typically takes 2-3 hours. In order to overcome this drawbacks, it is possible to perform experiments at higher thermal drifts to eliminate or reduce desorption of water from the samples.

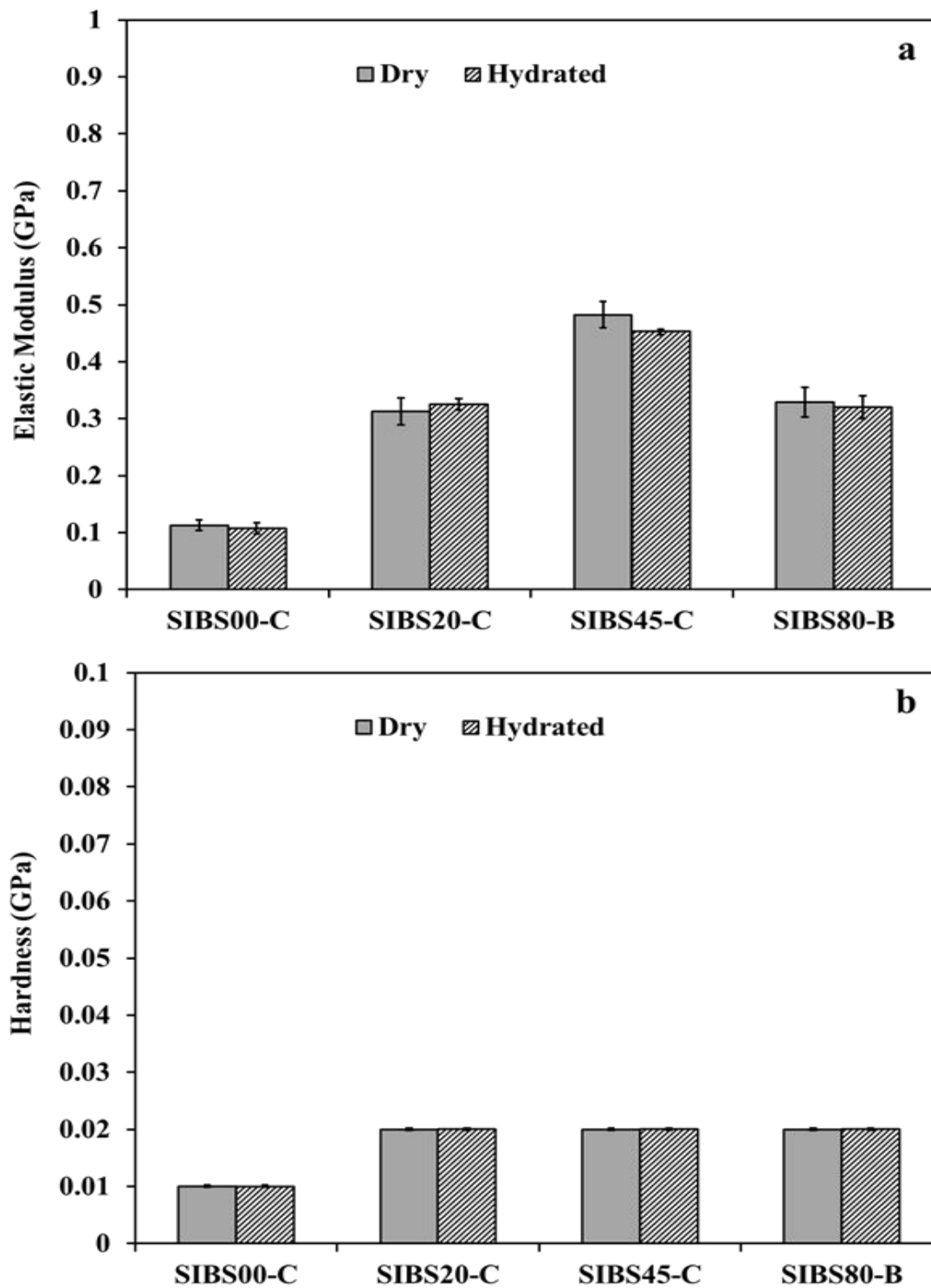


Figure 6.13. Hydration treatment effect on the mechanical properties of SIBS thin films: (a) elastic modulus and (b) hardness for different SIBS.

However, it is important to note that in the case of standards *O&P* method, a high thermal drift could have significant effect on the results.

Another alternative could be to perform the nanoindentation experiments at controlled humidity levels (in the range from 5% to 90% relative humidity) using a humidity control stage compatible with the Agilent G200 NanoIndenter series.

6.3. Summary

Instrumented nanoindentation was used to determine the mechanical properties of SIBS and Nafion[®] thin films. A variety of experiments were performed to evaluate the effects of critical variables on the mechanical properties of SIBS thin films. Similarly, the effects of the hydration and temperature on the mechanical properties of these films were also studied.

The results showed that the mechanical properties increased with the sulfonation percent in the range from 0% to 45%. However, at high sulfonation percent, the trend in the mechanical properties is different for the films fabricated at 2.5 wt% and 5 wt% polymer concentration. For the 2.5 wt% polymer concentration films, the mechanical properties increase with the sulfonation percent, whereas the mechanical properties progressively decrease for the 5 wt% polymer concentration films most likely as a result of higher solvent/moisture retention into the films.

In contrast, the mechanical properties significantly decreased with polymer concentration regardless of the sulfonation percent. It was also possible to establish a relationship

between the morphology and the mechanical properties for the SIBS films. In general, films with a network-like morphology exhibited improved mechanical properties as compared with those showing a morphology comprised of non-interconnected domains. Also, SIBS thin films were thermo-mechanically more stable than Nafion[®] films, even at low sulfonation percent. It was also observed that for samples with high sulfonation percents, the decline in elastic modulus began at higher temperatures. In turn, hydration treatment had no significant effects on the mechanical properties of SIBS thin films.

CHAPTER 7

ADHESION CHARACTERIZATION OF SIBS THIN FILMS

The results obtained from the scratch adhesion tests performed on the fabricated MEAs are presented and discussed in this chapter. The effects of the mechanical properties on the practical adhesion of the SIBS thin films to Pd electrodes are also described in detail.

7.1. Practical Adhesion Measurement

SIBS and Nafion[®] thin films were subjected to scratch tests to evaluate their practical adhesion to palladium (Pd) electrodes. **Figure 7.1** shows the characteristic displacement curve for a scratch test performed on each sample. Figure 7.1a to Figure 7.1e correspond to SIBS00-C, SIBS20-C, SIBS45-C, SIBS80-B, and Nafion[®] samples, respectively. Each figure contains the original surface scan (blue trace), the ramp load scratch scan (green trace), and the residual deformation scan (orange trace). The dotted lines (parallel to the x axis) indicate the location of the polymer-Pd interface as determined by profilometry. The red dots illustrate the locus of adhesion failure. The load required to cause adhesive failure is also displayed in each figure.

Generally, the critical loads are determined based on three main criteria: (1) the detection of significant changes in the ramp load scratch displacement curves, (2) the amount of residual deformation, and (3) the location of the polymer-Pd interphase.

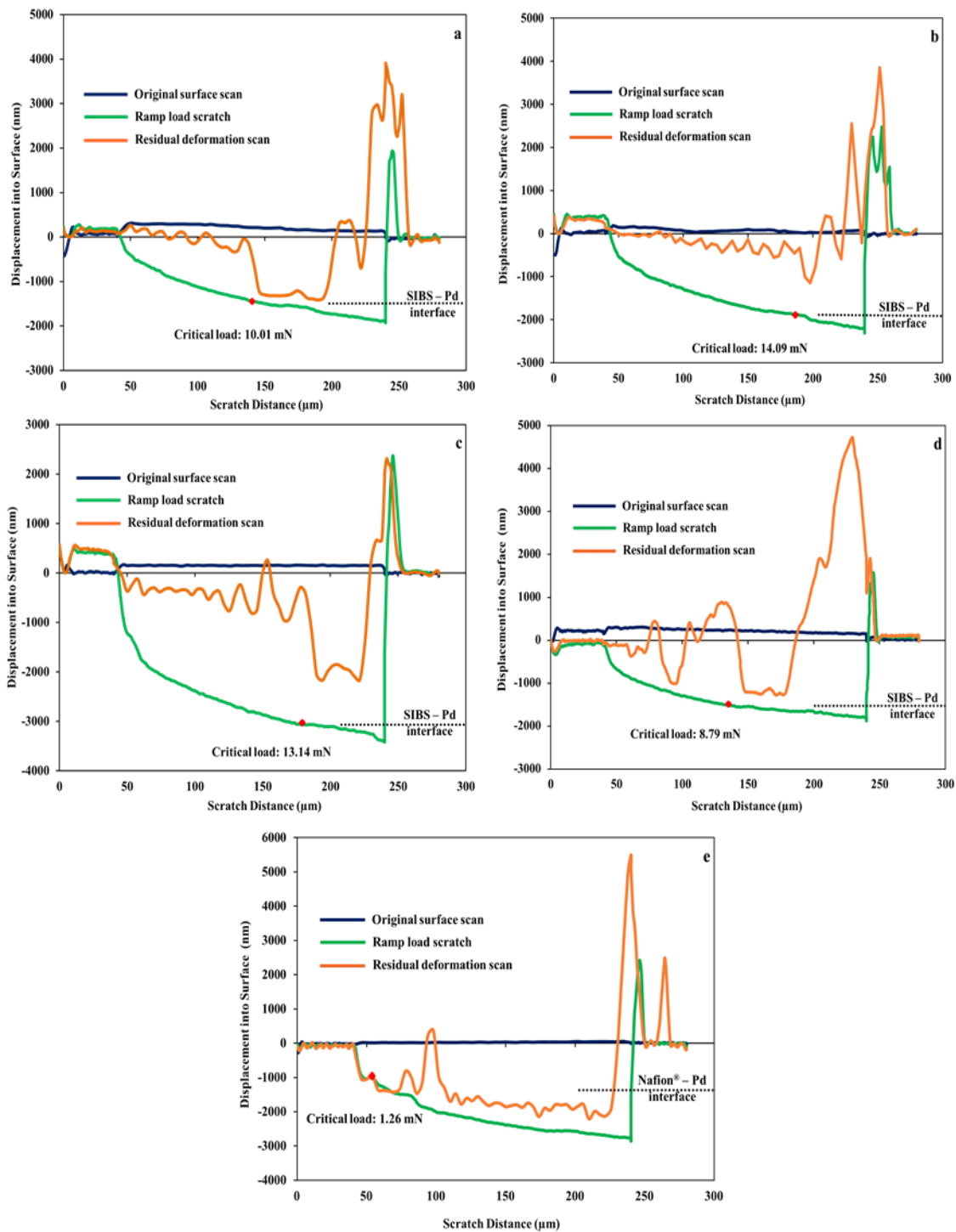


Figure 7.1. Displacement into the surface versus scratch distance data for the scratches performed on SIBS samples with sulfonation percents of: (a) 0%, (b) 20%, (c) 45%, and (d) 80%. Figure 7.1e corresponds to a scratch performed in Nafion[®].

All of the ramp load scan curves for the SIBS samples in Figure 7.1 indicate that the scratches progressed smoothly without any significant fluctuation in displacement into the surface (green lines). However, at a certain level of displacement into the surface, it is possible to observe that no further displacement is recorded for an incremental amount of applied load until the force applied is enough to penetrate into the surface of the Pd thin film. Then, the displacement into the surface continues to increase until the maximum load is reached (20 mN). In contrast, all the residual deformation curves exhibit small fluctuations in displacement into the surface even after the critical load.

On the other hand, when small fluctuations are only observed in the residual deformation curve, these are representative of small fracturing behind the tip during the experiment.¹⁶⁵ In turn, the abrupt change in displacement into the surface observed near the interface in all of the residual deformation curves is an indication of adhesive failure.¹⁶⁶ The critical load values for the studied samples are summarized in **Table 7.1**.

Table 7.1. Critical loads for the studied samples.

Sample	Critical Load (mN)
SIBS00-C	10.01
SIBS20-C	14.09
SIBS45-C	13.14
SIBS80-B	8.79
NAFION[®]	1.26

On the other hand, both ramp load scan and residual deformation scan curves for Nafion[®] (Fig. 7.1e), show abrupt fluctuations in displacement into the surface at 50 μm scratch distance. Since this abrupt decrease in penetration reaches the interface, it is possible to

consider an adhesive failure. The critical load required to cause delamination in this case was 1.26 mN.

An important observation is that the SIBS45-C sample exhibits the highest amount of elastic deformation (gap between the green and orange curves before the critical load). This result could have been expected because, even though the SIBS45-C sample has the highest thickness and therefore, the most material available to accommodate deformation, it also has the highest resilience among all the SIBS samples because of its high elastic modulus.

Another mechanical property that can be calculated using this technique is the coefficient of friction (CoF). According to ASTM D 7027-05, this coefficient can be defined as “the dimensionless ratio of the tangential force to the normal force applied to the indenter at a specific point in the scratch test”.¹⁶⁷ As such, abrupt changes in the CoF during scratch test can be correlated to the presence of damages in the film-substrate system.¹⁶⁸

Figure 7.2 displays the CoF data as a function of scratch distance for the sample presented in Figure 7.1. In general, the data shows two major peaks at the scratch distances of 40 and 240 μm , which correspond to the points where begin and end the ramp load scan scratch, respectively. Moreover, all of the curves also exhibit abrupt changes in the CoF along this segment, as a result of the presence of failures in the films. For example, the corresponding curve for the sample SIBS80-B exhibits abrupt changes at scratch distances of 75, 127 and 198 μm , which are consistent with the major fluctuations in displacement into the surface observed in its respective residual deformation curve (Figure 7.1d).

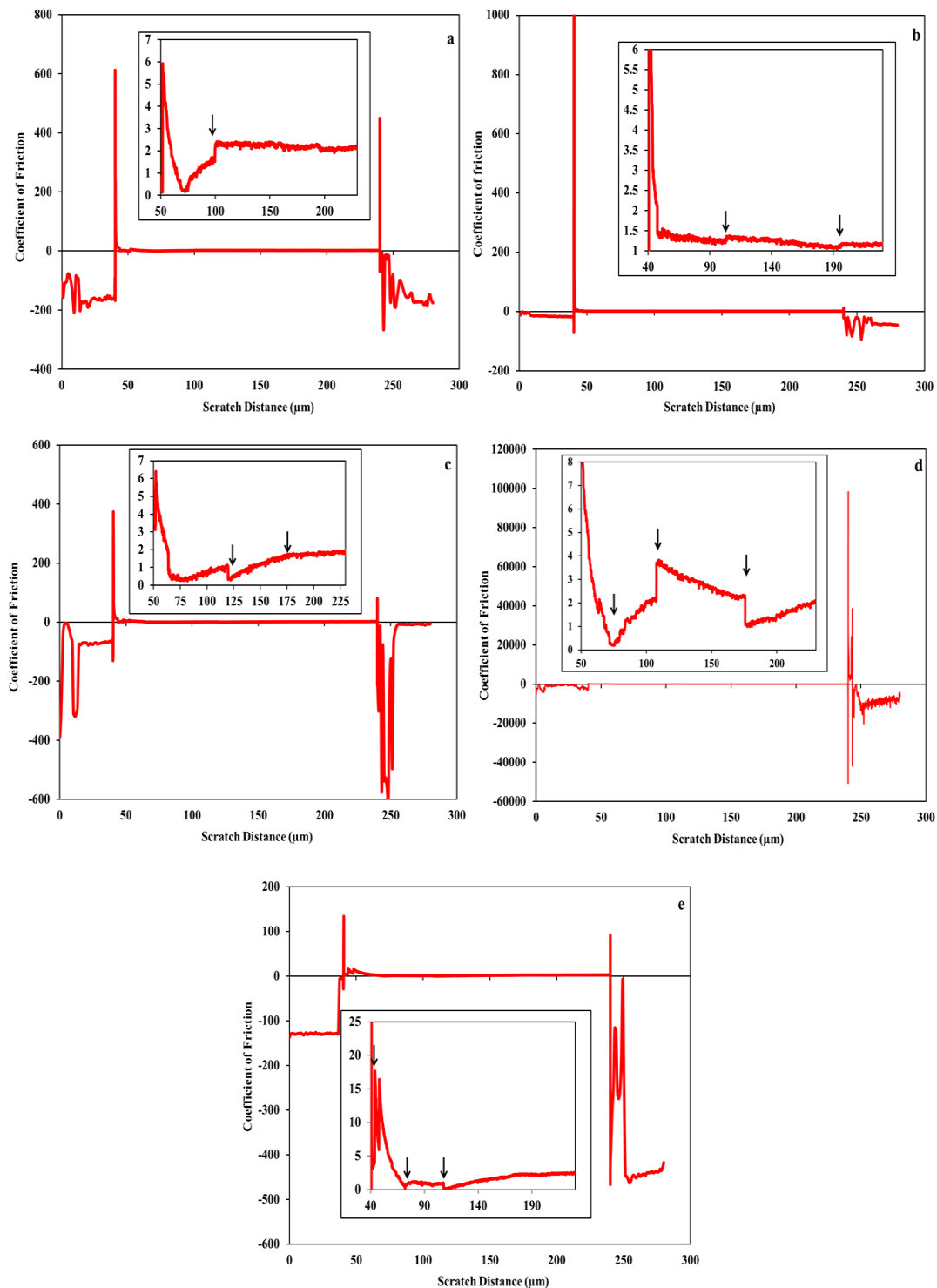


Figure 7.2. Coefficient of friction data versus scratch distance for the scratches performed on SIBS samples with sulfonation percents of: (a) 0%, (b) 20%, (c) 45%, and (d) 80%. Figure 7.1e corresponds to the data for the Nafion[®] film.

Similarly, the changes in CoF for the rest of the samples are also consistent with the failures observed in their respective residual deformation curves.

The scratch tracks were also evaluated in detail using scanning electron microscopy (SEM). Figures 7.3 to Figure 7.7 correspond to SEM images for the residual scratches performed on samples of SIBS00, SIBS20, SIBS45, SIBS80, and Nafion[®], respectively. Each figure consists of 6 images (except for Fig. 7.7), where the first image (labeled with the letter a) displays the scratch array performed on each sample. The rest of images correspond to magnified views of each of the labeled regions, namely I to V (or I to III in the case of Nafion[®]).

With respect to the details in Figure 7.3, the image for region I shows the initial part of the scratch where there is no evidence of any significant failure. In turn, the image for region II shows the typical residual groove followed by the film failure. In other words, this image shows the transition from where the polymer film undergoes plastic deformation to where it delaminates from the Pd electrode. This image also reveals noticeable overflow at the side of the groove. This phenomenon is called “pile-up” and is often observed when soft materials, like polymers, are scratched.¹⁶⁹ Subsequently, the images for regions III and IV show the film detachment. At these locations, the residual groove exhibits a width of approximately 4 μm and the illuminated region is likely a direct result of the exposed layer underneath. At the end of the track (region V), it is possible to observe the detached material forming a coil-like structure. This reflects the magnitude of the failure caused by the applied stress. Figures 7.4 to Figure 7.6 show a similar behavior as compared to the SIBS00 film (Fig. 7.3).

Figure 7.7 displays the SEM images for the scratch array performed on the Nafion[®] film. The image for region I shows adhesive failure (delamination) of the Nafion[®] film from the Pd electrode. As stated earlier, this failure occurs immediately after starting the ramp load scratch process. The rest of the images show additional magnified areas.

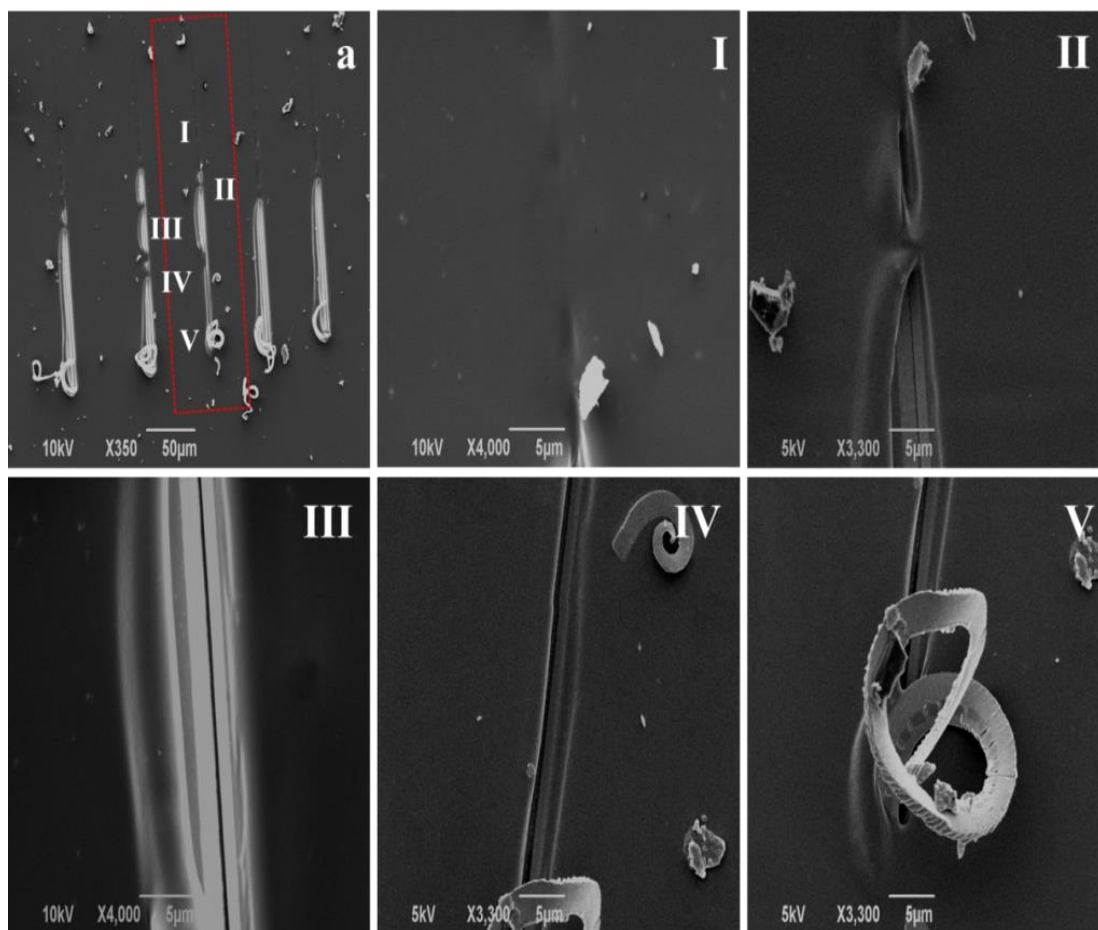


Figure 7.3. SEM images for scratches performed on the SIBS00-C film.

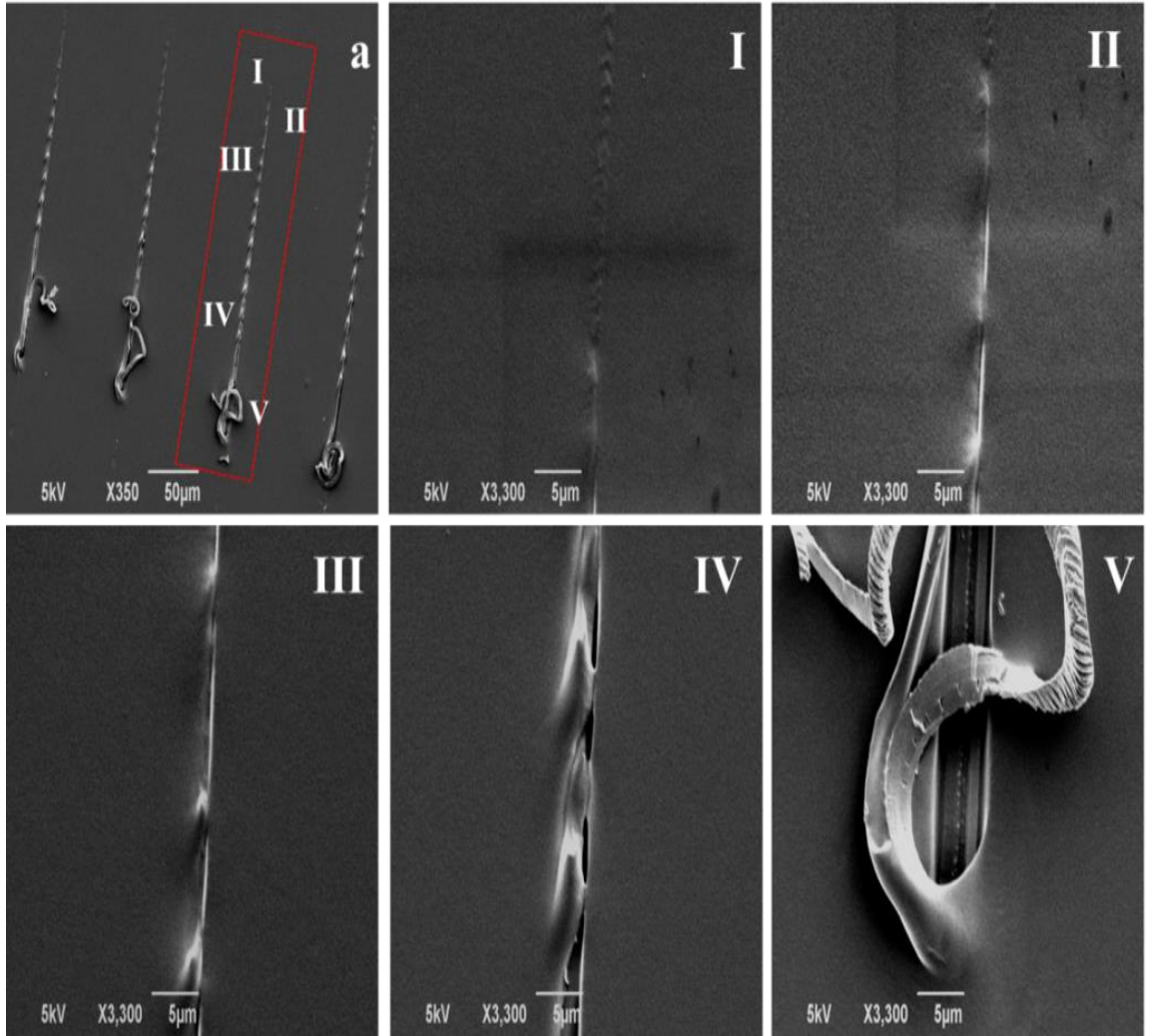


Figure 7.4. SEM images for scratches performed on the SIBS20-C film.

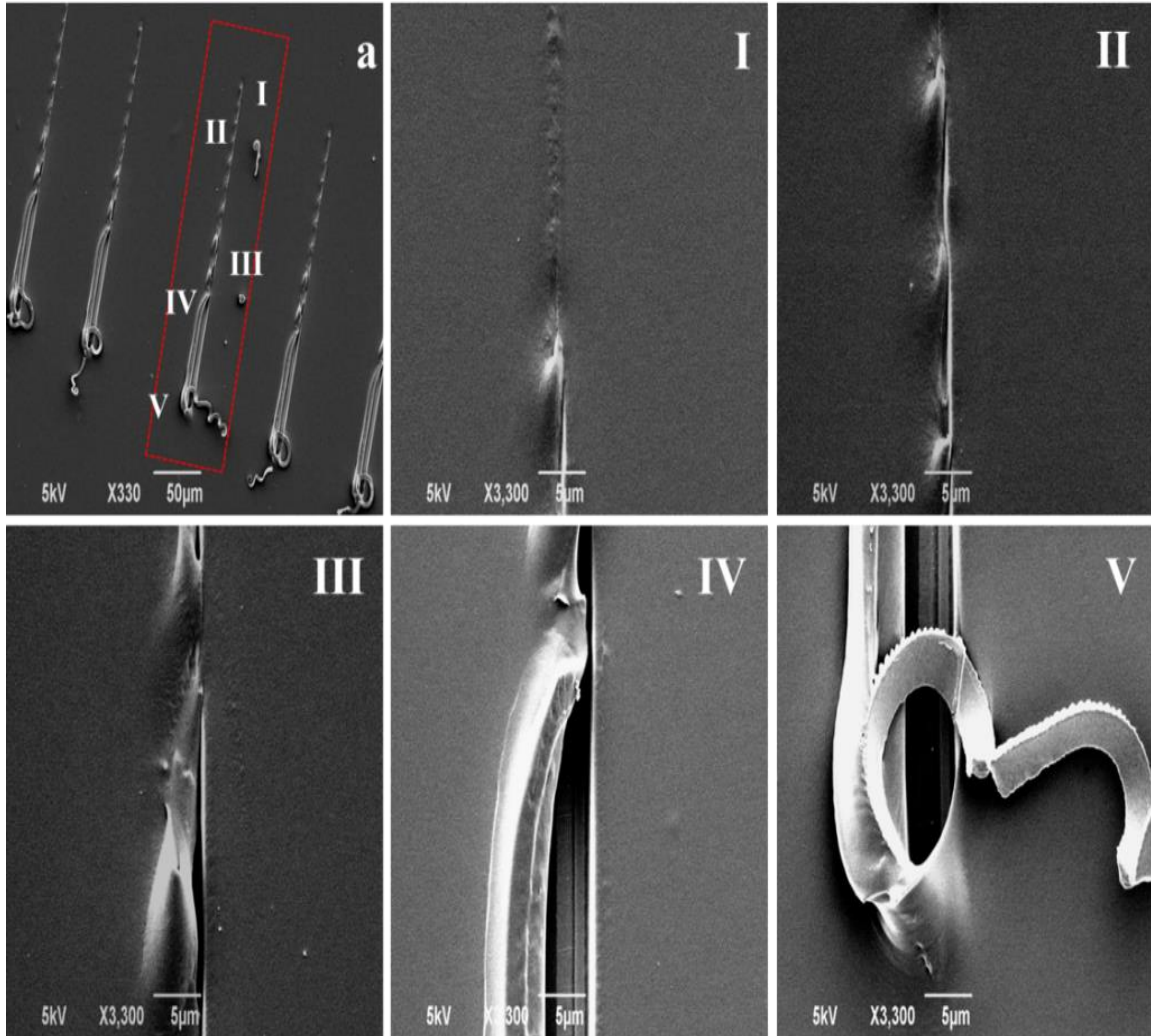


Figure 7.5. SEM images for scratches performed on the SIBS45-C film.

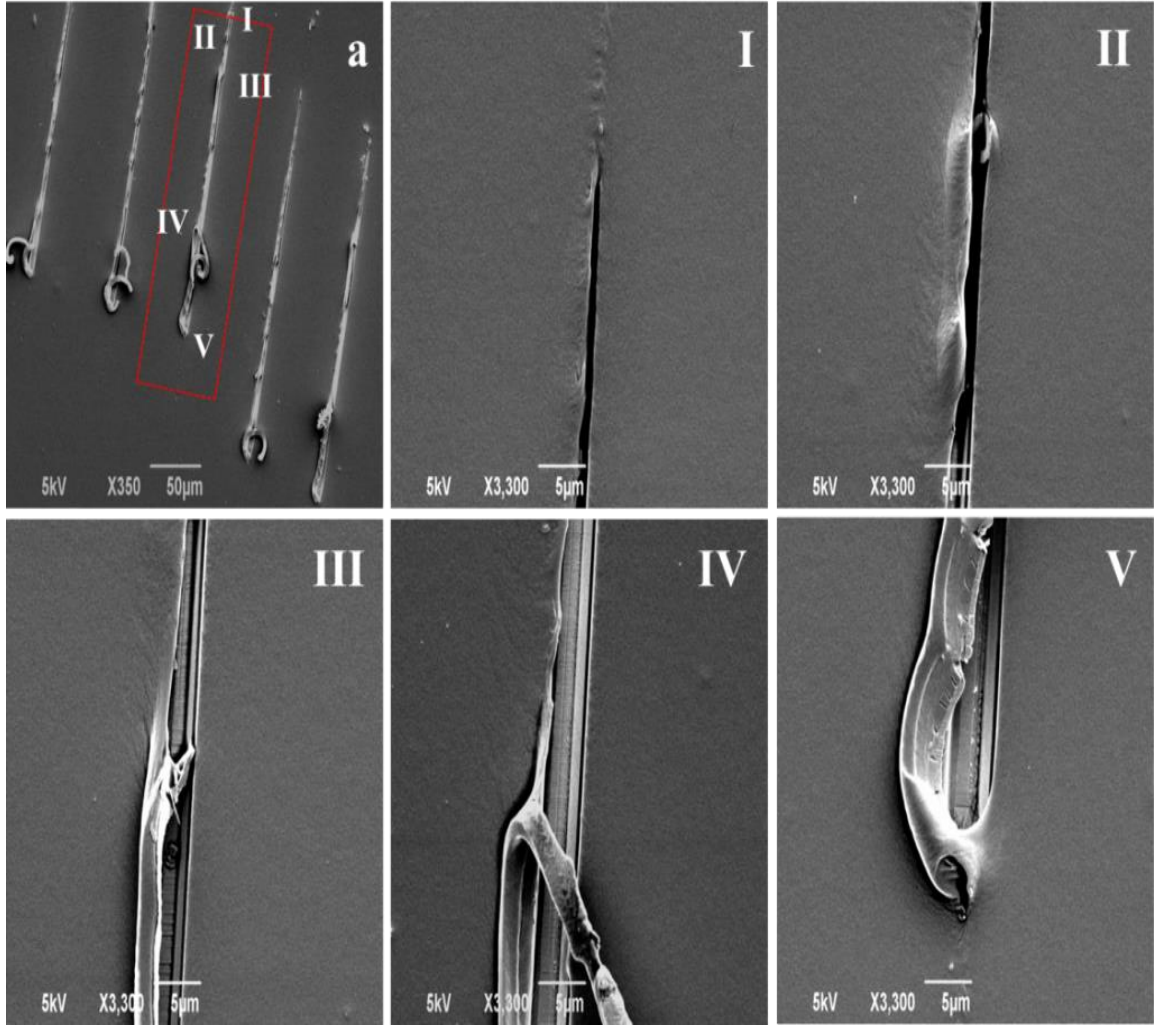


Figure 7.6. SEM images for scratches performed on the SIBS80-B film.

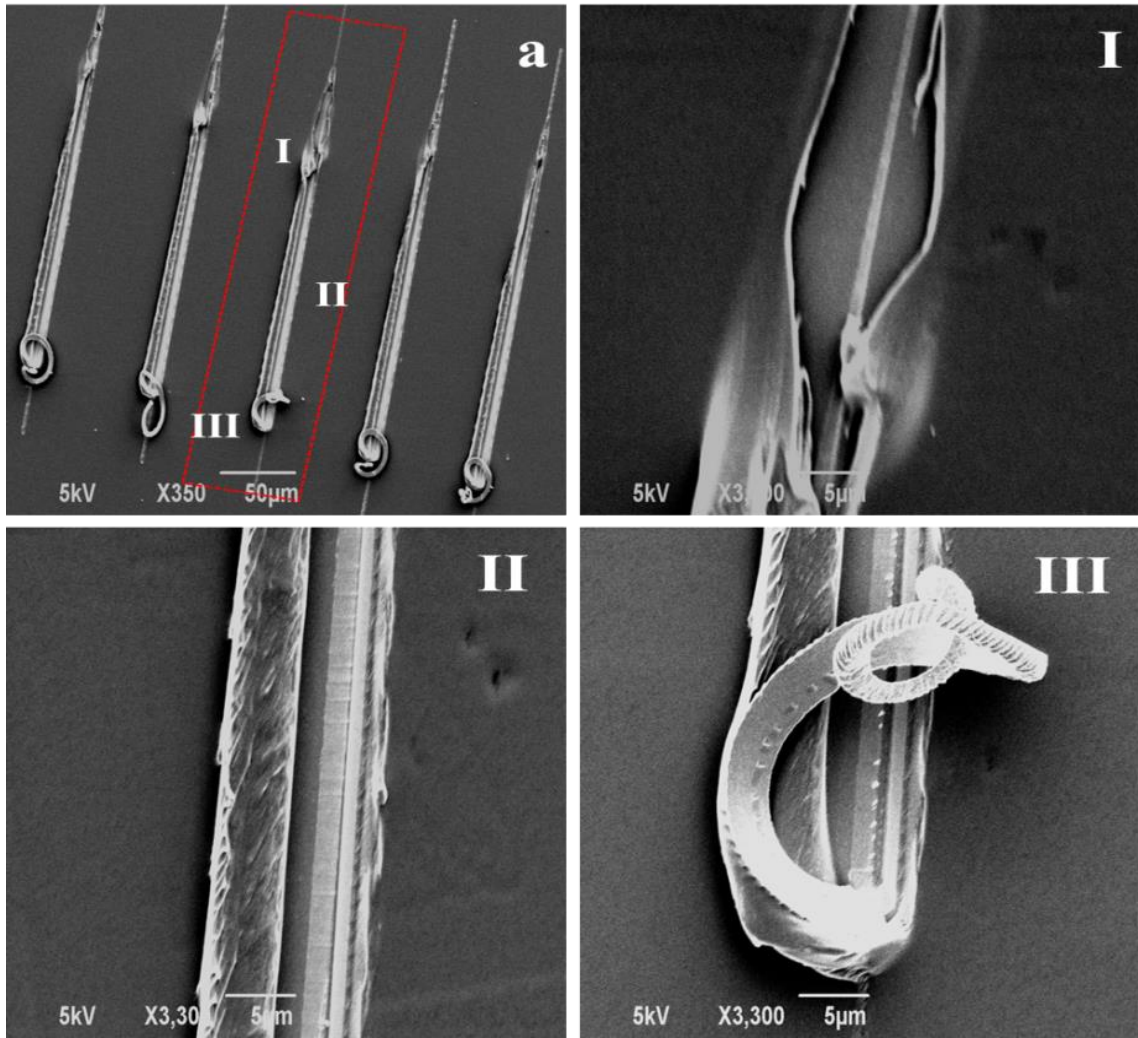


Figure 7.7. SEM images for scratches performed on the Nafion[®] film.

Figure 7.8 summarizes the average normalized critical load for the studied samples. This variable is defined as the ratio between the critical load and the film thickness.

An important observation is that all of the SIBS samples show higher normalized critical load values as compared to the Nafion[®] film. In addition, these results also suggest that the SIBS20-C sample has higher practical adhesion as compared to the others since it exhibited the highest normalized critical load (6.71 mN/ μ m). In comparison, the SIBS45-C film exhibits the lowest normalized critical load (4.22 mN/ μ m) amongst the SIBS samples. The error bars suggest significant variability in the results, most likely due to the short-range order morphology observed in the films.

In general, the results suggest that the practical adhesion for the SIBS thin films is higher as compared to the Nafion[®] film. In fact, the results suggest that causing adhesive failure in the SIBS samples requires normalized critical loads up to six times higher as compared to the Nafion[®] film.

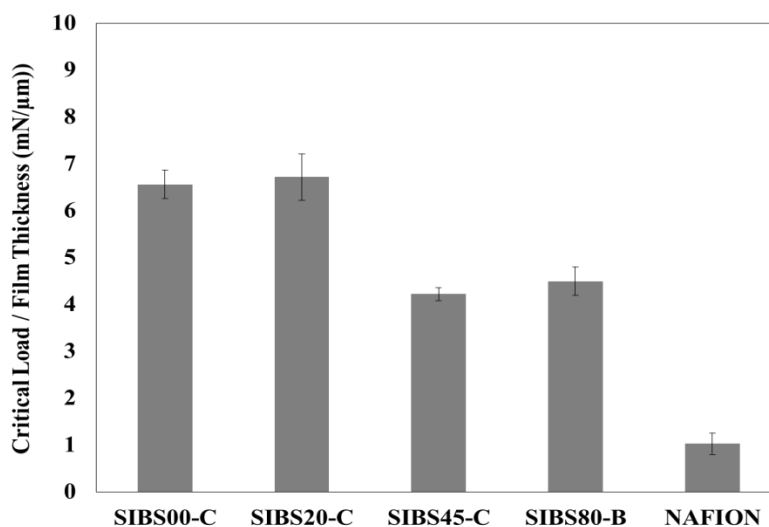


Figure 7.8. Average normalized critical load for the studied samples.

These results corroborate the poor adhesion of Nafion[®] to Pd electrodes. Unfortunately, the presence of fluorinated groups in Nafion[®] decreases its surface energy, which causes its poor adhesion to any other material. In addition, it is also important to consider the fact that Nafion[®] is much stiffer as compared to SIBS. It is possible that the high stiffness of Nafion[®] generates higher stresses in the film during the scratch test, which results in full film detachment even at lower loads.¹⁷⁰

Another important aspect that possibly explains the adhesive failures in the Nafion[®] is its high CoF. Comparing the results for the CoF (Fig. 7.2), it can be observed that the adhesive failure for the Nafion[®] film occurs at higher CoF. High CoF can be correlated to high tensile stress in the film, which in turn, promotes the development of failures such as crazing, cracking, and delamination.¹⁶⁵

7.3. Summary

Scratch tests were performed on different MEAs to investigate the practical adhesion between SIBS thin films and Pd electrodes. Similarly, a Nafion[®]-Pd system was evaluated for comparative purposes. It was found that SIBS thin films have higher practical adhesion to Pd electrodes as compared to the Nafion[®] film. In fact, the normalized critical loads for SIBS thin films were up to six times higher as compared to Nafion[®] film. It was also noticed that the high ductility (low elastic modulus) observed in the SIBS thin films has probably helped to prevent the formation of premature failures, which ultimately favored their practical adhesion to Pd electrodes.

CHAPTER 8

CONCLUSIONS

The purpose of this investigation was to evaluate the newly-developed SIBS polymers for potential applications in micro- and/or nanometer-sized electrochemical devices. The main goals were to develop SIBS into thin film technology and to perform the corresponding materials characterization studies with particular emphasis on the effect of critical variables. As such, the effect of sulfonation percent and polymer concentration on film morphology, as well as on the mechanical and adhesive properties of the films, were evaluated. In addition, the effect of hydration and temperature on the mechanical properties of the films was also studied. Nafion[®] thin films were assessed for comparative purposes.

Uniform and continuous SIBS thin films with different sulfonation percents were deposited onto silicon wafer substrates via spin coating using a variety of processing conditions. The results showed that the film continuity and uniformity was improved as a function of both, sulfonation percent and polymer concentration.

Overall, the optimum film quality likely requires a proper balance of the critical parameters because variations in the process variables could also result in more surface defects. The rapid evaporation of solvent and water during the spin-coating process induces “striations” and pin-hole formation in the films.

In terms of the morphology, AFM results revealed phase-separated morphologies with critical transitions from a short-range ordered cylindrical/lamellar morphology to a more disordered morphology (network-like structure) as the sulfonation percent increased from 0 to 80%. In addition, the results showed that the PS domain size increased with both, sulfonation percent and

polymer concentration. The thermal treatment used in the fabrication of the films also had a significant effect in re-ordering the morphology, but only in the cases where the annealing temperature was above the T_g of the polymer.

Nanoindentation results showed that the mechanical properties increased with the sulfonation percent in the range from 0% to 45%. However, at higher sulfonation percent, the trend in the mechanical properties was different depending on the polymer concentration used to fabricate the films. For the films with 2.5 wt% polymer concentration, the mechanical properties increased with the sulfonation percent, but the elastic modulus progressively decreased for the 5 wt% films most likely as a result of higher solvent and/or moisture retention in the films.

In general, films with a network-like morphology exhibited improved mechanical properties as compared to the films with morphologies comprised of non-interconnected domains. Also, SIBS thin films were more thermo-mechanically stable as compared to Nafion[®] films, even at low sulfonation percent.

Scratch adhesion tests indicated that SIBS thin films have higher practical adhesion to Pd electrodes as compared to Nafion[®] films. The normalized critical loads for SIBS thin films were up to six times higher as compared to Nafion[®] films.

RECOMMENDATIONS

Some possible recommendations for future work are described in this section.

In order to properly assess the mechanical properties of fully hydrated SIBS thin films, it is recommended to use a humidity controlled stage compatible with the G200 NanoIndenter from Agilent Technologies, Inc. This stage allows for performing nanoindentation experiments at controlled humidity levels in the range from 5% to 90% relative humidity.

In addition, future studies should also explore the morphology of the SIBS thin films as a function of the thickness of the film, just underneath the surface. These studies could be performed using a grazing incidence small angle X-ray scattering (GISAXS) system and/or via AFM after dry etching the polymer film at different depths.

Finally, to understand the potential application of SIBS thin films into microelectrochemical devices, further adhesion studies should be performed using different metal layers and/or substrates and critical properties such as the selectivity and proton conductivity of the thin films should be characterized.

REFERENCES

- ¹ Daiko, Y.; Katagiri, K.; Matsuda, A. *Chem. Mater.* 2008, 20, 6405-6409.
- ² Anis, A.; Banthia, A.; Bandyopadhyay, S. *J. Power Sources* 2008, 179, 69-80.
- ³ Sekhon, S.; Park, J.; Cho, E., Yoon, Y., Kim Ch., Lee, W. *Macromolecules* 2009, 42, 2054-2062.
- ⁴ Neburchilov, V.; Martin, J.; Wang, H.; Zhang, J. *J. Power Sources* 2007, 169, 221-238.
- ⁵ Kim, T.; Sahimi, M.; Tsotsis, T. *Ind. Eng. Chem. Res.* 2011, 50, 3880-3888.
- ⁶ Majsztrik, P.; Satterfield, M.; Bocarsly, A.; Benziger, J. *J. Membr. Sci.* 2007, 301, 93-106.
- ⁷ Lee, G.; Lee, H.; Kwon, D. *Electrochim. Acta* 2007, 52, 4215-4221.
- ⁸ Kim, S.; Park, M. *Macromolecules* 2010, 43, 8128-8135.
- ⁹ Nakabayashi, K.; Higashihara, T.; Ueda, M. *Macromolecules* 2010, 43, 5756-5761.
- ¹⁰ Yamazaki, K.; Kawakami, H. *Macromolecules* 2010, 43, 7185-7191.
- ¹¹ Elabd, Y.; Hickner, M. *Macromolecules* 2011, 44, 1-11.
- ¹² Lawton, J.; Budil, D. *Macromolecules* 2010, 43, 652-661.
- ¹³ Angelopoulos, M. *IBM J. Res. & Dev.* 2001, 45(1), 57-76.
- ¹⁴ Chu, K.; Shannon, M.; Masela, R. *J. Electrochem. Soc.* 2006, 153(8), A1562-A1567.
- ¹⁵ La O, G.; In, H.; Crumlin, E.; Barbastathis, G.; Horn, Y. *Int. J. Energ. Res.* 2007, 31, 548-575.
- ¹⁶ Napadensky, E. "Investigation of Proton Conductivity of Cation-Exchanged, Sulfonated Poly(*b*-Styrene-*b*-Isobutylene-*b*-Styrene) Membranes", Army Research Laboratory 2009, ARL-TR-4940.
- ¹⁷ Pichonat, T.; Gauthier, B. *Microsyst. Technol.*, 2007, 13, 1671-1678.
- ¹⁸ Shah, K.; Shin, W.; Besser, R. *J. Power Sources* 2003, 123, 172-181.
- ¹⁹ Chen, Z.; Tan, X. *Sens. Actuators A* 2010, 157, 246-257.

-
- ²⁰ Wainrigh, J.; Sanvinell, R.; Liu, C.; Litt, M. *Electrochim. Acta* 2003, 48, 2869-2877.
- ²¹ Van, T.; Nordheden, K.; He, W.; *J. Electrochem. Soc.* 2007, 154(11), A1073-A1076.
- ²² Geng, K.; Yang, F.; Druffel, T.; Grulke, E. *Polymer* 2005, 46, 11768–11772.
- ²³ Pavoov, P.; Bellare, A.; Strom, A.; Yang, D.; Cohen, R. *Macromolecules* 2004, 37, 4865-4871.
- ²⁴ Torres, J.; Stafford, C.; Vogt, B. *ACS Nano* 2009, 3(9), 2677-2685.
- ²⁵ BS EN ISO Standard: 14577-4 (2007) *Metallic Materials. Instrumented indentation test for hardness and materials parameters. Test method for metallic and non-metallic coatings.*
- ²⁶ Shena, L.; Zenga, K.; Wang, Y.; Narayanan, B.; Kumar, R. *Microelectron. Eng.* 2003, 70, 115–124.
- ²⁷ Ma, Z.; Cheng, P.; Zhao, T. *J. Membr. Sci.* 2003, 215, 327-336.
- ²⁸ Volinsky, A. *J. Mater. Res.* 2004, 19 (9), 2650-2657.
- ²⁹ Marques, B.; Wunderle, B.; Johnston, C.; Grant, P. *Acta Mater.* 2013, 61, 2471-2480.
- ³⁰ Hinz, M.; Kleiner, A.; Hild, S.; Marti, O.; D€urig, U.; Gotsmann, B.; Drechsler, U.; Albrecht, T.; Vettiger, P. *Eur. Polym. J.* 2004, 40, 957-964.
- ³¹ Zhao, h.; Li, R. *Composites Part A* 2008, 39, 602-611.
- ³² Wu, Q.; Meng, Y.; Concha, K.; Wang, S.; Li, Y.; M, L.; Fu, S. *Ind. Crop. Prod.* 2013, 48, 28-35.
- ³³ Zheng, X.; Zhou, Y. *Compos. Sci. Technol.* 2005, 65, 1382-1390.
- ³⁴ Wang, H.; Liub, R.; Jianga, W.; Zhua, J.; Fenga, J.; Dinga, g.; Zhaoa, X. *Appl. Surf. Sci.* 2011, 257, 2203-2207.
- ³⁵ Charitidis, C. *Int. Journal of Refractory Metals & Hard Materials* 2010, 28, 51-70.
- ³⁶ Sander, T.; Tremmel, S.; Wartzack, S. *Surf. Coat. Technol.* 2011, 206, (7), 25, 1873-1878.
- ³⁷ Peighambardousta, S.; Rowshanzamira, S.; Amjadia, M. *Int. J. Hydrogen Energy* 2010, 35, 9349-9384.

-
- ³⁸ Costamagna, P.; Srinivasan, S. *J. Power Sources*, 2001, 102, 242-252.
- ³⁹ Smitha, B.; Sridhar, S.; Khan, A. *J. Membr. Sci.* 2005, 259, 10-26.
- ⁴⁰ Viswanathan, B.; Helen, M. *Bulletin of the Catalysis Society of India* 2007, 6, 50-66.
- ⁴¹ Duy, T.; Sawada, S.; Hasegawa, S.; Katsumura, Y.; Maekawa, Y. *J. Membr. Sci.* 2013, 447, 19-25.
- ⁴² Kang, S.; Jung, D.; Shin, J.; Lim, S.; Kim, S.; Shul, Y.; Peck, D. *J. Membr. Sci.* 2013, 447, 36-42.
- ⁴³ Enomoto, K.; Takahashi, S.; Rohani, R.; Maekawa, Y. *J. Membr. Sci.* 2012, 415, 36-41.
- ⁴⁴ Lufrano, F.; Baglio, V.; Staiti, P.; Antonucci, V.; Arico, A. *J. Power Sources* 2013, 243, 519-534.
- ⁴⁵ Zhong, S.; Sun, C.; Luo, Y.; Liu, W.; Dou, S. *J. Power Sources* 2013, 238, 485-491.
- ⁴⁶ Cho, K.; Jung, H.; Sung, S.; Kim, W.; Sung, S.; Park, J.; Choi, J.; Sung, Y. *J. Power Sources* 2006, 159, 524-528.
- ⁴⁷ Park, J.; Kim, J.; Lee, H.; Lee, T.; Joe, Y. *Electrochim. Acta* 2004, 50, 769-775.
- ⁴⁸ Sundmacher, K. *Ind. Eng. Chem. Res.* 2010, 49, 10159-10182.
- ⁴⁹ Barique, M.; Seesukphronrarak, S.; Wu, L.; Ohira, A. *J. Phys. Chem. B*, 2011, 115, 27-33.
- ⁵⁰ Papadimitriou, K.; Geormezi, M.; Neophytides, S.; Kallitsis, J. *J. Membr. Sci.* 2013, 433, 1-9.
- ⁵¹ Tran, T.; Sawada, S.; Hasegawa, S.; Katsumura, Y.; Maekawa, Y. *J. Membr. Sci.* 2013, 447, 19-25.
- ⁵² Bae, B.; Miyatake, K.; Watanabe, M. *Appl. Mater. Interfaces*, 2009, 1(6), 1279-1286
- ⁵³ Avilés, S.; Suleiman, D. *J. Membr. Sci.* 2010, 362, 471-477.
- ⁵⁴ Andzelm, J.; Sloan, J.; Napadensky, E.; Mcknight, S.; Rigby, D. *Mol. Simulat.* 2006, 32 (2), 163-172.
- ⁵⁵ Elabd, Y.; Napadensky, E.; Walker, C.; Winey, K. *Macromolecules*, 2006, 39, 399-407.

-
- ⁵⁶ Crawford, D.; Napadensky, E.; Tan, N.; Reuschle, D.; Mountz, D.; Mauritz, K.; Laverdure, K.; Gido, S.; Liu, W.; Hsiao, B. *Thermochim. Acta* 2001, 367(368), 125-134.
- ⁵⁷ Kamarudin, S.; Achmad, F.; Daud, W. *Int. J. Hydrogen Energy*, 2009, 34, 6902-6916.
- ⁵⁸ http://www1.eere.energy.gov/hydrogenandfuelcells/pdfs/2011_market_report.pdf
- ⁵⁹ Jankowski, A.; Hayes, J.; Graff, R.; Morse, J. *Microfabricated thin film fuel cells for portable power requirements* in: Proceedings of the Spring Meeting of the Materials Research Society, San Francisco, USA, 2002.
- ⁶⁰ Taylor, A.; Lucas, B.; Guo, L.; Thompson, L. *J. Power Sources* 2007, 171, 218-223.
- ⁶¹ Zhang, Y.; Lu, J.; Shimano, S.; Zhou, H.; Maeda, R. *Electrochem. Commun.* 2007, 9, 1365-1368.
- ⁶² Ho, K.; Hung, W. *Sens. Actuators, B* 2001, 79, 11-16.
- ⁶³ Weng, Y.; Hung, K. *Sens. Actuators, B* 2009, 141, 161-167.
- ⁶⁴ Lee, K.; Kim, S.; Ju, B. *World Academy of Science, Engineering and Technology*, 2011, 74, 412-415.
- ⁶⁵ Star, A.; Han, T.; Joshi, V.; Stetter, D. *Electroanal.* 2004, 16, 108-112.
- ⁶⁶ Pantelic, N.; Andria, S.; Heineman, W.; Seliskar, C. *Anal. Chem.* 2009, 81, 6756-6764.
- ⁶⁷ Kokkinos, C.; Economou, A. *Talanta*, 2011, doi:10.1016/j.talanta.2011.01.077.
- ⁶⁸ Lee, Y.; Park, D.; Park, *IEEE Sensors Journal* 2008, 8(11), 1922-1927.
- ⁶⁹ Usman, S.; Willander, M.; Nur, O.; Danielsson, B. *Sens. Actuators, B* 2010, 145, 869-874.
- ⁷⁰ Norouzi P.; Faridbod, F.; Larijani, B.; Reza, M. *Int. J. Electrochem. Sci.* 2010, 5, 1213-1224.
- ⁷¹ Kim, H.; Yoon, S.; Choi, H.; Lyu, Y.; Lee, W. *Bulletin Korean Chemical Society* 2006, 27 (1), 65-70.
- ⁷² Zhou, W.; Li, W. *Nano and Microtechnology: Materials, Processes, Packaging, and Systems, Proceedings of SPIE* 2002, 4936, 154-158.

-
- ⁷³ Weiss, R.; Zhai, X.; Dobrynin, A. *Langmuir* 2008, 24, 5218-5220.
- ⁷⁴ Hill, T.; Carrol, D.; Czerw, R.; Martin, C.; Perahia, D. *J. Polym. Sci., Part B: Polym. Phys.* 2003, 41, 149-158.
- ⁷⁵ Zhou, N.; Chan, C.; Winey, K. *Macromolecules*, 2008, 41, 6134-6140.
- ⁷⁶ Gromadzki, D.; Cernoch, P.; Janata, M.; Kudela, V.; Nallet, F.; Diat, O.; Stepanek, P. *Eur. Polym. J.* 2006, 42, 2486-2496.
- ⁷⁷ Vogt, B.; Soles, C.; Lee, H.; Lin, E.; Wu, W. *Langmuir*, 2004, 20, 1453-1458.
- ⁷⁸ Hill, T.; Jiao, X.; Martin, C.; Perahia, D. *Material Research Society Symposium Proceeding*, 2002, 710, DD13.9.1-DD13.9.6.
- ⁷⁹ Park, M.; Kim, S.; Minor, A.; Hexemer, A.; Balsara, N. *Adv. Mater.*, 2009, 21, 203- 208.
- ⁸⁰ Luo, S.; Craciun, V.; Douglas, E. *Langmuir*, 2005, 21, 2881-2886.
- ⁸¹ Cho, S.; Lee, D. *Sens. Actuators, A* 2011, 165, 316-320.
- ⁸² Pantelic, N, Wansapura, C.; Heineman, W.; Seliskar, C. *J. Phys. Chem.* 2005, 109 (29), 13971-13979.
- ⁸³ Mather, B.; Beyer, F.; Timothy, L. “*Morphological Behavior of Sulfonated Styrene-Ethylene/Propylene-Styrene Triblock Copolymers*” Army Research Laboratoty, 2006, ARL-TR-3727.
- ⁸⁴ Denga, C.; Genga, Y.; Wua, Y.; Wang, Y.; Weia, J. *Microelectron. Eng.* 2013, 103, 7-11.
- ⁸⁵ Nunns, A.; Gwyther, J.; Manners, I. *Polymer* 2013, 54 (4) 1269-1284.
- ⁸⁶ Kravchenko, A.; Shevchenko, A.; Grahn, P.; Ovchinnikov, V.; Kaivol, M. *Thin Solid Films* 2013, 540, 162-167.
- ⁸⁷ Rajarathinam, V.; Allen, S.; Kohl, P. *Microelectron. Eng.* 2012, 93, 19-26.
- ⁸⁸ Puskas, J.; *Macromolecules*, 2002, 183, 191-197.
- ⁸⁹ Ma, Y.; Zhang, Y.; Yu, H.; Zhang, X.; Shu, X.; Tang, B. *Trans. Nonferrous Met. Soc. China* 2013, 23, 2368-2373.

-
- ⁹⁰ Nemecek, J.; Králík, V.; Vondřejc, J. *Computers and Structures* 2013, 128, 136- 145.
- ⁹¹ Hou, L.; Wang, S.; Chen, G.; He, Y.; Xie, Y. *Trans. Nonferrous Met. Soc. China* 2013, 23, 2323-2328.
- ⁹² Chakraborty, H.; Sinha, A.; Mukherjee, N.; Ray, D.; Chattopadhyay, P. *Mater. Lett.* 2013, 93, 137-140.
- ⁹³ Li, X.; Bhushan, B. *Mater. Charact.* 2002, 48, 11-36.
- ⁹⁴ Hay, J. “*Using Instrumented Indentation to Measure the Complex Modulus of Highly Plasticized Polyvinyl Chloride*”, Agilent Technology Application Note, 2010.
- ⁹⁵ Hay, J.; Herbert, E. *Exp. Techniques*, 2010, 2010, 34(3), 86-94.
- ⁹⁶ Marteau, J.; M.Bigerelle, M.; Xia, Y.; Mazeran, P.; Bouvier, S. *Tribol. Int.* 2013, 59, 154-162.
- ⁹⁷ Haungl, B.; Tseng, J.; Wong, M.; Chiu, P.; Kuang, J. *Life Sci. J.* 2013, 10(2), 276-282.
- ⁹⁸ Hay, J.” *Measuring Substrate-Independent Young’s Modulus of Low-k Films by Instrumented Indentation*”, Agilent Technology Application Note, 2010.
- ⁹⁹ Hay, J. “*Measuring Substrate-Independent Young’s Modulus of Hard Overcoats for Magnetic Media*”, Agilent Technology Application Note, 2010.
- ¹⁰⁰ Dupont, S.; Voroshazi, E.; Heremans, P.; Dauskardt, R. *Org. Electron.* 2013, 14, 1262-1270.
- ¹⁰¹ Covarel, G.; Bensaid, B.; Boddaert, X.; Giljean, S.; Benaben, P.; Louis, P. *Surf. Coat. Technol.* 2012, 211, 138-142.
- ¹⁰² Koski, K.; Hölsä, J.; Ernoulth, J.; Rouzaud, A. *Surf. Coat. Technol.* 1996, 80 (1-2), 195-199.
- ¹⁰³ Harish, C.; Barshilia, H.; Ananth, A.; Khan, J.; Srinivas, G. *Vacuum* 2012, 86 (8), 1165-1173.
- ¹⁰⁴ Wenxia Zhaoa, W.; Wang, Z. *Int. J. Adhes. Adhes.* 2013, 41, 50-56.
- ¹⁰⁵ Ammar, M.; Legeay, G.; Bulou, A.; Bardeau, J. *Surf. Coat. Technol.* 2009, 203, 2202-2206.
- ¹⁰⁶ Pantoja, M.; Encinas, N.; Abenojar, J.; Martínez, M. *Appl. Surf. Sci.* 2013, 280, 850-857.

-
- ¹⁰⁷ Boddaert, X.; Covarel, G.; Bensaid, B.; Mattei, M.; Benaben, P.; Bois, J. *Thin Solid Films* 2013, 528 194-198.
- ¹⁰⁸ Junga, C.; Choa, H.; Hwanga, I.; Choia, J.; Nhoa, Y.; Shinb, J.; Chang, K. *Radiat. Phys. and Chem.* 2012, 81(8), 919-922.
- ¹⁰⁹ Suna, J.; Qiana, S.; Lia, Y.; Hea, X.; Zhenga, Z. *Measurement*, 2013, 46(8), 2278-2287.
- ¹¹⁰ <http://oxforddictionaries.com/definition/english/adhesion>
- ¹¹¹ Mittal, K.; *Electrocomponents Science and Technology* 1976, 3, 21-42.
- ¹¹² Fraunhofer, J. *Int. J. Dentistry* 2012, doi:10.1155/2012/951324.
- ¹¹³ ASTM Standard: C1624-05 (2010) *Standard test method for adhesion strength and mechanical failure modes of adhesion ceramic coating by quantitative single point scratch testing.*
- ¹¹⁴ Rimai, D.; DeMejo, L.; Mittal, K.; *Fundamental of adhesion and interfaces*, Utrecht-The Netherlands, Tokyo, 1995, p 206.
- ¹¹⁵ Mittal, K. *Adhesion measurement of films and coating*, Utrecht-The Netherlands, Tokyo, 1995, p 2.
- ¹¹⁶ Farokhzadeh, K.; Edrisy, A.; Pigott, G.; Lidster, P. *Wear* 2013, 302, 845-853.
- ¹¹⁷ Barletta, M.; Tagliaferri, V.; Gisario, A.; Venettacci, S. *Tribol. Int.* 2013, 64, 39-52.
- ¹¹⁸ Barlettaa, M.; Pezzolaa, S.; Trovaluscib, F.; Vescoa, S. *Prog. Org. Coat.* 2013, 76, 1494-1504.
- ¹¹⁹ Beake, B.; Davies, M.; Liskiewicz, T.; Vishnyakov, V.; Goodes, S. *Wear* 2013, 301, 575-582.
- ¹²⁰ Liu, Z.; Pan, C.; Chen, Y.; Liang, P. *Thin Solid Films* 2013, 531, 284-293.
- ¹²¹ ASTM Standard: D7187-10 (200*) *Standard test method for measuring mechanistic aspect of scratch/mar behavior of paint coating by nanoscratching.*
- ¹²² Miksovsky, J.; Kutilek, P.; Lukes, J.; Tolde, Z.; Remsa, J.; Kocourek, T.; Uherek, F.; Jelinek, M. *Chem. Listy* 2011, 105, S692-S695.
- ¹²³ Xia, H.; Jun, H.; Honglai, L.; Ying, H. *Langmuir*, 2006, 22, 3428-3433.

-
- ¹²⁴ Vaughan, C. *J. Soc. Cosmet. Chem.*, 1985, 36, 319-333.
- ¹²⁵ Drobry, J. *Handbook of Thermoplastic Elastomers*; William Andrew Publishing, New York, 2007; Vol. 2, p 142.
- ¹²⁶ Saito, T.; Moore, H.; Hickner, M. *Macromolecules*, 2010, 43, 599-601.
- ¹²⁷ Rikukawa, M.; Sanui, K. *Prog. Polym. Sci.* 2000, 25, 1463-1502.
- ¹²⁸ http://www.paper.edu.cn/en_releasepaper/content/4425372
- ¹²⁹ Xu, S.; Li, M.; Mitov, Z.; Kumacheva, E. *Prog. Org. Coat.* 2003, 48, 227-235.
- ¹³⁰ Salvador, M.; Bianchi, A.; Pereira, M.; Carvalho, A. *Polymer* 2010, 51, 4145-4151.
- ¹³¹ Luo, S.; Craciun, V.; Douglas, E. *Langmuir* 2005, 21, 2881-2886.
- ¹³² Kaniappan, K.; Latha, S. *Int. J. Chem. Tech. Res.* 2011, 3 (2), 708-717.
- ¹³³ Walch, E.; Gaymans, R.; *Polymer* 1994, 35 (8), 1774-1778.
- ¹³⁴ Aviles-Barreto, S.; Suleiman, D. *J. Appl. Polym. Sci.* 2013, 129 (4), 2294-2304.
- ¹³⁵ Elabd, J.; Napadensky, E. *Polymer* 2004, 45, 3037-3043.
- ¹³⁶ Crawford, D.; Napadensky, E.; Beck, N.; Reuschle, D.; Mountz, D.; Mauritz, K.; Laverdure, K.; Gido, S.; Liu, W.; Hsiao, B. *Thermochim. Acta* 2001, 367-368, 125-134.
- ¹³⁷ Storey, R.; Baugh, D. *Polymer* 2000, 41, 3205-3211.
- ¹³⁸ Elabd, Y.; Beyer, F.; Walker, C. *J. Membr. Sci.* 2004, 231, 181-188.
- ¹³⁹ Fang, L.; Wei, M.; Barry, C.; Mead, J. *Macromolecules* 2010, 43, 9747-9753.
- ¹⁴⁰ Fang, L.; Wei, M.; Shang, Y.; Jimenez, L.; Kazmer, D.; Barry, C.; Mead, J. *Polymer* 2009, 50, 5837-5845.
- ¹⁴¹ Niu, S.; Saraf, R. *Macromolecules* 2003, 36, 2428-2440.
- ¹⁴² Kim, B.; Lee, H.; Lee, J.; Son, S.; Jeong, S.; Lee, S.; Lee, D.; Kwak, S.; Jeong, H.; Shin, H.; Yoon, J.; Lavrentovich, O.; Kim, S. *J. Adv. Funct. Mater.* 2009, 19, 2584-2591.

-
- ¹⁴³ Torrisi, V.; Ruffino, F.; Licciardello, A.; Grimaldi, M.; Marletta, G. *Nanoscale Res. Lett.* 2011, 6:167.
- ¹⁴⁴ Wang, Y.; Hong, X.; Liu, B.; Ma, C.; Zhang, C. *Macromolecules* 2008, 41, 5799-5808.
- ¹⁴⁵ Zhang, X., Liu, S., Yin, J. *J. Membr. Sci.* 2005, 258, 78-84.
- ¹⁴⁶ Xia, H.; Honglai, L.; Yarning, D.; Yiang, H. *Chin. J. Chem. Eng.* 2005, 13 (4), 498-503.
- ¹⁴⁷ Park, M.; Balsara, N. *Macromolecules*, 2008, 41, 3678-3687.
- ¹⁴⁸ <http://www-bsac.eecs.berkeley.edu/~mccoy/files/091018-material-properties-efunda-v02.pdf>.
- ¹⁴⁹ Wang, D.; Fujinami, S.; Liu, H.; Nakajima, K.; Nishi, T. *Macromolecules* 2010, 43, 9049-9055.
- ¹⁵⁰ Guan, R.; Dai, H.; Li, C.; Liu, J.; Xu, J. *J. Membr. Sci.* 2006, 277, 148-156.
- ¹⁵¹ Gilles P. Robertson, G.; Mikhailenko, S.; Wang, K.; Xing, P.; Guiver, M.; Kaliaguine S. *J. Membr. Sci.* 2003, 219 (1-2), 113-121.
- ¹⁵² Fu, Y.; Hu, C.; Qui, H.; Lee, K.; Lai, J. *Sep. Purif. Technol* 2008, 62, 175-182.
- ¹⁵³ Mali, S.; Sakanaka, I.; Yamashita, F.; Grossmann, M. *Carbohydr. Polym.* 2005, 60 (3), 283-289.
- ¹⁵⁴ Bourtoom, T.; Songklanakarin *J. Sci. Technol.* 2008, 30 (1), 149-165.
- ¹⁵⁵ Zhou, J.; Komvopoulos, K. *J. Appl. Phys.* 2006, 100 (11), 114329-14329.
- ¹⁵⁶ Sethuraman, V.; Weidner, J.; Haug, A.; Protsailo, L. *J. Electrochem. Soc.*, 2008, 155 (2), B119-B124.
- ¹⁵⁷ Jung, H.; Kim, J. *Int. J. Hydrogen Energy* 2012, 37, 12580-12585.
- ¹⁵⁸ Martinez, A.; Imrie, C.; Ribes, A. *J. Appl. Polym. Sci.* 2013, DOI 10.1002/APP.37881
- ¹⁵⁹ Albers, D.; Galgoci, M.; King, D.; Miller, D.; Newman, R.; Peerey, L.; Tai, E.; Wolf, R. *Org. Process Res. Dev.* 2007, 11, 846-860.
- ¹⁶⁰ Critter, S.; Airoidi, C. *J. Braz. Chem. Soc.* 2006, 17 (7), 1250-1258.

-
- ¹⁶¹ Pansu, M.; Gautheyron, J. *Handbook of Soil Analysis, Mineral, Organic and Inorganic Methods*, Springer, 2006, p 1.
- ¹⁶² Naim, R.; Ismail, A.; Saidi, H. *Effects of sulfonation process on thermal behavior and microstructure of sulfonated polysulfone membranes as a material for Proton Exchange Membrane (PEM)*, Proceedings of Regional Symposium on Membrane Science and Technology, Johor Bharu, Malaysia, April 21, 2004.
- ¹⁶³ Unveren, E.; Erdogan, T.; Celebi, S.; Inan, T. *Int. J. Hydrogen Energy* 2010, 35, 3736 - 3744.
- ¹⁶⁴ Pavoov, P.; Bellare, A.; Strom, A.; Yang, D.; Cohen, R. *Macromolecules* 2004, 37, 4865-4871.
- ¹⁶⁵ “*Nanoindentation, Scratch, and Elevated Temperature Testing of Cellulose and PMMA Films*” Agilent Application Note, 2010.
- ¹⁶⁶ “*Scratch Testing of Low-k Dielectric Films and a Correlation Study of the Results*” Agilent Application Note, 2010.
- ¹⁶⁷ ASTM standard: D 7027-05 (2009) *Standard Test Method for Evaluation of Scratch Resistance of Polymeric Coatings and Plastics Using an Instrumented Scratch Machine*.
- ¹⁶⁸ Wong, M.; Moyse, A.; Lee, F.; Sue, H. *J. Mater. Sci.* 2004, 39, 3293-3308.
- ¹⁶⁹ Jiang, H.; Browning, R.; Sue, H. *Polymer* 2009, 50, 4056-4065.
- ¹⁷⁰ Xiang, C.; Sue, H.; Chu, J.; Coleman, B. *J. Polym. Sci. Pol. Phys.* 2001, 39, 47-59.